



THE  
2  
2007

This is to certify that the  
dissertation entitled

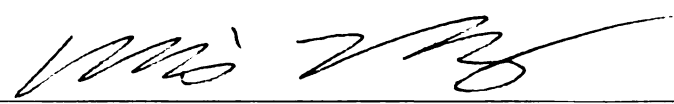
COMPUTATIONAL AEROACOUSTICS:  
ITS METHODS AND APPLICATIONS

presented by

Shi Zheng

has been accepted towards fulfillment  
of the requirements for the

Ph.D. degree in Mechanical Engineering



Major Professor's Signature

8/18/2006

Date

*MSU is an Affirmative Action/Equal Opportunity Institution*

**LIBRARY**  
**Michigan State**  
**University**



**COMPUTATIONAL AEROACOUSTICS:  
ITS METHODS AND APPLICATIONS**

By

Shi Zheng

**A DISSERTATION**

**Submitted to  
Michigan State University  
in partial fulfillment of the requirements  
for the degree of**

**DOCTOR OF PHILOSOPHY**

**Department of Mechanical Engineering**

**2006**

# **ABSTRACT**

## **COMPUTATIONAL AEROACOUSTICS: ITS METHODS AND APPLICATIONS**

By

Shi Zheng

The first part of this thesis deals with the methodology of computational aeroacoustics (CAA). The effects of parameters used in constructing a broadband optimized upwind scheme are systematically studied. It is shown that there are optimum values for these parameters for a given range of wavenumber, at which the overall accuracy of the scheme improves. However a scheme that is accurate everywhere in a wide range is virtually not possible because increasing the accuracy for large wavenumbers is always at the expense of decreasing the accuracy for smaller wavenumbers. Partially for avoiding such a dilemma, optimized multi-component schemes are proposed. When calculating a sound field with dominant wavenumbers, such a scheme is superior to an optimized broadband scheme. The Fourier analysis shows that even for broadband waves an optimized central multi-component scheme is at least comparable to if not better than an optimized central broadband scheme.

Numerical implementation of the impedance boundary condition in the time domain is a unique and challenging topic in CAA. A problem is proposed and its analytical solution is derived and evaluated to benchmark such boundary conditions. A CAA code using Tam and Auriault's formulation of broadband time-domain impedance boundary condition very accurately reproduces the analytical solution. The CAA code is also tested against the analytical solution of a semi-infinite impedance duct problem and

the experimental data from the NASA Langley flow impedance tube facility in the presence of a sheared or zero mean flow. The CAA code accurately predicts the duct acoustics in terms of both amplitude and phase.

In the second part of the thesis are applications of the developed CAA codes. A time-domain method is formulated to separate the instability waves from the acoustic waves of the linearized Euler equations in a critical sheared mean flow. The effectiveness of the method is demonstrated by a test problem solved with the CAA code.

Several other applications are concerned with coupling an optimizer with the CAA code. A noise prediction and optimization system for turbofan engine inlet duct designs is developed. The noise prediction system is verified with several test problems, each emphasized on testing a specific aspect of the system. The noise prediction and optimization system is applied in three scenarios: liner impedance optimization, duct geometry optimization and liner layout optimization. The results show that the system is effective in finding values for the design variables in favor of a given objective function.

With the same idea of coupling an optimizer with the CAA code but in a different context, a conceptual design for adaptive noise control is developed. It consists of a liner with controllable impedance and an expert subsystem which is realized with an optimizer coupled with the CAA code. It is shown that the expert system is able to find the impedance properties that minimize the difference between the current and the desired acoustic fields.

## ACKNOWLEDGEMENTS

I am most grateful to my advisor Professor Mei Zhuang, for her intellectual and financial support throughout my studies at Michigan State. She has always been a source of inspiration and brought out the best in me. Without her constant encouragement and guidance, I could not have finished this thesis. I could not have wished for a better friend and mentor.

I would also like to thank Professor Ahmed Naguib, Professor Tom I-P. Shih, Professor Z.J. Wang and Professor Zhengfang Zhou for being kind enough to serve as members of my guidance committee. Special thanks go to Professor Tom I-P. Shih, Professor Z.J. Wang, who came to my oral defense from Iowa in spite of their busy schedules.

I wish to express my gratitude to other people who contributed to this thesis one way or another. Among them are Professor F. Q. Hu from Old Dominion University for his helpful discussion, Dr. Rangfu Chen (former PhD student of Professor Zhuang), whose computer program was a starting point for the code developed in my research, Dr. W. R. Watson at NASA Langley Research Center, who provided experimental data and very helpful suggestions and comments, and Steve Miller (former intern working with Professor Zhuang), whose active involvement added values to the method of separating instability waves from acoustic waves.

I would like to acknowledge the National Science Foundation. Part of the work in this thesis was supported by the grant NSF-MRSEC DMR09809688.

I owe deepest thanks to my parents who have been supporting me since I was born. Their encouragement for my education has never ceased because I came to this other side of the globe. I am indebted to my wife Jenny for giving up her career selflessly and taking care of all the household chores while I was on my thesis journey. This thesis would not have been accomplished without her. I dedicate this thesis to my family.

# TABLE OF CONTENTS

LIST OF TABLES .....	ix
LIST OF FIGURES .....	x
1 INTRODUCTION.....	1
1.1 CAA Numerical Schemes and Boundary Conditions .....	1
1.2 CAA Applications .....	3
1.3 Thesis Outline.....	7
2 HIGH-ORDER OPTIMIZED NUMERICAL SCHEMES FOR COMPUTATIONAL AEROACOUSTICS.....	10
2.1 High-Order Optimized Upwind Broadband Schemes .....	10
2.2 High-Order Optimized Multi-Component Schemes .....	17
3 A THREE-DIMENSIONAL BENCHMARK PROBLEM FOR BROADBAND TIME DOMAIN IMPEDANCE BOUNDARY CONDITIONS .....	31
3.1 Formulation of the Test Problem.....	31
3.2 The Analytical Solution.....	31
3.3 Numerical Implementation.....	36
3.3.1 Broadband Dispersion-Relation-Preserving (DRP) Upwind Scheme ..	36
3.3.2 Broadband Time Domain Impedance Boundary Condition .....	36
3.3.3 Nonreflecting Radiation Boundary Condition .....	37
3.4 Comparison of the Results.....	38
4 VERIFICATION AND VALIDATION OF A TIME-DOMAIN IMPEDANCE BOUNDARY CONDITION IN LINED DUCTS.....	40
4.1 Verification with Analytical Solution .....	41
4.1.1 Verification Problem and its Analytical Solution.....	41
4.1.2 Methodology of the Numerical Implementation.....	45

4.1.3	Comparison with the Analytical Solution.....	47
4.2	Validation with Experimental Data.....	51
4.2.1	Experimental Setup.....	51
4.2.2	Numerical Results and Comparison with the Experimental Data.....	51
5	<b>A TIME-DOMAIN METHOD FOR ACOUSTIC WAVE SOLUTIONS OF MULTI-FREQUENCY SOUND SOURCES IN SHEARED MEAN FLOWS .....</b>	<b>57</b>
5.1	Problem Formulation.....	57
5.2	Instability Wave and Analytical Solution.....	60
5.2.1	Instability Wave .....	60
5.2.2	Analytical Solution to the Acoustic Wave.....	61
5.3	Numerical Solution.....	62
5.3.1	Numerical solutions of the Total Solution and the Pure Instability Wave Solution.....	63
5.3.2	Constructing the Contained Instability Wave .....	66
5.3.3	Acoustic Wave Solution in Comparison with the Analytical Solution.	70
6	<b>COMPUTATIONAL AEROACOUSTICS TIME-DOMAIN METHOD COUPLED WITH ADAPTIVE NOISE CONTROL OPTIMIZER .....</b>	<b>73</b>
6.1	Adaptive Noise Control System .....	74
6.1.1	The Expert System.....	74
6.1.2	Liners with Controllable Impedance.....	76
6.2	Numerical Implementation and Results .....	77
7	<b>NOISE PREDICTION AND OPTIMIZATION SYSTEM FOR TURBOFAN ENGINE INLET DUCT DESIGN.....</b>	<b>88</b>
7.1	Noise Prediction System.....	88
7.1.1	Governing Equations.....	89
7.1.2	Boundary Conditions .....	90

7.1.3	Grid Generation and Transformation of the Governing Equations and Boundary Conditions .....	94
7.1.4	Numerical Schemes.....	95
7.1.5	Kirchhoff Integral .....	95
7.2	Verification of Noise Prediction System.....	96
7.2.1	Semi-Infinite Hard-Wall Annular Duct .....	96
7.2.2	Semi-Infinite Hard-Wall Circular Duct .....	97
7.2.3	Semi-Infinite Lined-Wall Circular Duct .....	98
7.2.4	Test Problem for the Kirchhoff Code .....	99
7.3	Liner Impedance Optimization.....	100
7.3.1	Problem Definition.....	100
7.3.2	Optimization Result .....	101
7.4	Geometry Optimization.....	102
7.4.1	Problem Definition.....	102
7.4.2	Optimization Result .....	103
7.5	Liner Layout Optimization.....	104
7.5.1	Problem Definition.....	105
7.5.2	Optimization Result .....	107
8	CONCLUSIONS.....	110
	BIBLIOGRAPHY.....	115

## LIST OF TABLES

<b>Table 2.1</b> The coefficients of three schemes using the same stencil.....	19
<b>Table 4.2</b> Impedance on the wall and at the exit.....	51
<b>Table 5.1</b> The mean flow parameters .....	58
<b>Table 5.2</b> The sound source parameters for the three-frequency-component sound source .....	59
<b>Table 6.1</b> Values for the impedance parameters .....	87

## LIST OF FIGURES

**Figure 2.1** Comparisons of the optimized upwind broadband schemes ( $\lambda = 0.9661$  and  $\sigma = 0.2795\pi$ ) with the standard Taylor scheme. (a)  $\bar{\alpha}_r / \alpha - 1$  versus  $\alpha\Delta x$ ; (b)  $\bar{\alpha}_i / \alpha$  versus  $\alpha\Delta x$  ..... 14

**Figure 2.2** The effect of the parameter  $\sigma$  on an optimized upwind broadband scheme with  $\beta_0 = \pi/2$  and  $\lambda = 0.9661$ . (a)  $\bar{\alpha}_r / \alpha - 1$  versus  $\alpha\Delta x$ ; (b)  $\bar{\alpha}_i / \alpha$  versus  $\alpha\Delta x$  ..... 15

**Figure 2.3** The effect of the parameter  $\lambda$  on an optimized upwind broadband scheme with  $\beta_0 = \pi/2$  and  $\sigma = 0.2795\pi$ .  $\bar{\alpha}_r / \alpha - 1$  versus  $\alpha\Delta x$ ; (b)  $\bar{\alpha}_i / \alpha$  versus  $\alpha\Delta x$  ..... 16

**Figure 2.4** Comparisons of the optimized upwind 3-component scheme ( $\alpha = 11\pi/60$ ,  $7\pi/30$  and  $\pi/3$ ,  $\varepsilon = 10^{-5}$ ), the optimized upwind broadband scheme ( $\beta_0 = \pi/2$ ,  $\lambda = 0.9962$ ,  $\sigma = 0.2795\pi$ ) and the standard Taylor scheme (a)  $\bar{\alpha}_r / \alpha - 1$  versus  $\alpha\Delta x$ ; (b)  $\bar{\alpha}_i / \alpha$  versus  $\alpha\Delta x$  ..... 23

**Figure 2.5** Enlarged plots of the areas bounded with dashed lines in Figure 2.4. (a)  $\bar{\alpha}_r / \alpha - 1$  versus  $\alpha\Delta x$ ; (b)  $\bar{\alpha}_i / \alpha$  versus  $\alpha\Delta x$  ..... 24

**Figure 2.6** The results of the acoustic wave propagation with the three dominant wavenumbers, predicted by different numerical schemes. (a) velocity or pressure perturbation after  $120000\Delta x$  (1000 fundamental wavelengths) propagation; (b) local corresponding errors. .... 25

**Figure 2.7** The wavenumber spectrum of the broadband wave. .... 26

**Figure 2.8** The results of the broadband acoustic wave after traveling a distance of  $12000\Delta x$  predicted by different schemes. (a) wave shapes as compared to the exact solution, (b) local corresponding errors. .... 29

**Figure 2.9** Comparisons of the central multi-component schemes with Tam's central schemes and the standard Taylor scheme. The dots on the horizontal axis indicate the values of  $\alpha\Delta x$  for which the 1- or 2-component schemes are optimized. .... 30

**Figure 3.1** Schematic of the test problem ..... 32

**Figure 3.2** Comparison of the acoustic pressure along the  $x$ -axis at (a)  $t = 20$  and (b)  $t = 30$  ..... 38

<b>Figure 3.3</b> Comparison of the acoustic pressure along the $z$ -axis at $t = 30$ .....	39
<b>Figure 4.1</b> The semi-infinite impedance duct .....	41
<b>Figure 4.2</b> Comparison of the numerical solution with the analytical solution for the least attenuated mode of the semi-infinite duct problem with a zero mean flow. (a) Sound pressure level along the hard wall; (b) Phase along the hard wall. ....	49
<b>Figure 4.3</b> Comparison of the numerical solution with the analytical solution for the least attenuated mode of the semi-infinite duct problem with a sheared mean flow $M(y) = 1.2(y/h)(1 - y/h)$ . (a) Sound pressure level along the hard wall; (b) Phase along the hard wall.....	50
<b>Figure 4.4</b> Configuration of the NASA Langley flow-impedance tube.....	50
<b>Figure 4.5</b> Comparison of the numerical solution with the experimental result at test frequencies with a zero mean flow. (a) SPL along the upper (hard) wall; (b) Phase along the upper (hard) wall.....	54
<b>Figure 4.6</b> Comparison of the numerical solution with the experimental result at test frequencies with a mean flow profile assumed as $M(y) = 1.2(y/h)(1 - y/h)$ . (a) SPL along the upper (hard) wall; (b) Phase along the upper (hard) wall.....	56
<b>Figure 5.1</b> The domain of interest with a sound source and a sheared mean flow .....	57
<b>Figure 5.2</b> The computational domain with the grid distribution. The unshaded area is the PML regions. ....	64
<b>Figure 5.3</b> The sound pressure $t = 224T_1$ in the entire computational domain of $-250\text{m} \leq x \leq 350\text{m}$ and $0\text{m} \leq y \leq 100\text{m}$ . Outside the region confined by the long-dashed line is the PML region; the region confined by the short-dashed line is the domain of interest. (a) the total solution; (b) the pure instability wave solution. Note that the contours in the two plots are not on the same scale. ....	66
<b>Figure 5.4</b> The sound pressure $t = 224T_1$ in the domain of interest for the three-frequency component sound source. (a) the total solution; (b) the contained instability wave solution; (c) the acoustic wave solution. ....	71
<b>Figure 5.5</b> The sound pressure for the three-frequency component sound source at $t = 224T_1$ as compared with the analytical solution along the lines of (a) $-50 \text{ m} \leq x \leq 150 \text{ m}$ at $y = 15 \text{ m}$ , (b) $-50 \text{ m} \leq x \leq 150 \text{ m}$ at $y = 50 \text{ m}$ and (c) $5 \text{ m} \leq y \leq 50 \text{ m}$ at $x = 100 \text{ m}$ .....	72
<b>Figure 6.1</b> Schematic of the adaptive noise control system.....	73

<b>Figure 6.2</b> Test problem schematic.....	77
<b>Figure 6.3</b> Optimization process .....	79
<b>Figure 6.4</b> Acoustic pressure fields at $t = 25$ without mean flow. (a) the unperturbed desired; (b) the perturbed desired; (c) the optimized (resultant) for the perturbed desired. ....	83
<b>Figure 6.5</b> Acoustic pressure fields at $t = 25$ with a uniform mean flow of $M_x = 0.8$ and $M_y = 0$ . (a) the unperturbed desired; (b) the perturbed desired; (c) the optimized (resultant) for the perturbed desired. ....	84
<b>Figure 6.6</b> Acoustic pressure fields at $t = 25$ with a sheared mean flow of $M_x(y) = 0.8 \sin[(\pi/2)(y/40)]$ and $M_y = 0$ . (a) the unperturbed desired; (b) the perturbed desired; (c) the optimized (resultant) for the perturbed desired.....	85
<b>Figure 6.7</b> Acoustic pressure fields at $t = 25$ with a sheared mean flow of $M_x(y) = 0.8 \sin[(\pi/2)(y/40)]$ and $M_y = 0$ . (a) the modified desired; (b) the optimized (resultant) for the modified desired. ....	86
<b>Figure 7.1</b> The whole computational domain .....	89
<b>Figure 7.2</b> Types of boundary conditions .....	90
<b>Figure 7.3</b> Results of the hard-wall annular duct problem. The exact and the numerical solutions are above and below the axis, respectively. (a) mode (6,1); (b) mode (6,2).....	97
<b>Figure 7.4</b> Results of the hard-wall circular duct problem. The exact and the numerical solutions are above and below the axis, respectively. (a) mode (6,1); (b) mode (6,2).....	98
<b>Figure 7.5</b> Results of the lined-wall circular duct problem. The exact and the numerical solutions are above and below the axis, respectively. (a) $\omega = 12$ , $Z = 0.2 - i$ , mode (6,1); (b) $\omega = 10$ , $Z = 0.2 + i$ , mode (6,1). ....	98
<b>Figure 7.6</b> Schematic of the test problem for the Kirchhoff method .....	99
<b>Figure 7.7</b> Results of the test problem for the Kirchhoff method .....	100
<b>Figure 7.8</b> The history of the objective function during the liner impedance optimization .....	101
<b>Figure 7.9</b> The history of the design variables $R$ and $X$ during the liner impedance optimization. ....	101

<b>Figure 7.10</b> The sound field calculated with the optimized liner impedance. ....	102
<b>Figure 7.11</b> The sound field calculated with the original geometry and without liners applied.....	102
<b>Figure 7.12</b> The history of the objective function during the geometry optimization...	103
<b>Figure 7.13</b> The history of the design variables $a$ and $b$ during the geometry optimization. ....	103
<b>Figure 7.14</b> The sound field calculated with the optimized geometry.....	104
<b>Figure 7.15</b> The sound fields with different layouts of liner patches. The bold lines indicate the liner patches. Equal amounts of liner are applied for the two cases. ....	105
<b>Figure 7.16</b> Patches of liner on the duct wall.....	107
<b>Figure 7.17</b> Affected region and airplane path .....	107
<b>Figure 7.18</b> The history of the objective function during the geometry optimization... ..	108
<b>Figure 7.19</b> The history of the design variables $x_1$ and $x_2$ during the geometry optimization. ....	108
<b>Figure 7.20</b> The sound field before (a) and after (b) optimization. ....	109

# 1 INTRODUCTION

## 1.1 CAA Numerical Schemes and Boundary Conditions

Computational aeroacoustics (CAA) deals with the problems of sound generation and propagation in the presence of a mean flow. Acoustic fluctuations are many orders of magnitude smaller than the mean flow variables. Therefore, the numerical schemes for CAA are required to be much more accurate than those for traditional computational fluid dynamics (CFD). The dispersion and the dissipation errors of the numerical schemes have to be minimized to ensure that waves travel with an accurate speed, phase and amplitude. In the past ten years or so, many numerical schemes with high accuracy have been developed for applications in CAA. One approach for designing these schemes is to lower the otherwise possible maximum order of accuracy for a given stencil width such that the additional degrees of freedom can be used to minimize the integrated error over a range of wavenumber. It is noted from Zhuang and Chen's work [67] that for optimized upwind schemes the range of wavenumber is not the only parameter involved in the optimization process. Other parameters also play an important role in the optimization. A systematic study of the effects of parameters involved in the optimization, on the characteristics of the dispersion and the dissipation errors is critical to better understanding and improving the optimized schemes. For example, previous works [21, 22, 45] show that if a relatively large range of wavenumber is chosen for the optimization, the deviations from the exact solutions for small wavenumbers will be excessive, although the scheme can give accurate solutions at relatively large wavenumbers. Therefore, further improvement of the optimized schemes over a range of wavenumber is limited due to the fact that increasing the accuracy for relatively large values of

wavenumbers is at the expense of decreasing the accuracy for smaller values of wavenumbers. Since some acoustic waves travel with dominant wavenumbers in a range of spectrum, one possible way to design a better scheme for this class of acoustic wave propagation problems is to optimize the scheme for these dominant wavenumbers. The scheme would be superior to those optimized for a range of spectrum (optimized broadband schemes). In addition, the scheme optimized for the selected wavenumbers may give reasonably accurate results even for broadband waves if the deviations from the exact solutions are also relatively small at non-selected wavenumbers. The effects of parameters on optimized upwind schemes will be investigated and schemes optimized for multiple components will also be designed in this thesis.

As important to accurate CAA predictions as a numerical scheme are numerical boundary conditions for CAA. One of them is impedance boundary condition. Since impedance is conventionally defined in the frequency domain, such information must be properly converted into the time domain to serve as a well-posed boundary condition for the governing equations. Tam and Auriault developed their time-domain single-frequency and broadband impedance boundary conditions for the three-parameter impedance model of the Helmholtz resonator type, by implicitly using the derivative properties of the Fourier transform.[49] Özyörük and Long borrowed the idea from the computational electromagnetics community and proposed their time-domain surface acoustic impedance condition based on the z-transform.[33] Fung and Ju applied the inverse Fourier transform to the reflection coefficient instead of the corresponding impedance, resulting in a stable time-domain impedance boundary condition. [13, 14]

Özyörük and Long [33, 34] and Ju and Fung [17] have applied their own time-domain impedance boundary conditions to the NASA Langley flow impedance tube, for which experimental data are available. Favorable predictions of the sound pressure level (SPL) were reported for the both groups, but predictions of the phase information have not seen published. Tam and Auriault have tested their time-domain impedance boundary condition for a one-dimensional problem. [49] In this thesis the same formulation will be verified with a problem in three dimensional semi-open space bounded by an impedance wall. Because of the difference in geometry between a duct and an open space, which results in the concept of modes for a duct configuration, Tam and Auriault' formulation will be further verified and validated in a duct configuration. This is one of the topics of this thesis.

## **1.2 CAA Applications**

Since the perturbations of a sound source are so small compared to the mean flow, the effect of its propagation on the mean flow is in general negligible. It is therefore a common practice to study the convection and refraction effects of a sheared mean flow on acoustic wave propagation by solving the linearized Euler equations (LEE) based on such a mean flow. Unfortunately, the instability wave is intrinsic to the solution of the homogenous LEE (for a shear flow, these instability waves are well known Kelvin-Helmholz instabilities). The solution of the LEE includes both the instability wave solution and the acoustic wave solution. Because the instability waves grow exponentially as they are convected to the downstream, they can overwhelm the acoustic wave solution downstream of the sound source. In order to develop a numerical solver to study the effects of a mean flow on acoustic wave propagation, it is critical to establish a

method that can either suppress the instability waves or isolate the instability waves from the total solution so that the acoustic wave solution can be obtained by subtracting the instability wave solution from the total solution.

In the past, many techniques have been developed for this purpose. Agarwal et al. [15, 08, 24, 53] developed a general technique in the frequency domain to filter out the instability waves. The method is simple and effective than the previous studies [15, 08, 24, 53]. However, the disadvantages of the technique are that it requires a large amount of memory due to direct matrix solvers and it can only handle single frequency sound sources due to the nature of frequency-domain approaches. Ewert and Schröder [12] presented a time-domain approach by formulating acoustic perturbation equations driven by sources determined from a compressible flow simulation. They demonstrated that the systems of acoustic equations are free of instability waves for critical mean flows. Recently Zheng et al. [59] developed a time-domain method to separate the instability waves from the acoustic waves without any modifications of the governing equations. For a single frequency noise source, they have shown that by placing a sound source with the same excitation frequency upstream of the domain of interest, where the acoustic wave solution is desired, the instability wave solution alone can be approximated in the region of interest. The acoustic wave solution is then successfully achieved by subtracting the instability wave solution from the total solution of the LEE. Since one of the main advantages of the time-domain technique is that it can handle multi-frequency or broadband noise sources, one objective of this thesis is to extend the above global time-domain technique to multi-frequency or broadband noise sources so that the

separation of the acoustic wave solution from the instability wave solution can be performed effectively for any noise sources in critical mean flows.

Noise, as an environmental issue, has a major impact on both the conceptual and detailed design of modern aircraft engines. Because of the large bypass ratios in modern aircraft engines, fan noise is becoming an increasingly important noise source during the critical take-off and landing phases. Reducing acoustic noise emission of jet engines is of great interest in civil applications. This is where CAA is of great importance. Novel acoustic treatments and scarfed inlets of turbofan engine inlet ducts designed to attenuate such noise are therefore vital for the noise reduction of modern aircraft engines. These designs usually rely upon extensive experimental tests, which are very expensive and time consuming. Novel acoustic liners designed to attenuate such noise are therefore vital for the noise reduction of modern aircraft turbofan engines. These designs usually rely upon extensive experimental tests, which are very expensive and time consuming. In order to achieve optimal acoustic liner designs, it is necessary to have accurate impedance models and aeroacoustic prediction tools so that acoustic fields inside and radiated from both inlet and exhaust of turbofan engines can be predicted accurately and efficiently. For this reason, there have been ongoing research activities for the development of numerical noise prediction systems,[ 3, 9, 11, 19, 20, 28, 30, 39, 41, 42, 43, 44, 58, 65] and impedance boundary conditions. [13, 14, 17, 26, 27, 32, 33, 35, 49, 64] In the past, there have been ongoing research activities for the development of numerical noise prediction systems.[3, 9, 30, 36, 41, 43, 44] It has been shown that these numerical

tools can be effectively used to predict both the acoustic wave propagations inside the inlet duct and the directivity patterns of the radiated sound in the far field.

A CAA noise prediction tool greatly assists in designing turbo fan engines by reducing the number of physical prototype builds and tests. Better physical insights are also obtained through virtual parametric studies that are typically more comprehensively done than if done physically. The power of such a tool is enhanced when it is used in conjunction with an optimization program. Without a complete knowledge of the physics involved in the product development, the user of the tool has to, to a certain degree, adopt the method of trial and error to find a design that meets the requirements. Manpower is spent in analyzing results, deciding the next design to try, and re-setting up the model, etc. When multiple design variables are involved, it is a serious challenge for a designer to think in a multi-dimensional design space, and only a limited portion of the design space is explored. The result of such a heavily human involved design loop may be time-consuming and far from the best possible design. On the other hand, in an optimization process, an optimizer takes much of the human work.

A noise prediction and optimization system for turbofan engine inlet duct design is developed in this thesis. Such a system naturally consists of a) a tool for predicting acoustic fields inside and radiated from a turbofan engine inlet duct and b) an optimizer that finds optimum design parameters toward a certain requirement on noise emission. Several design scenarios of practical significance are exercised with the noise prediction and optimization system. In the first two of them, the acoustic power emitted from a engine inlet duct is minimized by finding either the optimum duct geometry or the liner

impedance. In the third scenario, the overall noise level in an affected region during a take-off or landing phase is minimized by finding the most cost-effective liner layout.

Active noise control is an increasingly attractive topic on attenuation of jet engine inlet duct noise. The traditional approach is to employ a passive duct liner in the walls of the engine nacelle. Since the performance of these conventional passive liners depends on the source level and spectrum as well as the mean flow, [37] traditional passive liners with fixed impedance properties may not provide the maximum noise suppression due to the inability of adjusting liner impedance properties to achieve the optimum impedance. In order to suppress the noise more effectively, the impedance properties may need to be adaptively adjusted to accommodate the continuously changing mean flow conditions and the spectra of the noise sources. This is the essential idea of truly active noise control. Naturally, the realization of such noise control requires a) a liner whose impedance properties are adjustable and b) an algorithm that determines the optimum impedance properties. One objective of this thesis is to establish a design for the coupling of a CAA time-domain method with an optimizer for adaptive noise control. Although such noise control is still not a truly active noise control, it is a large step toward truly active noise control as compared with the traditional passive noise control.

### **1.3 Thesis Outline**

Chapters 2, 3 and 4 are toward the methodology of CAA while topics on its applications are discussed in Chapters 5, 6 and 7. Conclusions are given in Chapter 8.

In Chapter 2, the effects of optimization parameters,  $\beta_0$ ,  $\lambda$  and  $\sigma$  on the characteristics of broadband optimized upwind schemes are systematically studied. An

approach for designing high-order optimized upwind and central finite difference schemes is presented. In this approach, numerical schemes are optimized at several discrete frequencies instead of over a range of wavenumber. These optimized multi-component schemes, as referred to in this thesis, are very accurate to predict an acoustic wave of dominant wavenumbers.

Chapter 3 is dedicated to verify the time-domain broadband impedance boundary conditions formulated by Tam and Auriault. [49] A three dimensional acoustic wave propagation problem with an impedance boundary is proposed as a test problem. Its analytical solution is derived and evaluated. The test problem is then numerically solved using the time-domain broadband impedance boundary condition implemented in a CAA code and the results are compared with the analytical solution.

Chapter 4 is to verify the above mentioned formulation of the impedance boundary condition in a duct environment. The CAA code is used to solve a semi-infinite two-dimensional duct problem with an acoustic liner with or without a sheared mean flow. In addition, the formulation with the CAA code is validated by the experimental data from the NASA Langley flow impedance tube facility. In both the verification and the validation problems, the no-slip condition is assumed for the mean flow to avoid the controversy over the condition of particle displacement continuity and the condition of particle velocity continuity, and also to ensure the well-posedness of a time-domain broadband impedance boundary condition.

In Chapter 5, a time-domain method is developed that can separate the undesired instability wave solution under a critical sheared mean flow condition from the acoustic solution of the linearized Euler equations. The previously developed CAA code is used to

demonstrate the effectiveness of the method by solving an acoustic propagation problem with a three-frequency sound source under a critical sheared flow condition.

In Chapter 6, a design of an adaptive noise control system (ANC) is proposed. The system consists of two primary components, an expert subsystem with an acoustic prediction code coupled with an optimizer and a liner with controllable impedance properties. For an acoustic field under the influence of a noise source, a liner and a mean flow condition, an optimization process is executed by the expert subsystem in search of a set of required impedance parameters that minimize the difference between the current and the desired acoustic fields. The liner properties then can be adjusted adaptively to the required impedance parameters. The feasibility and potential of the design concept are demonstrated by using the previously developed CAA code and the three-parameter impedance model of the Helmholtz type.

A noise prediction and optimization system for turbofan inlet duct designs is developed in Chapter 7. This system consists of a noise prediction tool and an optimizer. For the noise prediction tool, a hybrid method is adopted: a CAA method for the duct and its near field and a Kirchhoff method for the far field. The noise prediction system is verified with several test problems, each emphasized on testing a specific aspect of the system. The capabilities of the system are demonstrated with three applications: liner impedance optimization, duct geometry optimization and liner layout optimization.

## 2 HIGH-ORDER OPTIMIZED NUMERICAL SCHEMES FOR COMPUTATIONAL AEROACOUSTICS

In this chapter, the effects of optimization parameters,  $\beta_0$ ,  $\lambda$  and  $\sigma$  on the characteristics of broadband optimized upwind schemes are first systematically studied. A new approach for designing high-order optimized schemes is then presented.

### 2.1 High-Order Optimized Upwind Broadband Schemes

Acoustic problems are governed by the linearized Euler equations. To simplify, consider the one-dimensional scalar modal wave equation, with  $c$  being the speed of sound,

$$\frac{\partial u}{\partial t} + c \frac{\partial u}{\partial x} = 0 \quad (2.1)$$

Suppose we are using a stencil with  $N$  points to the left and  $M$  points to the right. The spatial derivative  $\partial u / \partial x$  in Equation (2.1) can be approximated by a finite difference on a uniform grid of spacing  $\Delta x$  in the general form

$$\left( \frac{\partial u}{\partial x} \right)_l = \frac{1}{\Delta x} \sum_{j=-N}^M a_j u_{l+j} \quad (2.2)$$

where  $\left( \frac{\partial u}{\partial x} \right)_l = \frac{\partial u}{\partial x}(l\Delta x, t)$ ,  $u_{l+j} = u[(l+j)\Delta x, t]$  and the coefficients  $a_j$  are determined by the specific schemes, one of which, referred to as “standard” in this chapter, is purely based on Taylor series expansion. Obviously a standard scheme has the maximum order of accuracy with a given stencil. However this property does not necessarily guarantee that the scheme satisfies the dispersion relation to a maximum

extend for a given wavenumber. In other words, the numerical wavenumber  $\bar{\alpha}$  defined in Equation (2.3) is not optimized to be as close to the wavenumber  $\alpha$  as possible.

$$\bar{\alpha} = -\frac{i}{\Delta x} \sum_{j=-N}^M a_j \exp(ij\alpha\Delta x) \quad (2.3)$$

Instead of achieving the maximum order of accuracy by the Taylor expansion, the strategy applied to optimized schemes is to set some coefficients in the finite difference approximation free so that they can be used for minimizing the dispersion and the dissipation errors of the schemes. Specifically the  $L_2$  norm of the error introduced by the approximation of the non-dimensional numerical wavenumber  $\bar{\alpha}\Delta x$  to the non-dimensional exact wavenumber  $\alpha\Delta x$  is defined as [46]

$$E = \int_{-\beta_0}^{\beta_0} |\bar{\alpha}\Delta x - \alpha\Delta x|^2 d(\alpha\Delta x) \quad (2.4)$$

For optimized upwind schemes, the numerical wavenumber,  $\bar{\alpha}\Delta x$ , is a complex number, and the integrated error  $E$  is considered as [67]

$$E = \int_{-\beta_0}^{\beta_0} \left\{ \lambda [\text{Re}(\bar{\alpha}\Delta x) - \alpha\Delta x]^2 + (1 - \lambda) \left[ \text{Im}(\bar{\alpha}\Delta x) + \exp(-\ln 2((|\alpha\Delta x| - \pi)/\sigma)^2) \right]^2 \right\} d(\alpha\Delta x) \quad (2.5)$$

where  $\text{Re}$  and  $\text{Im}$  denote the real and imaginary parts, respectively,  $\beta_0$  defines the range of wavenumber for optimization,  $\lambda$  is a weighting factor and  $\sigma$  is a control parameter which determines how the imaginary part of the numerical wavenumber approaches to zero. The integrated error  $E$  is then minimized with respect to coefficients  $a_j$  that are chosen as free parameters,

$$\frac{\partial E}{\partial a_j} = 0 \quad (2.6)$$

It is known from the previous work [21, 22, 45] that if the range of wavenumber is too large the oscillations or overshoot observed in both the real and the imaginary parts of the numerical wavenumber will increase. However, using a small value of  $\beta_0$  will not be able to exploit the full potential of the optimized schemes. From the current investigation it is noted that all the three parameters  $\beta_0$ ,  $\lambda$  and  $\sigma$  in Equation (2.5) can be adjusted to improve the optimized upwind schemes. The objective here is then to study the effects of each individual parameter on the dispersion and the dissipation errors of the schemes. A 7-point stencil with 4 points to the left and 2 points to the right is used for all the schemes considered in this section. Since the optimization performed in this section is over a range of wavenumber, the schemes are referred to as the optimized broadband schemes, as distinguished from the optimized schemes studied in the next section.

At first, the effects of the parameter  $\beta_0$  are investigated. It is concluded from the previous work [21, 22, 45] that although using a small value of  $\beta_0$  does not allow us to take advantage of the optimized schemes to their full potential, it, however, does reduce the dispersion and the dissipation errors of the schemes. Our results shown in Figure 2.1 indicate that this is not always the case when there are other parameters involved during the optimization process. In Figure 2.1 the Fourier analysis of the optimized upwind broadband schemes with  $\beta_0 = \pi/2$  and  $\pi/3$  is shown along with that of the standard Taylor scheme. The parameters  $\lambda$  and  $\sigma$  are considered as  $\lambda = 0.9661$  and  $\sigma = 0.2795\pi$  for both of the optimized schemes. It can be seen that the deviation from the exact solution increases for both the real and the imaginary parts of the numerical wavenumber with the range of wavenumber decreased from  $\beta_0 = \pi/2$  to  $\beta_0 = \pi/3$ .

As a matter of fact, the accuracy of the optimized scheme with  $\beta_0 = \pi/3$  is even worse than that of the standard Taylor scheme. To improve the scheme with  $\beta_0 = \pi/3$  one has to search for optimum values of parameters  $\lambda$  and  $\sigma$ . Therefore, decreasing the range of wavenumber for optimization alone does not always improve the scheme. In Figure 2.2 the Fourier analysis of the optimized schemes with  $\beta_0 = \pi/2$  and  $\lambda = 0.9661$  is shown for different values of the parameter  $\sigma$ . As we can see, the effect is monotonic in the range of the parameter  $\sigma$  tested here. It is interesting to note in Figure 2.2 (a) that the three curves for different values of  $\sigma$  intersect at a point where  $\alpha\Delta x$  is a little less than the given range of wavenumber  $\beta_0$  ( $\beta_0 = \pi/2$ ). It seems that there is a better value for  $\sigma$  at which the deviation from the exact solution is overall relatively small for a given optimization range. Figure 2.2 (b), shows that the scheme passes through the exact solution at a relatively larger value of  $\alpha\Delta x$  for the smallest value of  $\sigma$ , but a significant overshoot of the dissipation error makes the scheme unstable. Similar behavior of the dispersion and the dissipation errors are shown in Figure 2.3 with the parameter  $\lambda$  varied. In Figure 2.3 the parameters  $\beta_0$  and  $\sigma$  are given as  $\beta_0 = \pi/2$  and  $\sigma = 0.2795\pi$  for all the schemes.

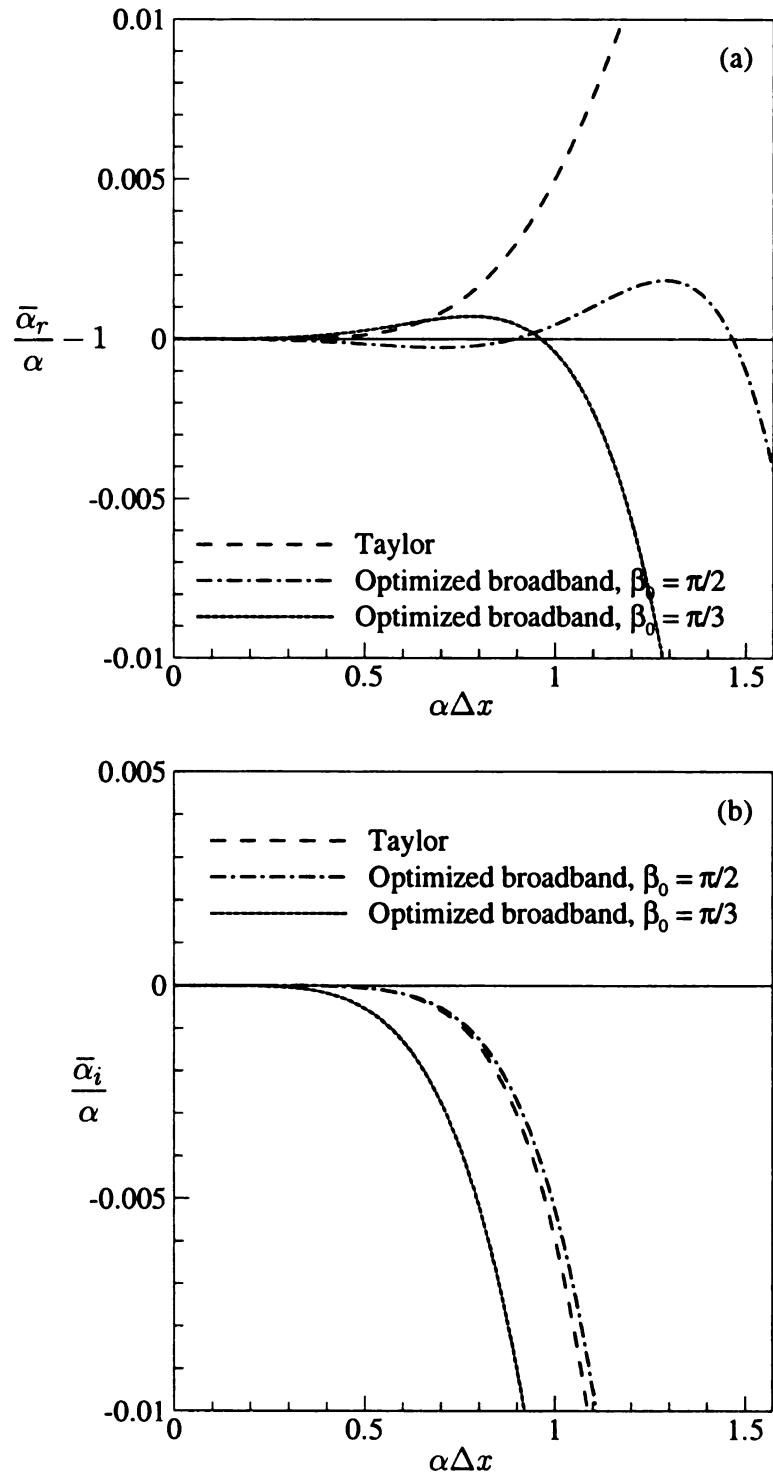


**Figure 2.1** Comparisons of the optimized upwind broadband schemes ( $\lambda = 0.9661$  and  $\sigma = 0.2795\pi$ ) with the standard Taylor scheme. (a)  $\bar{\alpha}_r / \alpha - 1$  versus  $\alpha\Delta x$ ; (b)  $\bar{\alpha}_i / \alpha$  versus  $\alpha\Delta x$ .

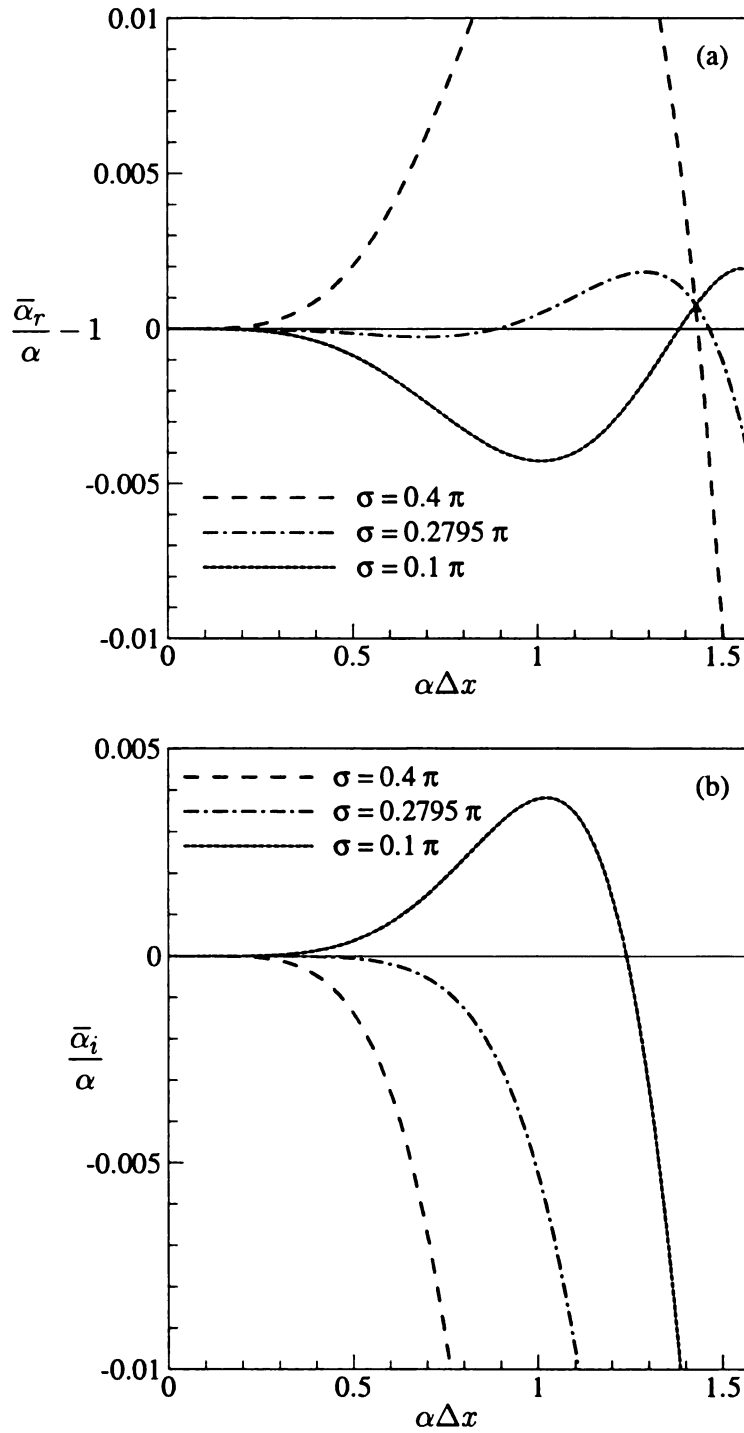


**Figure 2.2** The effect of the parameter  $\sigma$  on an optimized upwind broadband scheme with  $\beta_0 = \pi/2$  and  $\lambda = 0.9661$ . (a)  $\bar{\alpha}_r/\alpha - 1$  versus  $\alpha\Delta x$ ; (b)  $\bar{\alpha}_i/\alpha$  versus  $\alpha\Delta x$ .

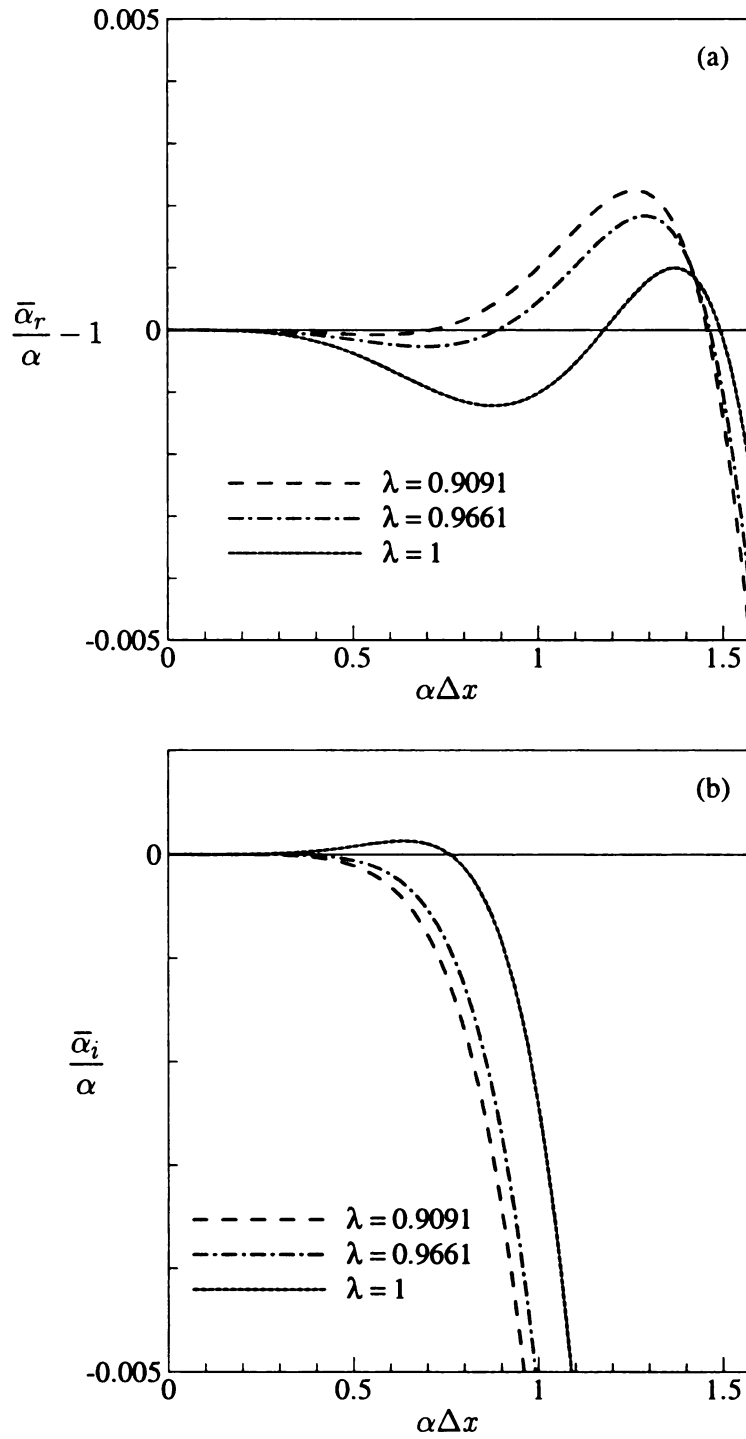


**Figure 2.3** The effect of the parameter  $\lambda$  on an optimized upwind broadband scheme with  $\beta_0 = \pi/2$  and  $\sigma = 0.2795\pi$ . (a)  $\bar{\alpha}_r/\alpha - 1$  versus  $\alpha\Delta x$ ; (b)  $\bar{\alpha}_i/\alpha$  versus  $\alpha\Delta x$ .

From the results shown above, it is concluded that all the three parameters,  $\beta_0$ ,  $\lambda$  and  $\sigma$  affect the characteristics of the optimized upwind broadband schemes. The improvement of the schemes is limited since increasing the accuracy for relatively large values of  $\alpha\Delta x$  is at the expense of decreasing the accuracy for smaller values of  $\alpha\Delta x$ . A practical approach is to control the errors by adjusting the available parameters in such a way that all the wavenumbers in the range of interest is reasonably balanced. This is particularly important when the schemes are used to solve waves with broadband wavenumbers.

## 2.2 High-Order Optimized Multi-Component Schemes

High-order schemes discussed in the last section are optimized over a given range of wavenumber. As we have seen, for a given range of wavenumber the parameters  $\lambda$  and  $\sigma$  also affect the characteristics of the optimized upwind schemes. For a scheme that gives an accurate result for relatively large values of  $\alpha\Delta x$ , the deviation from the exact solution for smaller values of  $\alpha\Delta x$  could become excessive. In order to improve the optimized upwind schemes for smaller values of  $\alpha\Delta x$ , one has to find optimum values for parameters  $\lambda$  and  $\sigma$  over a given optimization range of wavenumber. Unfortunately the improvement of the scheme for smaller values of  $\alpha\Delta x$  is only possible at the expense of decreasing the range of wavenumber,  $\beta_0$ , over which the scheme is capable of giving an accurate solution. The question, then, arises if it is possible to construct a scheme that can give accurate solutions for waves with both high and low wavenumber components. The main objective of this section is to design such a scheme that is accurate and efficient for waves with both large and small wavenumbers. Since it is not uncommon for acoustic waves to have several dominant wavenumbers ranging from

small to large, the scheme is, therefore, optimized for these dominant wavenumbers. To construct the coefficients,  $a_j$ , of such a scheme, instead of minimizing the integrated error  $E$  for a given range of wavenumber, the numerical wavenumber,  $\alpha\Delta x$ , is set to be equal to the actual wavenumber,  $\alpha\Delta x$ , at these dominant wavenumbers. Therefore for each dominant wavenumber, the following two equations have to be satisfied.

$$\operatorname{Re}(\bar{\alpha}\Delta x) = \sum_{j=-N}^M a_j \sin(j\alpha\Delta x) = \alpha\Delta x \quad (2.7)$$

$$\operatorname{Im}(\bar{\alpha}\Delta x) = - \sum_{j=-N}^M a_j \cos(j\alpha\Delta x) = -\varepsilon \quad (2.8)$$

where  $\varepsilon$  is a small positive number to prevents the scheme from becoming unstable at these dominant wavenumbers as time increases. If the number of dominant wavenumbers is  $P$ , then the number of equations used for matching the numerical and the actual wavenumbers is  $2P$ . In order to construct a scheme with a given order of accuracy, additional equations from the Taylor series expansions

$$\sum_{j=-N}^M a_j = 0 \quad (2.9)$$

$$\sum_{j=-N}^M a_j j = 1 \quad (2.10)$$

$$\sum_{j=-N}^M a_j j^k = 0, \quad k = 2, 3, \dots, M + N - 2P \quad (2.11)$$

are needed. The nominal accuracy of the scheme is of  $(M + N - 2P)$ th order. Noted that the number of stencil points has to be chosen accordingly in order to have a certain order of accuracy. In the current investigation, the upwind scheme with a 9-point stencil

is optimized for three selected wavenumbers,  $11\pi/60$ ,  $7\pi/30$  and  $\pi/3$ , with grid spacing  $\Delta x$  given as 1 and  $\varepsilon = 10^{-5}$ . The coefficients,  $a_j^{NM}$  (with  $N = 5$  and  $M = 3$ ), of the optimized 3-component scheme with 2nd-order accuracy, along with the standard Taylor 8th-order scheme and a 6th-order optimized broadband scheme ( $\alpha\Delta x$ ,  $\lambda = 0.9962$ ,  $\sigma = 0.2795\pi$ ) are calculated and given in Table 2.1. It is worth mentioning that  $a_{-j}^{MN} = -a_j^{NM}$ .

**Table 2.1** The coefficients of three schemes using the same stencil

	Taylor	Optimized broadband	Optimized 3-component scheme
$a_{-5}^{53}$	-0.003571428571429	-0.003230147260265	-0.005604334153557
$a_{-4}^{53}$	0.035714285714286	0.032070834858131	0.045751714302010
$a_{-3}^{53}$	-0.166666666666667	-0.150718387386172	-0.184410450650187
$a_{-2}^{53}$	0.500000000000000	0.461711038871108	0.505608972029783
$a_{-1}^{53}$	-1.250000000000000	-1.194148295379005	-1.222126953455600
$a_0^{53}$	0.449999999999999	0.398926233735301	0.399314635216253
$a_1^{53}$	0.500000000000001	0.528733084416301	0.541020210497248
$a_2^{53}$	-0.071428571428572	-0.080551224485787	-0.088485995954237
$a_3^{53}$	0.005952380952381	0.007206862630388	0.008932202168292

The Fourier analysis of the three schemes is shown in Figure 2.4. We can see that both the dispersion and the dissipation errors of the 3-component scheme are kept at a very low level for quite a wide range of  $\alpha\Delta x$ . At the wavenumbers,  $11\pi/60$ ,  $\alpha\Delta x$  and  $\pi/3$ , for which the optimization of the scheme is performed, the dispersion error is as small as zero and the dissipation error is a minimum (it cannot be given as zero due to the stability consideration). In order to examine the region of smaller  $\alpha\Delta x$  more clearly, an

enlarged plot of Figure 2.4 is given in Figure 2.5 for the range of  $\bar{\alpha}_r / \alpha - 1$ . It is shown in Figure 2.5 (a) that the three-component scheme passes through the exact solution at the three selected wavenumbers, but an oscillatory behavior around the exact solution with small amplitudes is observed. It is noted from Figure 2.5 (b) that the imaginary part of the numerical wavenumber  $\bar{\alpha}_i \Delta x$  is greater than zero in the region of  $0.79 < \alpha \Delta x < 1.04$ . These positive values of the imaginary part of the numerical wavenumber, although small in magnitudes, imply the 3-component scheme constructed here would eventually lead to an unstable solution for waves with a wavenumber  $\alpha \Delta x$  falling into this region. However, for waves with the three selected dominant wavenumbers, the 3-component scheme is stable and able to give minimum dispersion and dissipation errors. We will discuss how to avoid the stability problem of the 3-component scheme for broadband waves later in this section. We can also see from Figure 2.4 that the highest wavenumber for which the dispersion and dissipation errors are minimum is around  $\alpha \Delta x = \pi/3$  for the 3-component scheme. The scheme, therefore, can accurately resolve a wave with a number of points per wavelength (*PPW*) as low as 6. However, the other two schemes shown in Figure 2.4 begin to deviate from the exact solution at much smaller wavenumbers.

In order to test the effectiveness and accuracy of the 3-component scheme, the dimensionless one-dimensional Euler equations

$$\frac{\partial}{\partial t} \begin{bmatrix} u \\ p \end{bmatrix} + \frac{\partial}{\partial x} \begin{bmatrix} p \\ u \end{bmatrix} = 0 \quad (2.12)$$

are solved numerically for two wave propagation problems using all the three schemes given in Table 2.1. The flux vector splitting method is used and the Jacobian matrix is

split according to positive or negative eigenvalues. For all the three schemes, the coefficients used for the time discretization are the same as those derived by Tam et al [47].

First we consider a wave with three sinusoidal components of different wavenumbers,

$$\begin{aligned}
 u(x, t) = p(x, t) = & 0.3 \cos\left[\frac{\pi}{3}(x - t) - 1.0\right] \\
 & + 1.0 \cos\left[\frac{7\pi}{30}(x - t) + 0.1\right] \\
 & + 1.0 \cos\left[\frac{11\pi}{60}(x - t) - 0.7\right]
 \end{aligned} \tag{2.13}$$

The computational domain is given as  $-120 \leq x \leq 0$  and the periodic boundary conditions are imposed at the both boundaries. The grid size used by all the three schemes is considered as  $\Delta x = 1.0$ , i.e.  $PPW = 6$  for the highest wavenumber component,  $\alpha = \pi/3$ . The time step is given as  $\Delta t = 0.1$ . After the wave has traveled a distance of  $120000\Delta x$ , or 1000 fundamental wavelengths in this case, the numerical solutions from the three schemes are compared with the analytical solution in Figure 2.6 (a). As expected the 3-component scheme gives the most accurate result since the scheme is optimized for the three dominant wavenumbers. The advantage of the 3-component scheme can be demonstrated more clearly by comparing the errors of solutions from the three schemes (see Figure 2.6 (b)). It is known that the optimized broadband schemes, although optimized for the range of  $\beta_0 \leq \pi/2$  or  $\pi/3$ , cannot give satisfactory results when using  $PPW = 6$ . Results shown in Figure 2.6 (b) substantiate the claim that it is necessary for the optimized broadband scheme to use more  $PPW$  (e.g. with  $PPW = 10$ ) to achieve a reasonably accurate solution. Therefore these schemes are not always suitable to predict wave propagation accurately and economically (e.g. with

$PPW = 6$ ). For acoustic waves with dominant wavenumbers, the advantage of using multi-component schemes is that the schemes not only accurately predict the solution but also use a minimum  $PPW$  (e.g.  $PPW = 6$ ) for the component of the highest wavenumber (e.g.  $\bar{\alpha}_i / \alpha$ ). Since the deviation from the exact solution for smaller values of  $\alpha\Delta x$  is not excessive for the 3-component scheme (see Figure 2.4 and Figure 2.5), the smaller wavenumber components can be easily resolved by the scheme due to their relatively large individual  $PPW$ 's.

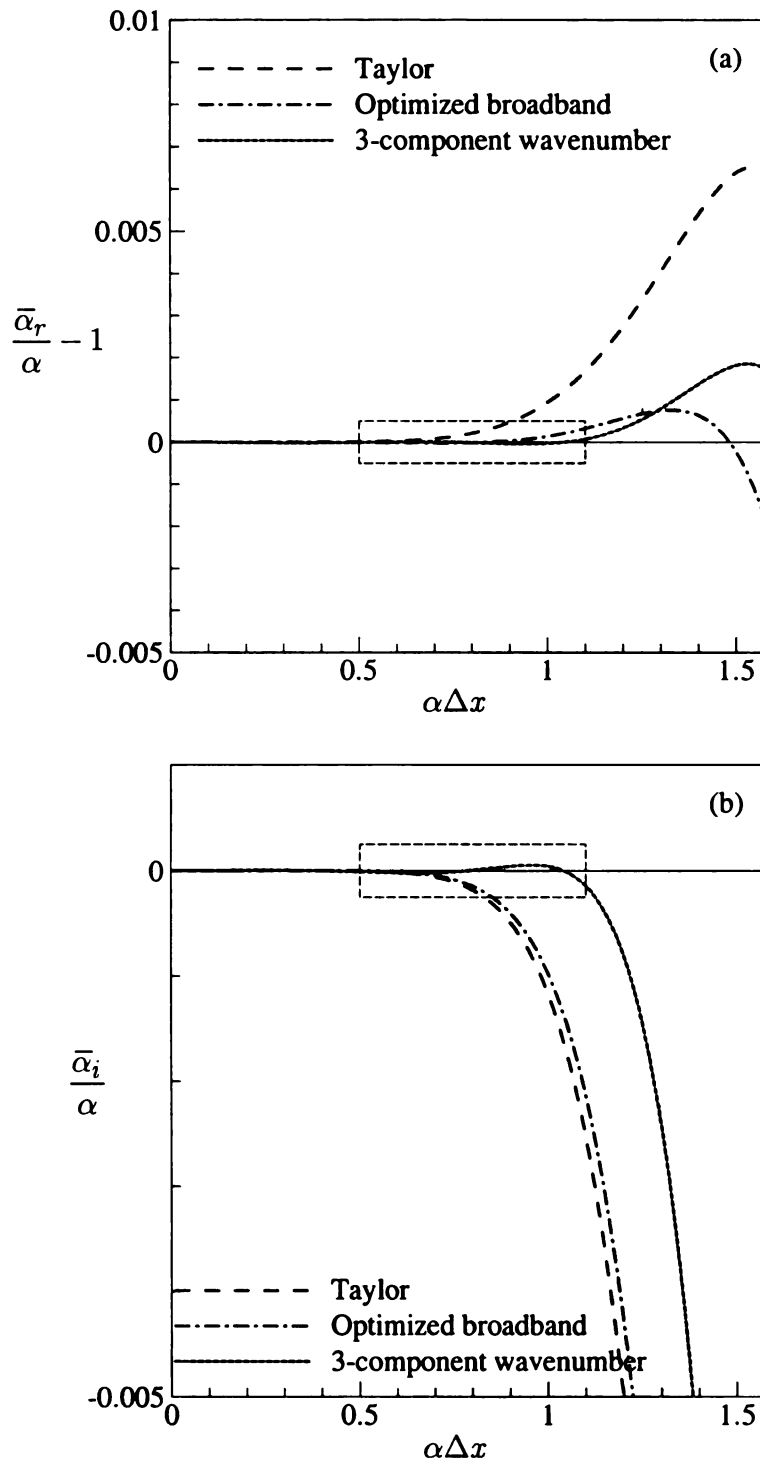


**Figure 2.4** Comparisons of the optimized upwind 3-component scheme ( $\alpha = 11\pi/60, 7\pi/30$  and  $\pi/3, \varepsilon = 10^{-5}$ ), the optimized upwind broadband scheme ( $\beta_0 = \pi/2, \lambda = 0.9962, \sigma = 0.2795\pi$ ) and the standard Taylor scheme (a)  $\bar{\alpha}_r/\alpha - 1$  versus  $\alpha\Delta x$ ; (b)  $\bar{\alpha}_i/\alpha$  versus  $\alpha\Delta x$ .

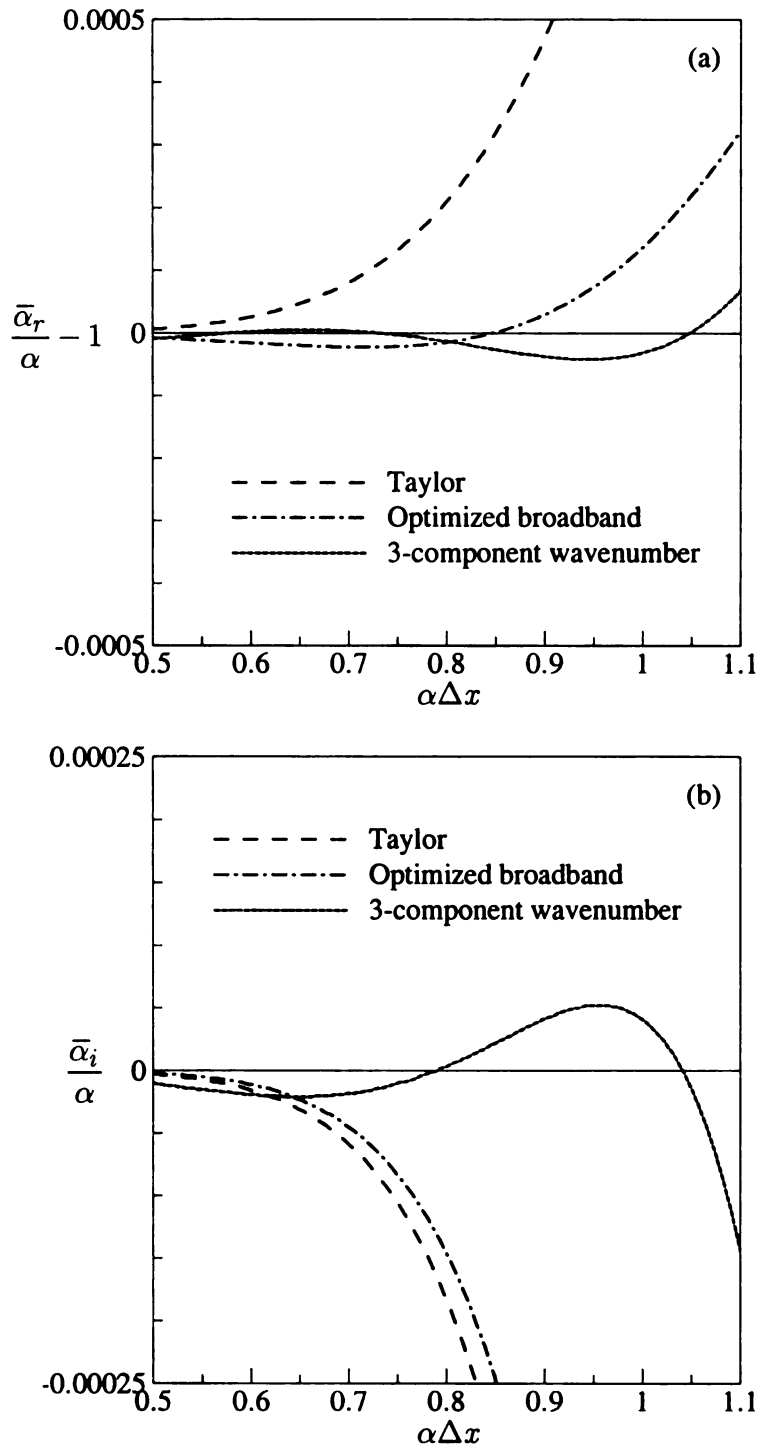


**Figure 2.5** Enlarged plots of the areas bounded with dashed lines in Figure 2.4. (a)  $\bar{\alpha}_r / \alpha - 1$  versus  $\alpha\Delta x$ ; (b)  $\bar{\alpha}_i / \alpha$  versus  $\alpha\Delta x$ .

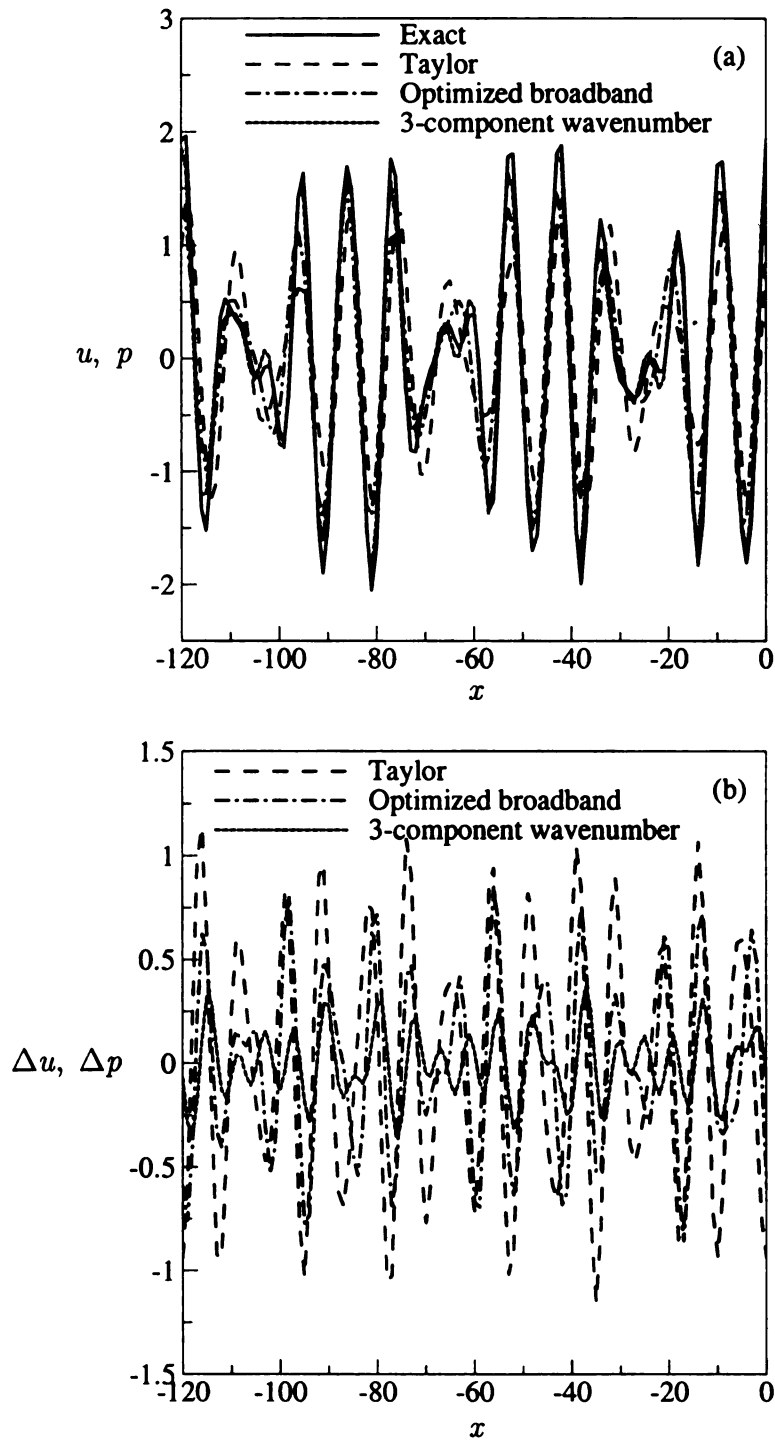


**Figure 2.6** The results of the acoustic wave propagation with the three dominant wavenumbers, predicted by different numerical schemes. (a) velocity or pressure perturbation after  $120000\Delta x$  (1000 fundamental wavelengths) propagation; (b) local corresponding errors.

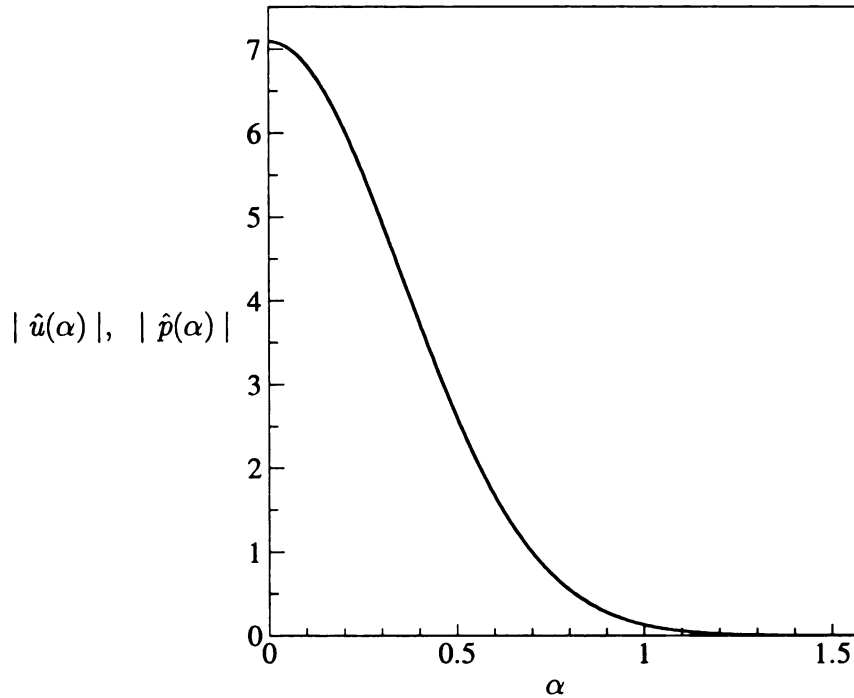


**Figure 2.7** The wavenumber spectrum of the broadband wave.

Until now we have demonstrated that the 3-component scheme has the advantage when resolving waves with dominant wavenumbers. It is also interesting to find out if the scheme can be used to solve broadband waves. For this purpose, a Gaussian wave is considered instead of the wave with the three sinusoidal components. The dimensionless velocity and pressure for the Gaussian wave are given as

$$u(x, t) = p(x, t) = \exp\left[-\frac{(x - t + 60)^2}{4^2}\right] \quad (2.14)$$

The peak of the Gaussian wave is located at  $x = -60$ . The computational domain, the boundary conditions, the grid size and the time step used here are the same as those in the previous problem. The Fourier transform of Equation (2.14), when performed with respect to  $x$ , is

$$\hat{u}(\alpha) = \hat{p}(\alpha) = 4\sqrt{\pi} \exp[i\alpha(-t + 60) - 4\alpha^2] \quad (2.15)$$

The transform gives the wavenumber spectrum of the Gaussian wave and the module of the transform is plotted in Figure 2.7. The horizontal axis in Figure 2.7 is the same as that in Figure 2.4 since the grid size  $\Delta x$  is given as 1. It can be seen from these two figures that the 3-component scheme gives slightly better characteristics than the other two schemes in the region of  $0 < \alpha\Delta x < \pi/3$ , where most of the wavenumber components of the Gaussian wave exist. In Figure 2.8, the solutions from all the three schemes are compared with the exact solution after the wave has traveled a distance of  $12000\Delta x$ . As expected, the 3-component scheme gives a slightly better result. However, as mentioned earlier, the imaginary part of the numerical wavenumber for the 3-component scheme is positive for some wavenumbers. Although the magnitudes of these positive numbers are small, they will eventually lead to an unstable solution for a broadband wave. In order to avoid the stability problem when solving broadband waves, a modification to the upwind multi-component schemes is needed. There are some approaches we could use to modify the optimized upwind multi-component schemes such that the imaginary part of the numerical wavenumber either remains negative or is positive for some wavenumbers, but with orders of magnitude smaller amplitudes. Another approach to avoid the stability problem is to consider central multi-component schemes instead of upwind multi-component schemes with the understanding that artificial dissipation is required for central difference schemes. Three central 1-component schemes and three central 2-component schemes are constructed for several values of wavenumbers selected for optimizations. A 7-point stencil is used for all the optimized central schemes discussed below. The orders of accuracy for these optimized

central schemes are the 4th-order for the 1-component schemes and the 2nd-order for the 2-components schemes. In Figure 2.9 the Fourier analysis of these 1-component and 2-component schemes is shown along with that of Tam's 4th-order, 7-point stencil optimized central broadband schemes. As is shown in Figure 2.9, the 1-component schemes optimized for wavenumbers  $\alpha\Delta x = 0.9571$  and  $\alpha\Delta x = 1.4215$  are nearly identical to Tam's broadband central schemes with  $\beta_0 = \pi/3$  and  $\beta_0 = \pi/2$ , respectively. In fact, by adjusting the value of the wavenumber for optimization, the 1-component scheme is almost identical to the optimized central broadband scheme with a corresponding range of optimization. The results in Figure 2.9 also show a marked improvement for the 2-component schemes. By adjusting the values of wavenumbers for optimization, the 2-component schemes can always give better characteristics than those of Tam's broadband schemes. The characteristics of a 2-component scheme can be further improved by adding a 3rd wavenumber for optimization, but the number of stencil points has to be increased accordingly.

The results shown in this section indicate that when solving acoustic waves with a few dominant wavenumbers, the optimized multi-component schemes are superior in terms of accuracy and efficiency to the optimized broadband schemes. In addition, the performance of the optimized central multi-component schemes, if constructed accordingly, is at least as good as the optimized central broadband schemes while solving broadband waves.

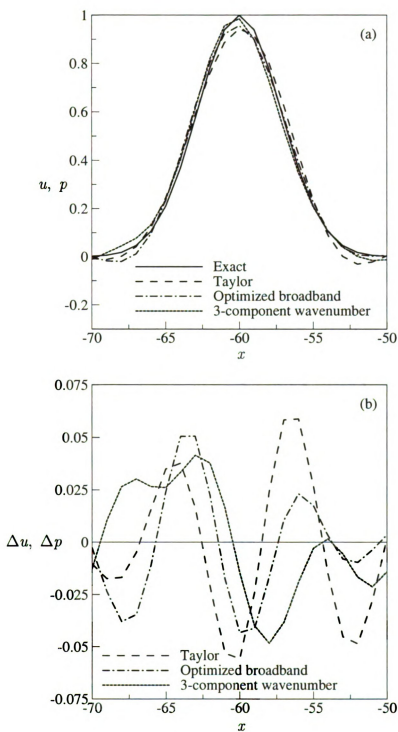


**Figure 2.8** The results of the broadband acoustic wave after traveling a distance of  $12000\Delta x$  predicted by different schemes. (a) wave shapes as compared to the exact solution, (b) local corresponding errors.

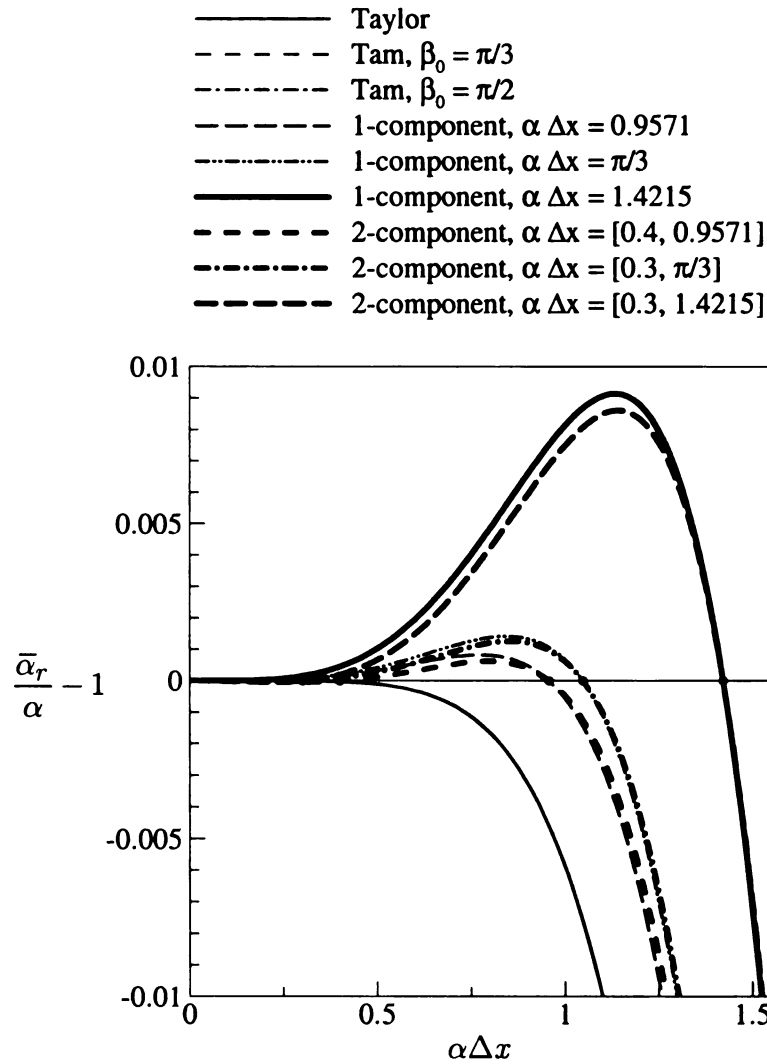


**Figure 2.9** Comparisons of the central multi-component schemes with Tam's central schemes and the standard Taylor scheme. The dots on the horizontal axis indicate the values of  $\alpha\Delta x$  for which the 1- or 2-component schemes are optimized.

### **3 A THREE-DIMENSIONAL BENCHMARK PROBLEM FOR BROADBAND TIME DOMAIN IMPEDANCE BOUNDARY CONDITIONS**

In this chapter, an acoustic wave propagation problem in three dimensions with an impedance boundary is proposed and its analytical solution is derived and evaluated. It is then used as a benchmark problem to test a broadband time domain impedance boundary condition.

#### **3.1 Formulation of the Test Problem**

The test problem is illustrated in Figure 3.1. The domain of interest lies in the ranges of  $-\infty < x < \infty$ ,  $-\infty < y < \infty$  and  $z \geq 0$ . A liner with uniform impedance  $Z(\omega) = \hat{p}(\omega)/\hat{v}_n(\omega)$  is applied at  $z = 0$ , where  $\hat{p}$  and  $\hat{v}_n$  are acoustic pressure and particle velocity  $\hat{v}_n$  normal to the liner (positive when pointing into the liner) in frequency domain. A spherical Gaussian acoustic pressure pulse  $p_0(R) = \exp(-BR^2)$  is initially introduced with zero initial velocity components, where constant  $B > 0$  and  $R$  is the distance to the pulse center at  $S(0, 0, z_S)$ . It is noted that all the quantities in this report are non-dimensionalized such that the speed of sound is unity.

#### **3.2 The Analytical Solution**

The analytical solution of the test problem is considered to be the superposition of three component waves, i.e., the outgoing wave, which diverges from the sphere center, the incoming wave, which converges to the sphere center and the reflected wave by the impedance boundary. A broadband incident wave needs to be decomposed into harmonic waves and a non-plane incident wave needs to be decomposed into plane waves. Then the

reflection of each of the harmonic plane incident wave by the impedance boundary can be determined. The total reflected wave is in a form of an integral of the reflected harmonic plane waves. This is the general idea for deriving the analytical solution to the problem.

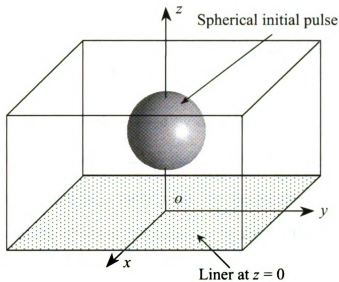


**Figure 3.1** Schematic of the test problem

The outgoing and incoming waves in free space with the same initial condition can be determined, in terms of the velocity potential  $\varphi$  defined by  $\nabla\varphi = \vec{v}$  with spherical symmetry [57], to be

$$\varphi_{out}(R, t) = f(R - t) / R \quad (3.1)$$

$$\varphi_{in}(R, t) = -f(R + t) / R \quad (3.2)$$

where  $R = \sqrt{x^2 + y^2 + (z - z_S)^2}$  and  $f$  is determined from the initial condition to be  $f(r) = -\exp(-Br^2)/(4B)$ , for  $-\infty < r < \infty$ .

For the test problem, the outgoing and incoming waves are not exactly the same as the free space solutions. This is because the actual initial condition is not a complete spherical Gaussian pulse, part of which is outside the semi-infinite space. However, if the

center of the spherical pulse is far away from the impedance boundary, the outside portion of the initial pulse will be of very small amplitude and thus insignificant to the whole problem. Therefore, we can safely assume a complete initial spherical Gaussian pulse for the test problem and approximate its outgoing and incoming waves with the free space solution in Equations (3.1) and (3.2). Such treatment will greatly simplify the analysis.

The reflected wave is determined by considering the incident (outgoing) wave  $\varphi_{out}$  in Equation (3.1) being reflected by the impedance boundary. As stated earlier, the broadband spherical outgoing wave must be decomposed into harmonic plane components to study the effects of the impedance boundary. This decomposition process is done in the following two steps (can be done in the reverse order).

In the first step, the broadband outgoing spherical wave  $\varphi_{out}$  is decomposed into harmonic outgoing spherical waves

$$\varphi_{out}(R, t) = \int_{-\infty}^{\infty} \hat{f}(k_0) \exp[ik_0(R - t)] / R dk_0 \quad (3.3)$$

by resolving function  $f(R - t)$  into its Fourier transform

$$\hat{f}(k_0) = \exp[-k_0^2 / (4B)] / (8B\sqrt{\pi B})$$

which is real and even due to the fact that  $f(R - t)$  is real, even and summable. [5] Obviously the expression  $\exp[ik_0(R - t)] / R$  in the integrand of Equation (3.3) represents a harmonic outgoing spherical wave with an angular frequency/wavenumber  $k_0$  (the speed of sound is unity). Since  $\hat{f}(k_0)$  is real and even, the integration in Equation (3.3) can be performed only over the non-negative range of angular frequency/wavenumber  $k_0$  with the real part of the integral unchanged,

$$\varphi_{out}(R, t) = 2 \operatorname{Re} \left\{ \int_0^\infty \hat{f}(k_0) \exp(-ik_0 t) \exp(ik_0 R) / R dk_0 \right\} \quad (3.4)$$

For the sake of convenience, the time dependence is separated from the harmonic spherical wave, which will then be represented only by the term  $\exp(ik_0 R) / R$  in the following derivation.

As the second step of the decomposition process, a harmonic spherical wave  $\exp(ik_0 R) / R$  with a non-negative angular frequency/wavenumber  $k_0$  is decomposed into harmonic plane waves, using Weyl's integral, [38, 40]

$$\exp(ik_0 R) / R = \frac{i}{2\pi} \int_{-\infty}^{\infty} \int_{-\infty}^{\infty} \exp\{i[k_x x + k_y y + k_z(z - z_S)]\} \frac{dk_x dk_y}{k_z}, \text{ for } z > 0 \quad (3.5)$$

where  $\exp\{i[k_x x + k_y y + k_z(z - z_S)]\}$  represents a harmonic plane wave with

$$k_z = \sqrt{k_0^2 - k_x^2 - k_y^2}.$$

By now, the broadband spherical incident wave has been decomposed into harmonic plane waves and thus it is ready to incorporate the effects of the impedance boundary on each of these harmonic plane incident waves. Using the method of mirror image, the reflected wave of each of the harmonic plane waves in the integrand of Equation (3.5) by the impedance boundary is determined to be

$$C_r(k_0, k_z) \exp\{i[k_x x + k_y y + k_z(z + z_S)]\} \quad (3.6)$$

where the reflection coefficient  $C_r(k_0, k_z)$  is determined from the liner impedance  $Z(\omega)$ ,

$$C_r(k_0, k_z) = [Z(k_0)(k_z / k_0) - 1] / [Z(k_0)(k_z / k_0) + 1] \quad (3.7)$$

Corresponding to Equation (3.5), the reflected harmonic (non-plane) outgoing wave is then obtained by integrating the reflected harmonic plane waves in Equation (3.6),

$$\varphi_{k_0, refl}(x, y, z, k_0) = \frac{i}{2\pi} \int_{-\infty}^{\infty} \int_{-\infty}^{\infty} C_r(k_0, k_z) \exp\{i[k_x x + k_y y + k_z(z + z_S)]\} \frac{dk_x dk_y}{k_z} \quad (3.8)$$

Similarly, the reflected wave of the outgoing wave in Equation (3.4) is obtained by integrating the reflected harmonic (non-plane) wave in Equation (3.5),

$$\varphi_{refl}(x, y, z, t) = 2 \operatorname{Re} \left\{ \int_0^{\infty} \hat{f}(k_0) \exp(-ik_0 t) \varphi_{k_0, refl}(R, k_0) dk_0 \right\} \quad (3.9)$$

By changing the variables of integration and separating the real and the imaginary parts of Equation (3.8), we have

$$\begin{aligned} \operatorname{Re}[\varphi_{k_0, refl}(x, y, z, k_0)] &= k_0 \int_{-1}^0 C_1 \sin(k_0 z' \xi - \beta_1) J_0[k_0 r \sqrt{1 - \xi^2}] d\xi \\ &\quad + k_0 \int_0^{\infty} C_2 \cos(\beta_2) e^{-k_0 z' \xi} J_0[k_0 r \sqrt{1 + \xi^2}] d\xi \end{aligned}$$

and

$$\begin{aligned} \operatorname{Im}[\varphi_{k_0, refl}(x, y, z, k_0)] &= k_0 \int_{-1}^0 C_1 \cos(k_0 z' \xi - \beta_1) J_0[k_0 r \sqrt{1 - \xi^2}] d\xi \\ &\quad + k_0 \int_0^{\infty} C_2 \sin(\beta_2) e^{-k_0 z' \xi} J_0[k_0 r \sqrt{1 + \xi^2}] d\xi \end{aligned}$$

where  $J_0$  is the Bessel function of the first kind of order zero and  $C_1$ ,  $C_2$ ,  $\beta_1$  and  $\beta_2$  are the moduli and arguments of reflection coefficients  $C_r(k_0, -k_0\xi)$  and  $C_r(k_0, ik_0\xi)$  defined in Equation (3.7),

$$C_1 = |C_r(k_0, -k_0\xi)|, \quad \beta_1 = \arg[C_r(k_0, -k_0\xi)],$$

$$C_2 = |C_r(k_0, ik_0\xi)|, \quad \beta_2 = \arg[C_r(k_0, ik_0\xi)].$$

By taking the derivatives of the velocity potential, the acoustic pressure and the components of the particle velocity can be determined. Specially, the acoustic pressures associated with the outgoing, incoming and reflected waves are determined from Equations (3.1), (3.2) and (3.9),

$$p_{out}(x, y, z, t) = -\frac{\partial}{\partial t} \varphi_{out}(R, t) = \frac{R-t}{2R} \exp[-B(R-t)^2] \quad (3.10)$$

$$p_{in}(x, y, z, t) = -\frac{\partial}{\partial t} \varphi_{in}(R, t) = \frac{R+t}{2R} \exp[-B(R+t)^2] \quad (3.11)$$

and

$$\begin{aligned} p_{refl}(x, y, z, t) &= -\frac{\partial}{\partial t} \varphi_{refl}(x, y, z, t) \\ &= 2 \int_0^\infty k_0 \hat{f}(k_0) [\sin(k_0 t) \operatorname{Re}(\varphi_{k_0, refl}) - \cos(k_0 t) \operatorname{Im}(\varphi_{k_0, refl})] dk_0 \end{aligned} \quad (3.12)$$

which has to be evaluated using numerical integration. The total acoustic pressure is given by the sum of Equations (3.10), (3.11) and (3.12).

### 3.3 Numerical Implementation

#### 3.3.1 Broadband Dispersion-Relation-Preserving (DRP) Upwind Scheme

A fourth-order, seven-point stencil optimized upwind DRP scheme with the parameters [68] chosen as  $\beta_0 = \pi/2$ ,  $\lambda = 0.0374$ , and  $\sigma = 0.2675\pi$  is used for the numerical simulation of the Euler equations. The approximation coefficients used in the scheme for the interior and boundary points are the same as those listed in Reference [68].

#### 3.3.2 Broadband Time Domain Impedance Boundary Condition

For the impedance of the Helmholtz resonator type characterized by

$$Z(\omega) = R_0 - i(X_{-1}/\omega + X_1\omega) \quad (3.13)$$

where  $R_0$ ,  $X_{-1}$  and  $X_1$  are constant parameters, the broadband time domain impedance boundary condition is given by Tam and Auriault [49] as

$$\frac{\partial p}{\partial t} = R_0 \frac{\partial v_n}{\partial t} - X_{-1} v_n + X_1 \frac{\partial^2 v_n}{\partial t^2} \quad (3.14)$$

where  $p$  and  $v_n$  are the acoustic pressure and the normal acoustic velocity at the impedance boundary (positive when pointing into the impedance liner) in the time

domain. Since in a discrete form, both the Euler equations and the impedance boundary condition (3.14) have to be satisfied on the nodes at the impedance boundary, extra freedom must be introduced to accommodate this requirement. For this purpose, a ghost value for pressure is introduced on a point outside the computational domain one grid spacing away from each of those boundary nodes. For the test problem, the discretized ghost value for pressure at time level  $n$  is

$$p_{i,j,ghost}^{(n)} = \left( \Delta z s_{i,j} - \sum_{l=0}^5 a_l^{15} p_{i,j,l} \right)^{(n)} / a_{-1}^{15} \quad (3.15)$$

where

$$s_{i,j}^{(n+1)} = s_{i,j}^{(n)} + \Delta t \sum_{l=0}^3 b_l \left\{ -\frac{1}{X_1} \left[ \left( \frac{\partial u}{\partial x} + \frac{\partial v}{\partial y} + \frac{\partial w}{\partial z} \right)_{i,j,0} + R_0 s_{i,j} + X_{-1} w_{i,j,0} \right] \right\}^{(n-l)}$$

and  $a_l^{15}$  and  $b_l$  are the coefficients for spatial and temporal discretization of the DRP scheme.

### 3.3.3 Nonreflecting Radiation Boundary Condition

The boundary conditions at all the boundaries other than the impedance boundary should be able to simulate the situation of a semi-infinite space by allowing the waves to leave the finite computational domain without being reflected. This physical condition is approximated by the non-reflecting radiation boundary conditions for the three-dimensional case

$$\left( \frac{\partial}{\partial t} + \frac{\partial}{\partial r} + \frac{1}{r} \right) [\rho, \bar{v}^T, p]^T = 0 \quad (3.16)$$

where  $r$  is the distance between the current boundary point and a fixed point inside the computational domain.

### 3.4 Comparison of the Results

In the test problem, the initial acoustic pressure pulse  $p_0(R) = \exp(-BR^2)$  with  $B = (\ln 2)/25$  is centered at  $S(0,0,30)$ . The three parameters for the impedance model are  $R_0 = 0.2$ ,  $X_{-1} = -0.4758$  and  $X_1 = 2.0938$ .

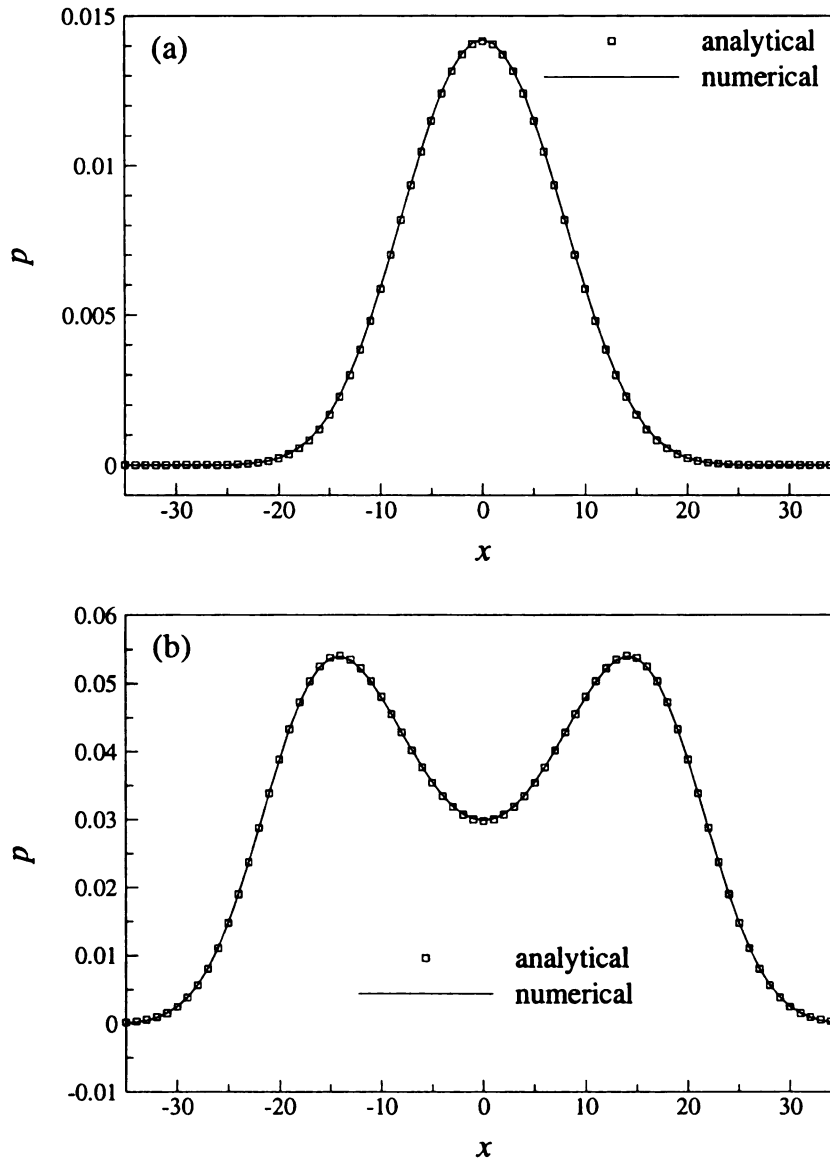


**Figure 3.2** Comparison of the acoustic pressure along the  $x$ -axis at (a)  $t = 20$  and (b)  $t = 30$ .

The results from the numerical simulation are compared with the analytical solution for the test problem. The acoustic pressure along the  $x$ -axis, which is at the impedance boundary, at  $t = 20$  and  $t = 30$  is shown in Figure 3.2 (a) and Figure 3.2 (b). Shown in Figure 3.3 is the acoustic pressure along the  $z$ -axis at  $t = 30$ . The asymmetry about  $z = 30$  where the center of the initial spherical pulse lies shows the effect of the impedance boundary. As we can see in all the figures, the numerical solutions agree very well with the analytical solutions and thus the time domain broadband impedance boundary condition is verified.

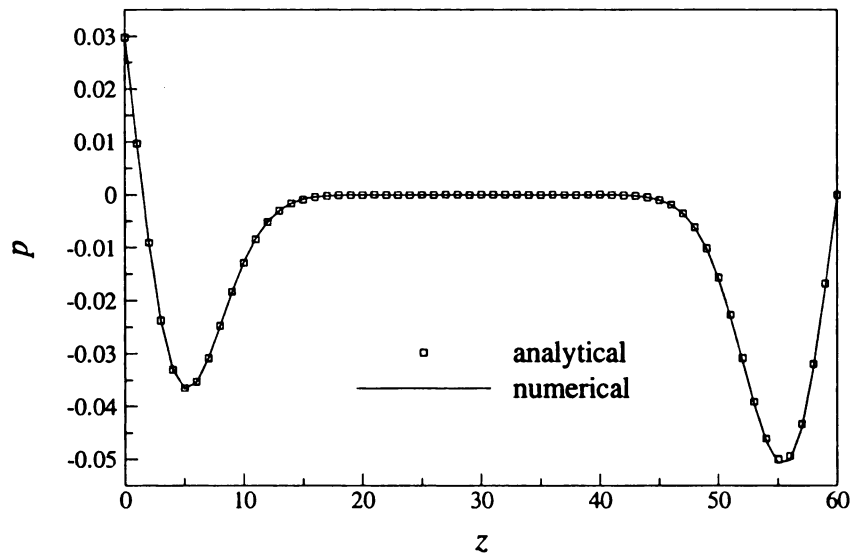


**Figure 3.3** Comparison of the acoustic pressure along the  $z$ -axis at  $t = 30$

## 4 VERIFICATION AND VALIDATION OF A TIME-DOMAIN IMPEDANCE BOUNDARY CONDITION IN LINED DUCTS

In section 4.1, a semi-infinite impedance duct problem is proposed and its analytical solution is given. In addition the numerical scheme is introduced along with the time domain-broadband impedance boundary condition and other relevant types of boundary conditions. The numerical results are compared with those of the analytical solution at the end of the section. In section 4.2, the configuration of the NASA Langley flow impedance tube facility is introduced, for which the numerical method is again implemented and the results are compared with the experimental data. The effects of the exit boundary condition are also discussed.

Unless otherwise stated, variables used in this chapter are dimensionless with  $L = 1\text{ m}$  as the length scale,  $c_0 = 344.283\text{ m/s}$  as the velocity scale,  $\rho_0 = 1.29\text{ kg/m}^3$  as the density scale,  $L/c_0$  as the time scale,  $\rho_0 c_0^2$  as the pressure scale and  $\rho_0 c_0$  as the impedance scale. The harmonic time dependence  $\exp(i\omega t)$  is assumed. Under this convention, the impedance is  $Z = R + iX$ , where  $R$  and  $X$  are the resistance and the reactance.

## 4.1 Verification with Analytical Solution

### 4.1.1 Verification Problem and its Analytical Solution

To verify the time-domain impedance boundary condition, we consider a semi-infinite two-dimensional duct with a hard upper wall and an acoustically treated lower wall. The lower wall is characterized by its frequency dependent impedance

$$Z(\omega) = \hat{p}(\omega) / \hat{v}_n(\omega) \quad (4.1)$$

The mean flow velocity inside the duct is parallel in the  $x$  direction, i.e.,  $M_x = M(y)$  and  $M_y = 0$ . The mean flow density and pressure are constant and equal to  $\rho_0$  and  $\rho_0 c_0^2 / \gamma$ , respectively. Such a duct configuration is shown in Figure 4.1. The orientation of the coordinate system is shown in the figure and its origin is at the lower left corner of the duct.

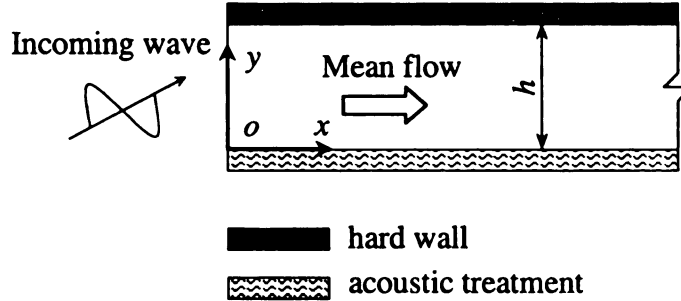


**Figure 4.1** The semi-infinite impedance duct

This problem is governed by the two-dimensional linearized Euler equations (LEE) with a parallel mean flow in the  $x$  direction,

$$\frac{\partial \mathbf{u}}{\partial t} + \mathbf{A} \frac{\partial \mathbf{u}}{\partial x} + \mathbf{B} \frac{\partial \mathbf{u}}{\partial y} + \mathbf{D} \mathbf{u} = \mathbf{0} \quad (4.2)$$

where

$$\mathbf{u} = \begin{bmatrix} \rho \\ u \\ v \\ p \end{bmatrix}, \mathbf{A} = \begin{bmatrix} M(y) & 1 & 0 & 0 \\ 0 & M(y) & 0 & 1 \\ 0 & 0 & M(y) & 0 \\ 0 & 1 & 0 & M(y) \end{bmatrix}, \mathbf{B} = \begin{bmatrix} 0 & 0 & 1 & 0 \\ 0 & 0 & 0 & 0 \\ 0 & 0 & 0 & 1 \\ 0 & 0 & 1 & 0 \end{bmatrix}, \text{ and}$$

$$\mathbf{D} = \begin{bmatrix} 0 & 0 & 0 & 0 \\ 0 & 0 & M'(y) & 0 \\ 0 & 0 & 0 & 0 \\ 0 & 0 & 0 & 0 \end{bmatrix}.$$

When the solution to the LEE is assumed to have the following form

$$\mathbf{u} = \begin{bmatrix} \Phi(y) \\ U(y) \\ V(y) \\ P(y) \end{bmatrix} \exp[i(\omega t - k_x x)] \quad (4.3)$$

Equation (4.2) can be reduced to a second-order ordinary differential equation for  $P(y)$  only,

$$P'' + \frac{2k_x}{\omega - M(y)k_x} M'(y)P' + \{[\omega - M(y)k_x]^2 - k_x^2\}P = 0 \quad (4.4)$$

At the upper boundary of the duct, the boundary condition is given as the hard wall boundary condition

$$P'(h) = 0 \quad (4.5)$$

To give the boundary condition at the acoustic treatment, we have to face a controversy as to whether the condition of particle displacement continuity (PDC) or the condition of particle velocity continuity (PVC) is to be used. When PDC or PVC is satisfied the boundary condition at the lower boundary at  $y = 0$  is

$$Z\omega P' + i[\omega - M(0)k_x]^2 P = 0 \quad (4.6)$$

or

$$ZP' + i[\omega - M(0)k_x]P = 0 \quad (4.7)$$

It is not an intention of this chapter to solve such a controversy. However, if no-slip condition is assumed, e.g., the mean flow is zero, at the acoustic treatment, it is easy to verify that Equation (4.6) is the same as Equation (4.7) and thus the controversy is avoided. On the other hand, if slip condition is assumed instead, the boundary condition (4.6) or its time-domain equivalents will lead to an unstable solution and thus is ill-posed. Stability analysis shows that any time-domain solution with such a boundary condition is prone to stability problems. [49, 52] Although the stability analysis was done in a semi-infinite domain, our numerical results show stability problems even in a duct configuration. For these reasons, the no-slip condition is assumed in the current study. For such a case, both Equation (4.6) and Equation (4.7) are reduced to

$$ZP' + i\omega P = 0 \quad (4.8)$$

Equations (4.4), (4.5) and (4.8) define an eigenvalue problem with  $k_x$  being the eigenvalue. For a general sheared mean flow profile  $M(y)$ , the problem is not analytically solvable and thus numerical procedure must be employed. For the zero mean flow case, the solution (for the right propagating wave) can be given as

$$P(y) = C \cos[k_y(h - y)] \quad (4.9)$$

where constant  $C$  is resulted from solving the eigenvalue problem;  $k_y$  is determined by solving the following transcendental equation

$$Zk_y \tan(k_y h) - i\omega = 0 \quad (4.10)$$

with

$$k_x = \sqrt{\omega^2 - k_y^2} \quad (4.11)$$

The eigenvalue problem has a series of eigenvalues  $k_x$ , each corresponding to a mode allowed in such a duct configuration. We have calculated the least attenuated mode allowed in the configuration shown in Figure 4.1 with duct width  $h = 0.0508$ , frequency  $2000L/c_0$  and specific impedance  $Z = 4.99 + 0.25i$  for the treatment. For the zero mean flow case,  $k_x = 36.2 - 1.94i$ ,  $k_y = 9.13 + 7.67i$  and  $P(y)$  is given by Equation (4.9). For the case with a sheared mean flow  $M(y) = 1.2(y/h)(1 - y/h)$  of centerline Mach number  $M(h/2) = 0.3$ ,  $k_x = 30.0 - 1.36i$  and  $P(y)$  is obtained by numerically solving Equations (4.4), (4.5) and (4.8). These two cases will serve as test cases to verify our numerical methods in subsection 4.1.3.

Once  $P(y)$  is known, the solution to the LEE in Equation (4.2) can be determined by using Equation (4.3) and the following equation,

$$\begin{cases} \Phi(y) = \frac{k_x U(y) + i V'(y)}{\omega - M(y)k_x} \\ U(y) = \frac{k_x}{\omega - M(y)k_x} P(y) - \frac{M'(y)}{[\omega - M(y)k_x]^2} P'(y) \\ V(y) = \frac{i}{\omega - M(y)k_x} P'(y) \end{cases} \quad (4.12)$$

When presenting the calculated results later in subsection 4.1.3, we will use the sound pressure level  $SPL(x)$  and the phase relative to point at  $(0, h)$  along the upper wall. From Equation (4.3),

$$SPL(x) - SPL(0) = 20(\log_{10} e) \operatorname{Im}(k_x)x \quad (4.13)$$

where the sound pressure level at the inlet  $SPL(0)$  is determined by the reference pressure. The phase relative to the phase at point  $(0, h)$  is

$$\varphi(x) = -\text{Re}(k_x)x \quad (4.14)$$

## 4.1.2 Methodology of the Numerical Implementation

### 4.1.2.1 Inlet and Exit Boundary Conditions

When we numerically solve the semi-infinite impedance duct problem, the computational domain can only be a segment of the duct, starting at  $x = 0$  and ending at some  $x > 0$ , for example. To simulate the infinite extension to the right of the duct, it is required that all the outgoing waves leave the computational domain without being reflected at the artificial duct exit. The same requirement applies for the duct inlet at  $x = 0$  with the incoming wave in Equation (4.3) also specified. For these purposes, we implement the Perfectly Matched Layers (PML) boundary conditions in unsplit physical variables [16] in vertical  $x$ -layers (PML regions) left to the inlet and right to the exit,

$$\frac{\partial \mathbf{u}'}{\partial t} + \mathbf{A} \frac{\partial \mathbf{u}'}{\partial x} + \mathbf{B} \frac{\partial \mathbf{u}'}{\partial y} + \mathbf{D} \mathbf{u}' + \sigma_x \mathbf{B} \frac{\partial \mathbf{q}}{\partial y} + \sigma_x \mathbf{u}' + \frac{\sigma_x M(y)}{1 - M^2(y)} \mathbf{A} \mathbf{u}' = 0 \quad (4.15)$$

where  $\mathbf{u}' = \mathbf{u} - \mathbf{u}_{\text{in}}$ , with  $\mathbf{u}_{\text{in}}$  being the incoming wave specified in Equation (4.3), for the inlet boundary condition, and  $\mathbf{u}' = \mathbf{u}$  for the outlet boundary condition.  $\mathbf{q}$  is an auxiliary variable and defined by  $\partial \mathbf{q} / \partial t = \mathbf{u}'$ .  $\sigma_x$  spatially varies and takes the same form as in Reference [16]. At the outer boundaries of the PML regions, a characteristics-based boundary condition is applied to further improve the quality of the absorbing boundary conditions.

We need to point it out that in Reference [16], the PML boundary condition is proposed for a uniform mean flow and its well-posedness is only proved in the same context. In spite of this, our numerical solution as seen later shows the success of the boundary condition for a non-uniform flow.

#### 4.1.2.2 Impedance Boundary Condition

At the acoustically treated wall, the broadband time-domain impedance boundary condition proposed by Tam and Auriault [49] is applied:

$$\frac{\partial p}{\partial t} = R_0 \frac{\partial v_n}{\partial t} - X_{-1}v_n + X_1 \frac{\partial^2 v_n}{\partial t^2} \quad (4.16)$$

where  $R_0$ ,  $X_{-1}$  and  $X_1$  are related to the impedance by  $R(\omega) = R_0$  and  $X(\omega) = X_{-1}/\omega + X_1\omega$ .

Equation (4.16) is valid only when the no-slip condition is satisfied at the acoustic treatment. For the slip condition and also PDC to be satisfied, a time-domain impedance boundary condition similar to Equation (4.16) can be found to be

$$\frac{\partial p}{\partial t} + M \frac{\partial p}{\partial x} = R_0 \frac{\partial v_n}{\partial t} - X_{-1}v_n + X_1 \frac{\partial^2 v_n}{\partial t^2} \quad (4.17)$$

However this boundary condition has been found to be unstable both analytically and by our numerical experiments, a result supporting the analysis in References [49, 52].

The stability analysis in References [49, 52] shows that time-domain impedance boundary conditions are unstable with the combination of PDC and slip condition. This limitation is not unique to the current time-domain formulation in Equation (4.17). It is a challenge to be overcome for any time-domain impedance boundary conditions. However, we may take an alternative approach that leads to the same result by using a stable non-slip time-domain impedance boundary condition and the fact that as the boundary layer thickness approaches to zero, the non-slip impedance boundary condition gives a limiting result of the combination of PDC and slip condition. [29, 52]

#### 4.1.2.3 Hard Wall Boundary Condition

The hard wall boundary condition is applied at the upper wall. A ghost point is introduced right above each of the node at the upper boundary in implementing the condition  $\partial p / \partial y = 0$  at  $y = h$ . The hard wall can also be treated as a special case of the acoustically treated wall with  $R(\omega) = X(\omega) = \infty$ . In such a case, the adoption of either PDC or PVC does not make a difference, i.e., Equations (4.6) and (4.7) are equivalent.

#### 4.1.2.4 Numerical Scheme

The two-dimensional linearized Euler equations are numerically solved with a fourth-order seven-point-stencil optimized upwind Dispersion-Relation-Preserving scheme [68]. The spatial coefficients for both the interior and the boundary points are the same as those listed in Reference [68] while the temporal coefficients are from Reference [47].

### **4.1.3 Comparison with the Analytical Solution**

The semi-infinite impedance duct problem with only the least attenuated mode is used to test the numerical methods presented above. The domain of interest starts at  $x = 0$  and ends at  $x = 0.8382$ , for which we use 216 grid points in the  $x$  direction and 14 grid points in the  $y$  direction with uniform spacings  $\Delta x$  and  $\Delta y$ . The PML boundary conditions with and without incoming waves are implemented in 10 vertical  $x$ -layer left to  $x = 0$  and 20 vertical  $x$ -layers right to  $x = 0.8382$ , respectively. The time step is chosen such that  $CFL = 0.05$  for  $\Delta x$ . The parameters  $X_{-1}$  and  $X_1$  for the reactance  $X$  are selected such that the specific impedance  $Z = 4.99 + 0.25i$  is satisfied

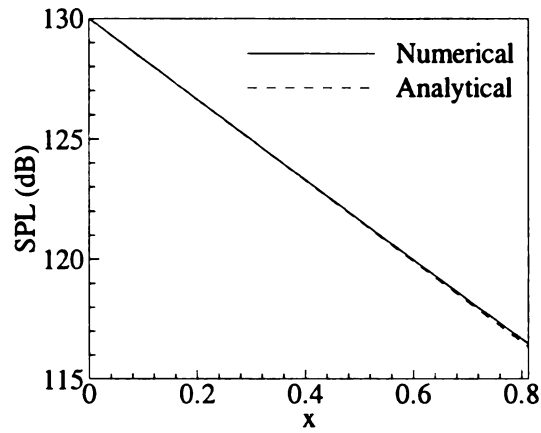
for the test frequency given earlier. We have conducted a grid dependence study, which shows that a converged solution is achieved with the above spatial and temporal resolutions. The calculation is started with all the acoustic variables being zero everywhere in the computational domain and is terminated when the solution has become periodic. It takes about 90 seconds of CPU time and 1.2 MB of memory on a personal computer with an Athlon XP 1800+ CPU at 1533 MHz and 512-MB PC2100 DDR memory.

In Figure 4.2, we compare the numerical solution with the analytical solution for the zero mean flow case. Shown in Figure 4.2 (a) is a comparison on the sound pressure level along the hard wall. It can be seen that the numerical solution coincides with the analytical solution described by a straight line very well even near the exit of the computational domain. Figure 4.2 (b) compares the phase along the hard wall, where the phase is relative to the inlet point on the hard wall and has been converted into the range of  $[-180^\circ, 180^\circ]$ . Again, the agreement between the numerical solution and the analytical solution is excellent everywhere in the computational domain. Specially, the excellent agreements near the exit substantiate that the PML boundary condition indeed introduces little reflections.

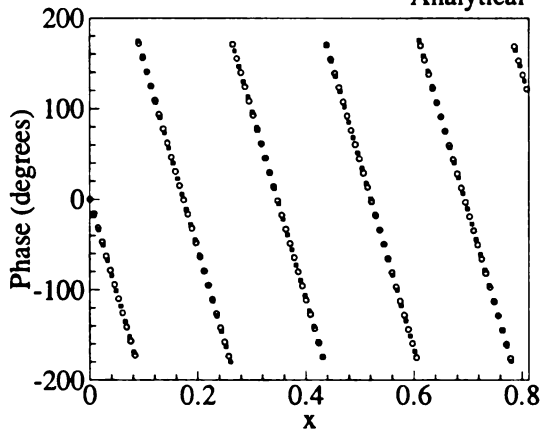
With a sheared mean flow  $M(y) = 1.2(y/h)(1 - y/h)$ , the comparisons between the analytical and the numerical solutions are given in Figure 4.3. As we can see, an excellent agreement between the two solutions is achieved.

By benchmarking our numerical methods with the analytical solution, we conclude that our numerical methods are accurate and reliable under the physical

conditions and configurations in the test problem. In the next section, we are going to apply our numerical methods to the NASA impedance duct configuration.

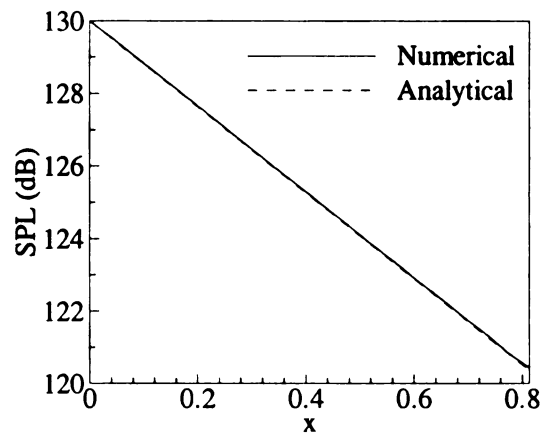


(a)   
 • Numerical   
 ○ Analytical

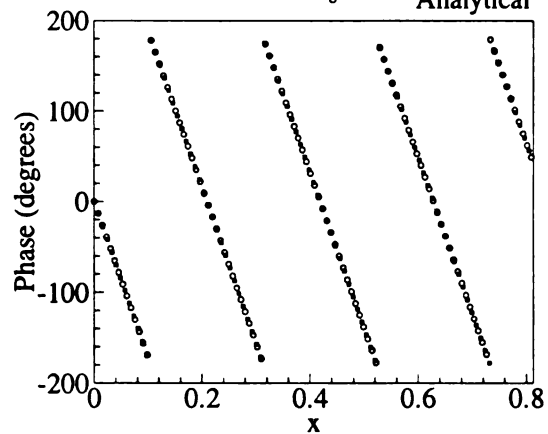


(b)

**Figure 4.2** Comparison of the numerical solution with the analytical solution for the least attenuated mode of the semi-infinite duct problem with a zero mean flow. (a) Sound pressure level along the hard wall; (b) Phase along the hard wall.



(a)   
 • Numerical  
 ○ Analytical



(b)

**Figure 4.3** Comparison of the numerical solution with the analytical solution for the least attenuated mode of the semi-infinite duct problem with a sheared mean flow  $M(y) = 1.2(y/h)(1 - y/h)$ . (a) Sound pressure level along the hard wall; (b) Phase along the hard wall.

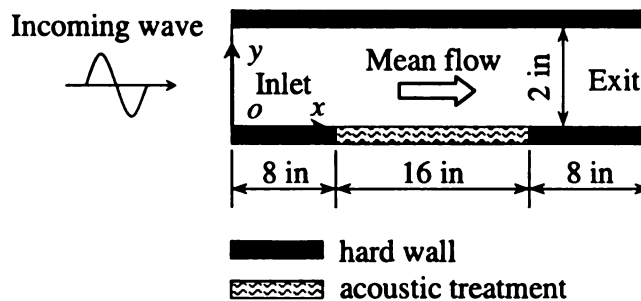


**Figure 4.4** Configuration of the NASA Langley flow-impedance tube

## 4.2 Validation with Experimental Data

### 4.2.1 Experimental Setup

The experimental data from the Flow-Impedance Test Laboratory of NASA Langley Research Center [37] are used to validate our numerical methods. The duct configuration for the experiment is shown in Figure 4.4, where acoustic treatment is applied only in the middle section of the lower wall while all the rest of the walls are hard wall. The liner impedance  $Z_{wall}$  and exit impedance  $Z_{exit}$  were experimentally measured at each test frequency  $f = \omega / 2\pi$  and are listed in Table 4.2. An incoming acoustic wave of each test frequency is supplied at the inlet and its amplitude is adjusted such that the numerical result best matches the experimental data at the duct inlet for each test frequency.

**Table 4.2** Impedance on the wall and at the exit

$f$ (Hz)	$Z_{wall}$		$Z_{exit}$	
	$R$	$X$	$R$	$X$
500	0.41	-1.56	1.077	0.008
1000	0.46	0.03	0.966	0.042
1500	1.08	1.38	0.935	-0.047
2000	4.99	0.25	1.094	-0.070
2500	1.26	-1.53	1.074	0.127
3000	0.69	-0.24	0.852	0.008

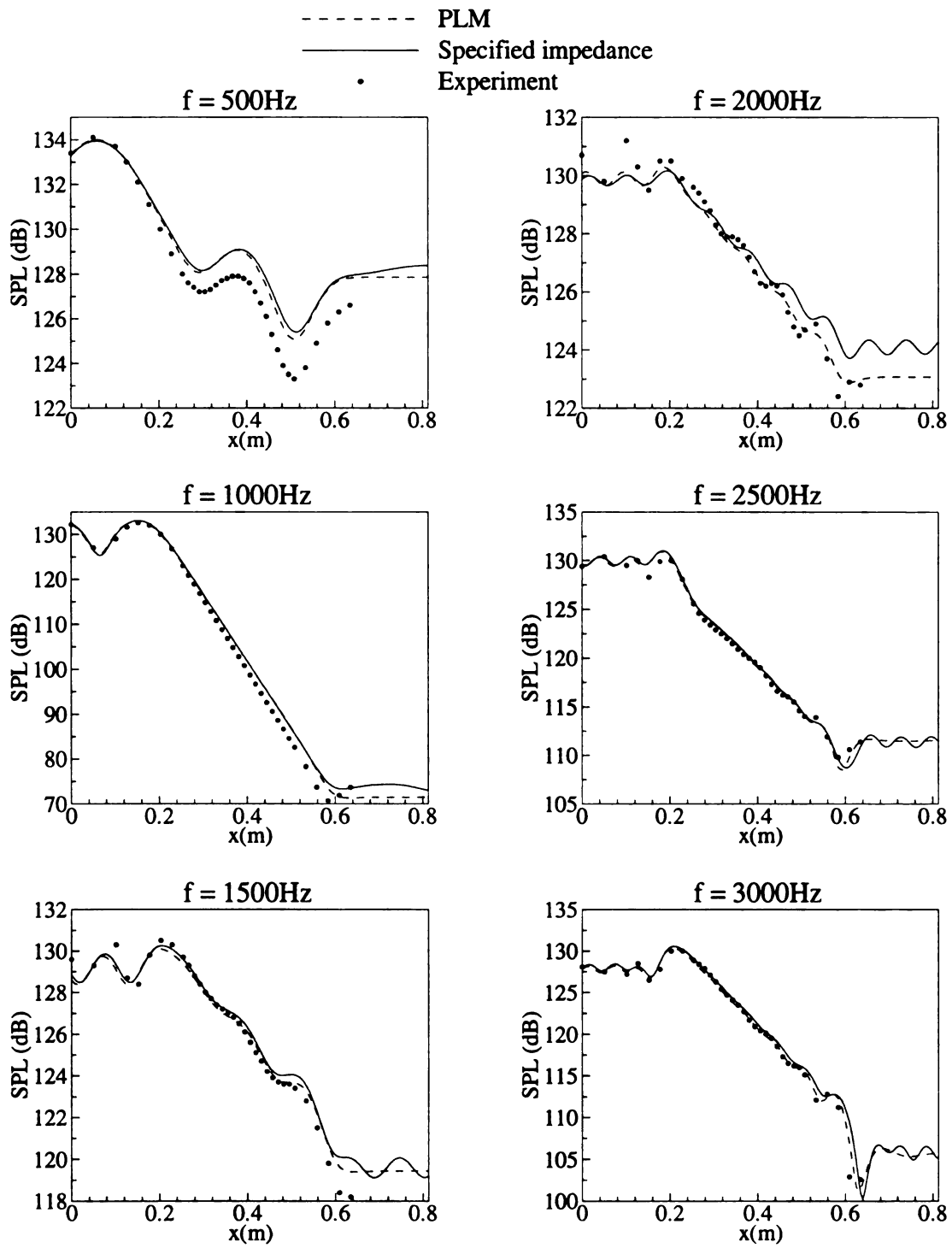
### 4.2.2 Numerical Results and Comparison with the Experimental Data

The NASA Langley flow-impedance tube problem is solved numerically by the numerical methods introduced in section 4.1. For the zero mean flow cases, both the

PML boundary condition and the impedance boundary condition with the specified exit impedance  $Z_{exit}$  are considered for the exit boundary condition. The grid and time step used for both the cases are the same as for the verification problem except that for the latter case, the vertical x-layers right to the domain of interest are not needed, which correspondingly reduces the computational cost. The numerical results of SPL and the phase along the upper hard wall are shown in Figure 4.5 for all the test frequencies, where “PML” and “Specified impedance” denote the boundary conditions used. As we can see, the agreements between the numerical results and the experimental measurements are in general very good. Note that when the PML boundary condition is used at the exit, there is virtually no reflection at the exit. The reflection is apparent when the specified impedance condition is used at the exit. However, due to the fact that the reflection at the exit is small, the difference between the numerical solutions with the two different boundary conditions at the exit is insignificant except for the case of 2000Hz. For this case, there is a small discrepancy between the two numerical results. It is also noted from Figure 4.5 that the agreement between the numerical solution and the experimental data improve as the frequency increases. The reason for the improvement could be that the reflections at both the inlet and the exit are minimum at higher frequencies. Therefore the PML boundary conditions used are more adequate for these cases.

For the cases with a mean flow, only the PML boundary condition is applied at the exit. Since an accurate mean flow profile is not available, we assume the profile as  $M(y) = 1.2(y/h)(1 - y/h)$  for the nominal Mach number 0.3. The same measured impedance parameters for the liner in Table 4.2 are used. The results are compared with

the experimental data in Figure 4.6. Again, the agreement between the numerical solution and the experimental data is very good for both the sound pressure level and the phase.



(a)

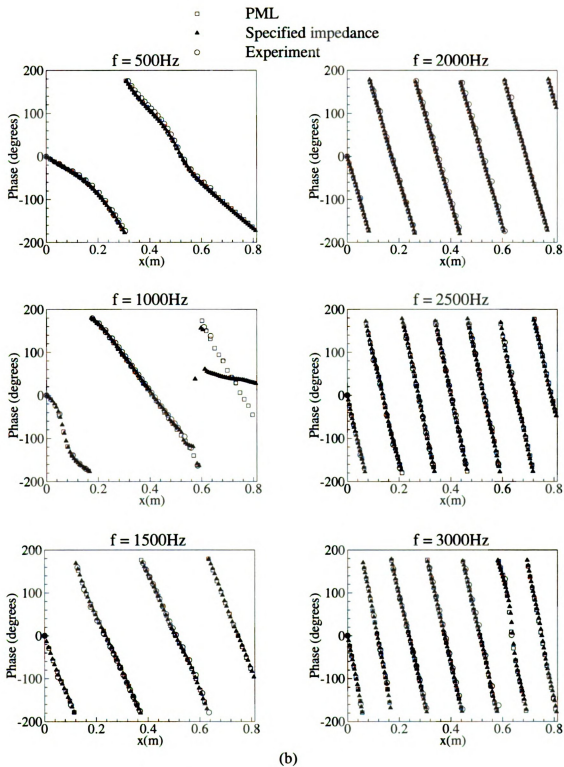
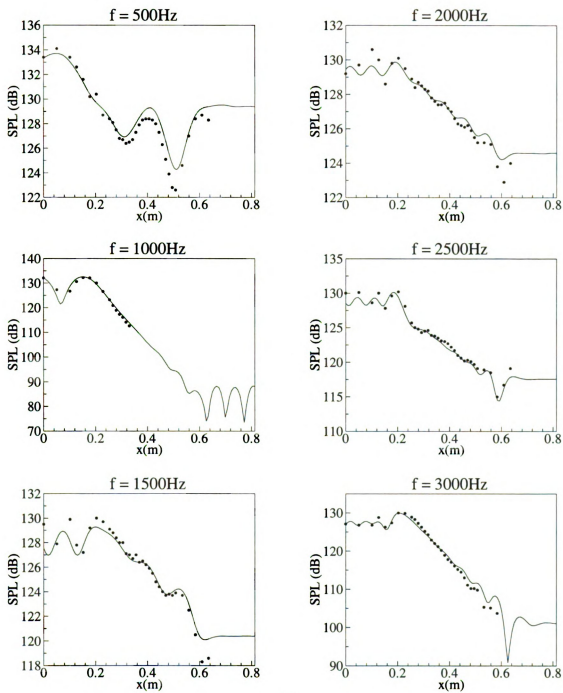


**Figure 4.5** Comparison of the numerical solution with the experimental result at test frequencies with a zero mean flow. (a) SPL along the upper (hard) wall; (b) Phase along the upper (hard) wall.

— Numerical  
• Experiment



(a)

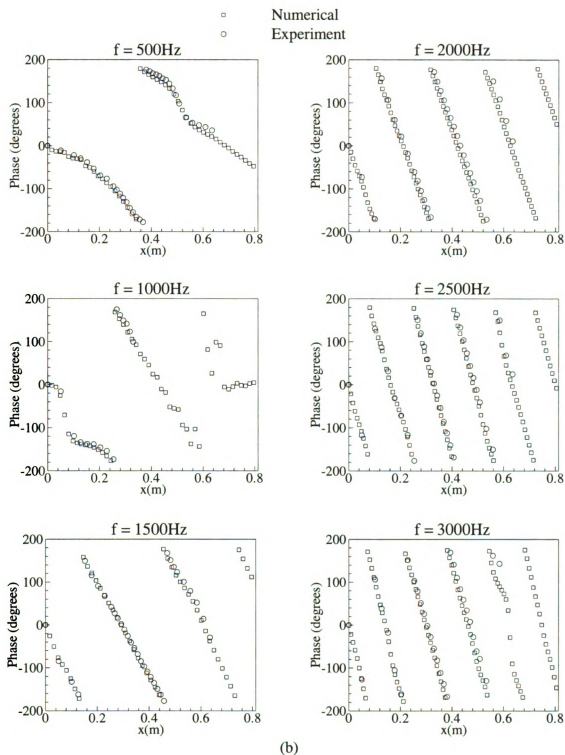


**Figure 4.6** Comparison of the numerical solution with the experimental result at test frequencies with a mean flow profile assumed as  $M(y) = 1.2(y/h)(1 - y/h)$ . (a) SPL along the upper (hard) wall; (b) Phase along the upper (hard) wall.

## 5 A TIME-DOMAIN METHOD FOR ACOUSTIC WAVE SOLUTIONS OF MULTI-FREQUENCY SOUND SOURCES IN SHEARED MEAN FLOWS

Based on the characteristics of the eigen-solution of the homogeneous linearized Euler equations (LEE), a procedure is developed that can separate the instability wave solution contained in the total solution of the LEE from the acoustic solution. The problem formulation and the analytical solution are given in sections 5.1 and 5.2 respectively. In section 5.3, a full description of the numerical methodology and a global time-domain method of separating the instability wave solution from the total solution of the LEE for a multi-frequency sound source are presented. The numerical solutions of the acoustic wave solution are shown in comparison with the respective analytical solutions.

### 5.1 Problem Formulation

The problem studied here is similar to Problem 1 of Category 4 in the Fourth Computational Aeroacoustics Workshop on Benchmark Problems [59] except that the sound source involves multiple frequencies or a broad-banded spectrum instead of a single frequency. This difference renders a frequency-domain method less feasible. The schematic of the problem is shown in Figure 5.1.

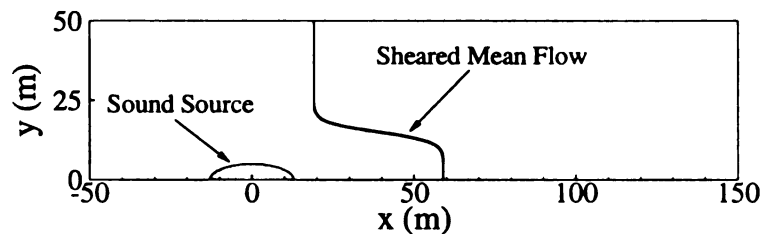


**Figure 5.1** The domain of interest with a sound source and a sheared mean flow

The problem is symmetric about the  $x$ -axis and the domain of interest is given as  $-50\text{m} \leq x \leq 150\text{m}$  and  $0\text{m} \leq y \leq 50\text{m}$ . A sound source is located near  $x = 0$  m and  $y = 0\text{m}$ . The mean flow is parallel to the  $x$ -axis and the mean flow velocity, density and pressure are given by

$$\begin{cases} \bar{u}(y) = u_j \exp[-(\ln 2)(y/b)^2] \\ \bar{v} = 0 \\ \frac{1}{\bar{\rho}(y)} = -\frac{1}{2} \frac{\gamma - 1}{\gamma \bar{p}} [\bar{u}(y) - u_j] \bar{u}(y) + \frac{1}{\rho_j} \frac{\bar{u}(y)}{u_j} + \frac{1}{\rho_\infty} \frac{u_j - \bar{u}(y)}{u_j} \\ \bar{p} = 103330 \text{ Pa} \end{cases} \quad (5.1)$$

where the mean flow parameters are given in Table 5.1, with  $M_j = u_j / \sqrt{\gamma R T_j}$ .

**Table 5.1** The mean flow parameters

$M_j$	$T_j$ (K)	$T_\infty$ (K)	$R$ ( $\text{m}^2\text{s}^{-2}\text{K}^{-1}$ )	$\gamma$	$b$ (m)
0.756	600	300	287.0	1.4	1.3

The governing equations are the two-dimensional LEE for a parallel mean flow in the  $x$  direction,

$$\left( \frac{\partial}{\partial t} + A \frac{\partial}{\partial x} + B \frac{\partial}{\partial y} \right) \mathbf{U} + D \frac{\partial \bar{\mathbf{U}}}{\partial y} = \mathbf{S} \quad (5.2)$$

where

$$\mathbf{U} = \begin{bmatrix} \rho \\ u \\ v \\ p \end{bmatrix}, A = \begin{bmatrix} \bar{u} & \bar{p} & 0 & 0 \\ 0 & \bar{u} & 0 & 1/\bar{p} \\ 0 & 0 & \bar{u} & 0 \\ 0 & \gamma \bar{p} & 0 & \bar{u} \end{bmatrix}, B = \begin{bmatrix} 0 & 0 & \bar{p} & 0 \\ 0 & 0 & 0 & 0 \\ 0 & 0 & 0 & 1/\bar{p} \\ 0 & 0 & \gamma \bar{p} & 0 \end{bmatrix}, \bar{\mathbf{U}} = \begin{bmatrix} \bar{\rho} \\ \bar{u} \\ \bar{v} \\ \bar{p} \end{bmatrix},$$

$$D = \begin{bmatrix} v & 0 & 0 & 0 \\ 0 & v & 0 & 0 \\ 0 & 0 & 0 & 0 \\ 0 & 0 & 0 & 0 \end{bmatrix}, \text{ and } \mathbf{S} = \begin{bmatrix} 0 \\ 0 \\ 0 \\ S(x, y, t) \end{bmatrix}.$$

The non-homogeneous term  $S(x, y, t)$  on the right hand side of Equation (5.2) represents the sound source. Due to the facts that all numerical schemes have a limitation on dealing with high-frequency acoustic waves and the high-frequency acoustic waves can be effectively damped out in the atmosphere, the high-frequency components in a sound source can be safely neglected in this study. As a result, a sound source composed of either discrete frequencies or a broadband spectrum can be effectively represented by a finite number of frequencies. For the purpose of demonstration, it is assumed that the sound source in the current problem consists of three frequency components, denoted by  $l = 1, 2, 3$ , each with its own amplitude  $a_l$ , spatial dependence, and phase  $\varphi_l$ , i.e.,

$$S(x, y, t) = \sum_{l=1}^3 a_l \exp[-(b_{x,l}x^2 + b_{y,l}y^2)] \exp[-i(\omega_l t + \varphi_l)]$$

where the sound source parameters are given in Table 5.2.

**Table 5.2** The sound source parameters for the three-frequency-component sound source

$l$	$a_l$ ( $\text{m}^{-1}\text{Kg s}^{-3}$ )	$b_{x,l}$ ( $\text{m}^{-2}$ )	$b_{y,l}$ ( $\text{m}^{-2}$ )	$\omega_l$ ( $\text{rad s}^{-1}$ )	$\varphi_l$
1	1E3	0.04 ln 2	0.32 ln 2	76	0
2	1E4	0.04 ln 2	0.32 ln 2	38	$\pi/3$
3	1E3	0.04 ln 2	0.32 ln 2	60	0

As will be seen in the next section, the sound source at the three excitation frequencies  $\omega_l$ ,  $l = 1, 2, 3$  will trigger, for each frequency, an instability wave that grows along the  $x$  direction and co-exists with the acoustic waves radiated from the sound source. Such instability waves can overwhelm the acoustic waves downstream of the sound source. Therefore it is necessary to either eliminate or isolate these instability waves so that the acoustic wave solution can be achieved alone.

## 5.2 Instability Wave and Analytical Solution

### 5.2.1 Instability Wave

Assuming that the perturbations of flow variables have a space- and time-dependence of the following form

$$\begin{bmatrix} \rho \\ u \\ v \\ p \end{bmatrix} = \begin{bmatrix} \Phi(y) \\ U(y) \\ V(y) \\ P(y) \end{bmatrix} \exp[i(\alpha x - \omega t)] \quad (5.3)$$

where  $\alpha$  is the wavenumber in the  $x$  direction, the homogeneous version of Equation (5.2) can be reduced to a second order ordinary differential equation for  $P(y)$

$$\frac{d}{dy} \left( \frac{1}{\bar{\rho}(\omega - \alpha \bar{u})^2} \frac{dP}{dy} \right) + \left( \frac{1}{\gamma \bar{p}} - \frac{\alpha^2}{\bar{\rho}(\omega - \alpha \bar{u})^2} \right) P = 0 \quad (5.4)$$

The boundary condition at  $y = 0$  is given by the symmetry condition

$$\frac{dP}{dy} = 0 \quad (5.5)$$

In the far field, where the mean flow is uniform, the solution to Equation (5.4) must be in a form of  $C \exp(i\beta y)$ , where  $C$  is an arbitrary constant, and

$\beta = \sqrt{(\omega/a_\infty)^2 - \alpha^2}$  with  $a_\infty$  being the sound speed in the far field. Note that a positive sign has been chosen for  $\beta$  such that the wave is outgoing at  $y \rightarrow \infty$ . The boundary condition at  $y \rightarrow \infty$  is therefore

$$\frac{dP}{dy} = i\beta P \quad (5.6)$$

Equation (5.4) with the boundary conditions (5.5) and (5.6) forms an eigenvalue problem and is numerically solved using the shooting method. At the three excitation frequencies of the sound source given in section 5.1,  $\omega = 38, 60$  and  $76$  rad/s, the corresponding characteristic wavenumbers are  $\alpha = 0.1547 - 0.0384i$ ,  $0.2980 - 0.0576i$ , and  $0.4145 - 0.0377i$  m<sup>-1</sup>. The imaginary parts of these wavenumbers are negative and thus indicate a wave growing in the  $x$  direction for each of the three frequencies, according to the form assumed in Equation (5.3).

The above analysis shows that the instability wave is intrinsic to the homogenous LEE under the mean flow and boundary conditions given in section 5.1. It, therefore, exists for any corresponding non-homogeneous LEE with the same mean flow and boundary conditions. The non-homogenous term in LEE acts both as a sound source radiating acoustic waves to the surroundings and as a trigger for the instability wave.

### 5.2.2 Analytical Solution to the Acoustic Wave

Dahl [6] has derived the analytical solution for a problem very similar to the one formulated in section 5.1. The sound pressure of the acoustic wave solution for the current problem can be obtained for each frequency in Table 5.2 as

$$\begin{aligned}
p_a(x, y, t) = & -\frac{ia}{2\pi\bar{p}} \sqrt{\frac{\pi}{b_x}} \exp[-i(\omega t + \varphi)] \\
& * \int_{-\infty}^{\infty} \exp(ikx - k^2 / 4b_x) \left[ \zeta_1(k, y) \int_y^{\infty} \frac{\bar{\rho}(y_0)(\omega - \bar{u}(y_0)k)}{\Delta(k, y_0)} \exp(-b_y y_0^2) \zeta_2(k, y_0) dy_0 \right. \\
& \left. + \zeta_2(k, y) \int_0^y \frac{\bar{\rho}(y_0)(\omega - \bar{u}(y_0)k)}{\Delta(k, y_0)} \exp(-b_y y_0^2) \zeta_1(k, y_0) dy_0 \right] dk
\end{aligned} \quad (5.7)$$

where  $\zeta_1(k, y)$  ( $\zeta_2(k, y)$ ) is the solution to the initial-value problem of the characteristic Equation (5.4) only with the boundary condition at  $y = 0$  ( $y = \infty$ ) for a given wavenumber  $k$ ;  $\Delta(k, y)$  is the Wronskian of  $\zeta_1(k, y)$  and  $\zeta_2(k, y)$  with respect to  $y$ , defined as

$$\Delta(k, y) = \zeta_1(k, y) \frac{\partial \zeta_2(k, y)}{\partial y} - \zeta_2(k, y) \frac{\partial \zeta_1(k, y)}{\partial y} \quad (5.8)$$

Note that  $\zeta_1(k, y)$  and  $\zeta_2(k, y)$ , as well as their Wronskian, are not analytically obtainable for a general parallel mean flow condition. They, along with the integrals in Equation (5.7) are numerically evaluated. For a multiple frequency components sound source, the solution is the superposition of the solutions of each frequency component. The obtained sound pressure of the acoustic wave solution  $p_a(x, y, t)$ , referred to as the analytical solution, will be used in the next section for comparisons with the numerical solution.

### 5.3 Numerical Solution

The total solution of the problem proposed in section 5.1 contains both the acoustic wave solution and the instability wave solution. If the instability wave solution contained in the total solution is known, which is referred to as the contained instability wave solution, then the acoustic wave solution can be achieved by subtracting the contained instability wave solution from the total solution. This section is organized as follows: first the numerical method used for obtaining the total solution and the technique

of how to numerically achieve the “pure” instability solution are explained. Then a method is demonstrated that can derive the contained instability wave solution and thus the acoustic wave solution from the pure instability wave solution and the total solution. At last the numerical results of the acoustic wave solution are compared with the respective analytical solutions.

### 5.3.1 Numerical solutions of the Total Solution and the Pure Instability Wave Solution

Shown in Figure 5.2 is the computational domain with  $-250 \text{ m} \leq x \leq 350 \text{ m}$  and  $0 \text{ m} \leq y \leq 100 \text{ m}$ . In the  $x$ -direction, a uniform grid with  $\Delta x = 1.5 \text{ m}$  is used and in the  $y$  direction, the grid size varies from  $\Delta y = 0.4 \text{ m}$  at  $y = 0 \text{ m}$  to  $\Delta y = 1 \text{ m}$  in the far field, with the grid density determined by

$$\left( \frac{dy}{d\xi} \right)_j = 1 - 0.6 \exp[-(\ln 2)y_j^2 / 50]$$

where  $\xi$  is the transformed coordinate of  $y$  and  $j$  is the index of the grid points in the  $y$  direction. In the shaded area ( $-150 \text{ m} \leq x \leq 150 \text{ m}$  and  $0 \text{ m} \leq y \leq 50.62 \text{ m}$ ), the governing equations are applied. In the left, right and upper boundary regions, as denoted by the unshaded area in Figure 5.2, the Perfectly-Matched-Layer (PML) boundary condition in unsplit physical variables [16] is used. At the outer boundaries of the PML regions, a characteristics-based boundary condition is applied to terminate the computational domain. At the lower boundary of the computational domain, a symmetry boundary condition is applied. The numerical scheme used here is a fourth-order seven-point-stencil optimized upwind Dispersion-Relation-Preserving scheme [68]. The size of the time step is  $T_1 / 4000$ , where  $T_1$  is the period corresponding to the first angular

frequency in Table 5.2. An enough number of time steps must be allowed for any initial effects to taper off.

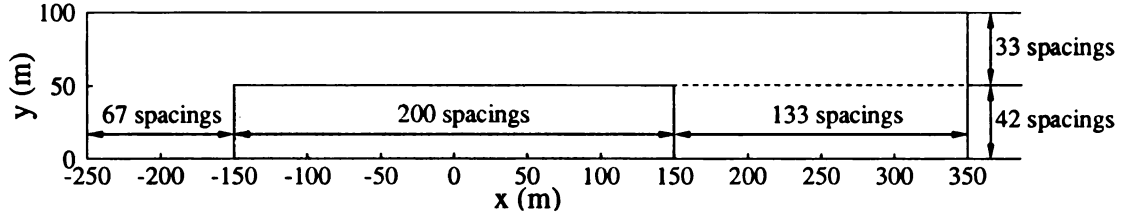


**Figure 5.2** The computational domain with the grid distribution. The unshaded area is the PML regions.

Using the above numerical scheme, the boundary conditions and the grids, the numerical solution of the problem formulated in section 5.1 is obtained. The sound pressure of the solution at  $t = 224T_1$  is shown in Figure 5.3 (a) for the three-frequency component sound source shown in Table 5.2. As expected, the solution contains both the acoustic wave solution and the instability wave solution and thus is referred to as the total solution.

In order to get the “pure” instability wave solution (referred to as the pure instability wave solution), a sound source of the same excitation frequencies is effectively placed upstream of the domain of interest. Such a sound source will produce a strong instability wave but a weak acoustic wave in the domain of interest and thus the total solution in this region can well approximate a pure instability wave. The sound source actually used for calculating the pure instability wave is

$$S(x, y, t) = [\delta(x - x_1)\delta(y - y_1) - \delta(x - x_2)\delta(y - y_2)] \sum_{l=1}^3 \exp(-i\omega_l t) \quad (5.9)$$

where  $\delta(\cdot)$  the Dirac delta function,  $(x_1, y_1) = (-148.5\text{m}, 0\text{m})$  and  $(x_2, y_2) = (-147\text{m}, 0\text{m})$  are two neighboring grid point on the  $x$ -axis,  $\omega_l$  is the same

angular frequencies in Table 5.2. The reason for choosing such a dipole-like source as in Equation (5.9) is that it produces an acoustic wave that seems to be local to the source and thus weak in the domain of interest. The instability wave solution is then obtained in the same way as the total solution above, but with the sound source replaced by Equation (5.9). The sound pressure of the pure instability wave solution, at the same time as that given in Figure 5.3 (a), is shown in Figure 5.3 (b). It can be seen that inside the domain of interest, which is confined by the short-dashed line, the solution is almost utterly free of acoustic waves radiated from the dipole-like sound source and thus can very closely approximate the pure instability wave. Note that the contours in Figure 5.3 (a) and Figure 5.3 (b) are not on the same scale. Although the pure instability wave and the contained instability wave in the total solution look very similar, they differ both in the phase and in the amplitude for each of the frequencies. The next sub-section explains how to construct the contained instability wave from the total solution and the pure instability wave solution.

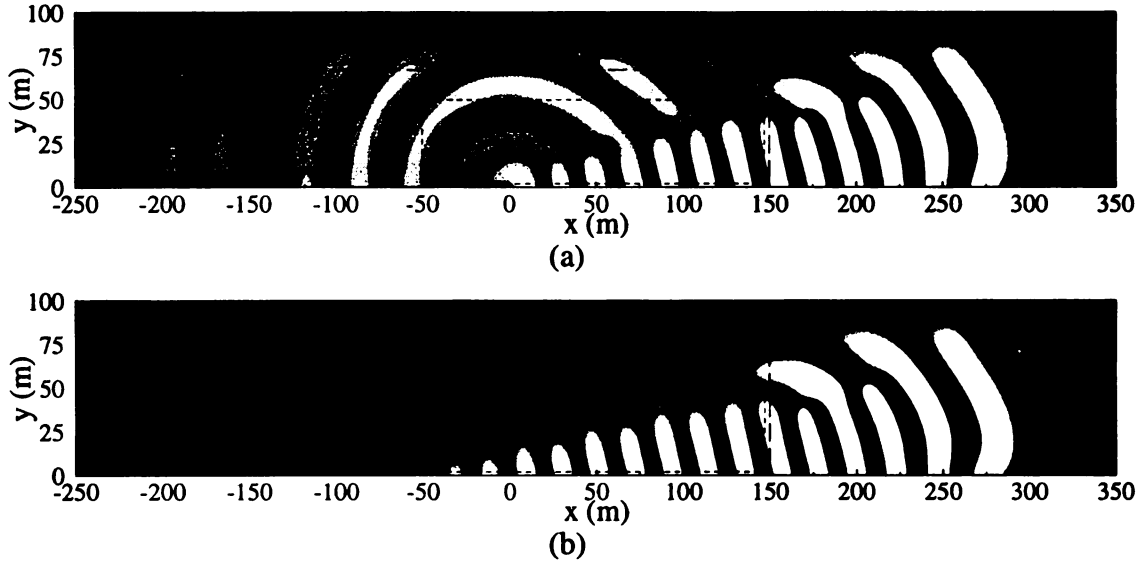


**Figure 5.3** The sound pressure  $t = 224T_1$  in the entire computational domain of  $-250\text{m} \leq x \leq 350\text{m}$  and  $0\text{m} \leq y \leq 100\text{m}$ . Outside the region confined by the long-dashed line is the PML region; the region confined by the short-dashed line is the domain of interest. (a) the total solution; (b) the pure instability wave solution. Note that the contours in the two plots are not on the same scale.

### 5.3.2 Constructing the Contained Instability Wave

As assumed in section 5.1, the spectrum of a sound source is represented by a finite number of angular frequencies  $\omega_l$ ,  $l = 1, 2, \dots, N_\omega$ . The total solution at a reference point  $(x_0, y_0)$ , with a time dependence of  $\exp(-i\omega_l t)$  for each of the angular frequencies  $\omega_l$ , can therefore be written as

$$p(x_0, y_0, t) = \sum_{l=1}^{N_\omega} P_l(x_0, y_0) \exp(-i\omega_l t) \quad (5.10)$$

where  $P_l(x_0, y_0)$  is the complex amplitude for angular frequency  $\omega_l$ . If  $p(x_0, y_0, t)$  represents the actual real-numbered physical quantity, a time history of the numerical solution,  $p(x_0, y_0, t_k)$ ,  $k = 1, 2, \dots, N_t$ , can therefore be expressed as

$$p(x_0, y_0, t_k) = \sum_{l=1}^{N_\omega} [P_{l,r}(x_0, y_0) \cos(\omega_l t_k) + P_{l,i}(x_0, y_0) \sin(\omega_l t_k)], \quad k = 1, 2, \dots, N_t$$

where

$$P_{l,r}(x_0, y_0) + iP_{l,i}(x_0, y_0) = P_l(x_0, y_0), \quad l = 1, 2, \dots, N_\omega$$

Or in the matrix form,

$$[w_{i,j}]_{N_t \times 2N_\omega} \begin{bmatrix} P_{1,r}(x_0, y_0) \\ P_{1,i}(x_0, y_0) \\ \vdots \\ P_{N_\omega,r}(x_0, y_0) \\ P_{N_\omega,i}(x_0, y_0) \end{bmatrix}_{2N_\omega \times 1} = \begin{bmatrix} p(x_0, y_0, t_1) \\ p(x_0, y_0, t_2) \\ \vdots \\ p(x_0, y_0, t_{N_t}) \end{bmatrix}_{N_t \times 1}$$

where

$$[w_{k,l}]_{N_t \times 2N_\omega} = \begin{bmatrix} \cos(\omega_1 t_1) & \sin(\omega_1 t_1) & \cdots & \cos(\omega_{N_\omega} t_1) & \sin(\omega_{N_\omega} t_1) \\ \vdots & \vdots & \vdots & \vdots & \vdots \\ \cos(\omega_1 t_{N_t}) & \sin(\omega_1 t_{N_t}) & \cdots & \cos(\omega_{N_\omega} t_{N_t}) & \sin(\omega_{N_\omega} t_{N_t}) \end{bmatrix}_{N_t \times 2N_\omega}$$

If the matrix  $[w_{k,l}]_{N_t \times 2N_\omega}$  has a rank of  $2N_\omega$ , and  $2N_\omega \leq N_t$  the complex amplitudes are (over-)determined and have the unique least squares solution from the above linear system

$$\begin{bmatrix} P_{1,r}(x_0, y_0) \\ P_{1,i}(x_0, y_0) \\ \vdots \\ P_{N_\omega,r}(x_0, y_0) \\ P_{N_\omega,i}(x_0, y_0) \end{bmatrix}_{2N_\omega \times 1} = [c_{k,l}]_{2N_\omega \times N_t} \begin{bmatrix} p(x_0, y_0, t_1) \\ p(x_0, y_0, t_2) \\ \vdots \\ p(x_0, y_0, t_{N_t}) \end{bmatrix}_{N_t \times 1}$$

where

$$[c_{k,l}]_{2N_\omega \times N_t} = ([w_{k,l}]^T [w_{k,l}])^{-1} [w_{k,l}]^T$$

When the solution is re-written in a component form,

$$P_{l,r}(x_0, y_0) = \sum_{k=1}^{N_t} c_{k,2l-1} p(x_0, y_0, t_k), l = 1, 2, \dots, N_\omega \quad (5.11)$$

$$P_{l,i}(x_0, y_0) = \sum_{k=1}^{N_t} c_{k,2l} p(x_0, y_0, t_k), l = 1, 2, \dots, N_\omega \quad (5.12)$$

Note that the coefficients  $c_{k,l}$  need to be calculated only once. One great feature about Equations (5.11) and (5.12) is that the summation can be carried out at the same time as the values of  $p(x_0, y_0, t_k)$  is being calculated for  $k = 1, 2, \dots, N_t$  and thus there is no need to store the solution history. This feature can help save a considerable amount of memory, in particular when  $N_t$  is large or when the complex amplitudes for many points are needed, as shown later when the complex amplitude of the pure instability wave solution is to be known for the entire domain of interest.

Similarly for the pure instability wave solution,  $p_{ins}(x_0, y_0, t_k)$ , of the same frequency components, the complex amplitude for each frequency is,

$$P_{ins,l}(x_0, y_0) = P_{ins,l,r}(x_0, y_0) + iP_{ins,l,i}(x_0, y_0) , l = 1, 2, \dots, N_\omega$$

with

$$P_{ins,l,r}(x_0, y_0) = \sum_{k=1}^{N_t} c_{k,2l-1} p_{ins}(x_0, y_0, t_k), k = 1, 2, \dots, N_t$$

$$P_{ins,l,i}(x_0, y_0) = \sum_{k=1}^{N_t} c_{k,2l} p_{ins}(x_0, y_0, t_k), k = 1, 2, \dots, N_t$$

Note that the time sequence  $t_k, k = 1, 2, \dots, N_t$ , is not necessarily the same for the total solution and the pure instability wave solution.

Now the reference point  $(x_0, y_0)$  is chosen at a grid point where the contained instability wave in the total solution is very strong while the acoustic wave is very weak. (Such a location is typically far downstream of the sound source.) Then the known total solution can be used to approximate the contained instability wave solution at this point, for each of the frequencies  $\omega_l, l = 1, 2, \dots, N_\omega$ ,

$$P_{c,ins,l}(x_0, y_0) \approx P_l(x_0, y_0)$$

Because an instability wave solution is an eigen-solution of the homogeneous LEE, the contained instability wave solution and the pure instability wave solution at any point  $(x, y)$  differ only by a complex proportionality constant  $C_l$  for each angular frequency  $\omega_l$ . Therefore,

$$C_l = \frac{P_{c,ins,l}(x, y)}{P_{ins,l}(x, y)} = \frac{P_{c,ins,l}(x_0, y_0)}{P_{ins,l}(x_0, y_0)} \approx \frac{P_l(x_0, y_0)}{P_{ins,l}(x_0, y_0)}$$

Since the complex amplitudes,  $P_l(x_0, y_0)$  and  $P_{ins,l}(x_0, y_0)$ , have been calculated from the total solution and the pure instability wave solution respectively, the complex proportionality  $C_l$  is therefore known. As a result the contained instability wave solution at point  $(x, y)$  can be determined by

$$\begin{aligned} p_{c,ins}(x, y, t) &= \text{Re} \left[ \sum_{l=1}^{N_\omega} P_{c,ins,l}(x, y) \exp(-i\omega_l t) \right] = \text{Re} \left[ \sum_{l=1}^{N_\omega} C_l P_{ins,l}(x, y) \exp(-i\omega_l t) \right] \\ &= \sum_{l=1}^{N_\omega} [C_{l,r} P_{ins,l,r} \cos(\omega_l t) + C_{l,r} P_{ins,l,i} \sin(\omega_l t) + C_{l,i} P_{ins,l,r} \sin(\omega_l t) - C_{l,i} P_{ins,l,i} \cos(\omega_l t)] \end{aligned}$$

where the complex amplitude for the pure instability wave,  $P_{ins,l}(x, y)$ , is calculated in the same way as  $P_{ins,l}(x_0, y_0)$ . As can be seen here, the complex amplitude for the pure

instability wave solution is needed for the entire domain of interest.

Finally, the acoustic wave solution is obtained by subtracting the contained instability wave solution from the total solution,

$$p_{acous}(x, y, t) = p(x, y, t) - p_{c,ins}(x, y, t)$$

### 5.3.3 Acoustic Wave Solution in Comparison with the Analytical Solution

Following the procedure described in the last subsection, the acoustic wave solution is calculated by using the point  $(x_0, y_0)$  ( $x_0 = 147\text{m}$ ,  $y_0 = 0\text{ m}$ ) as the reference point and  $N_t = 20$  after any initial effects have tapered off. Figure 5.4 (a), (b) and (c) show the sound pressure field for the total solution, the contained instability wave solution, and the acoustic wave solution, respectively, at the same time as that given in Figure 5.3. The sound source considered here is the three-frequency component sound source given in Table 5.2. The comparisons of the corresponding sound pressure along the lines of  $-50\text{ m} \leq x \leq 150\text{ m}$  at  $y = 15\text{ m}$ ,  $-50\text{ m} \leq x \leq 150\text{ m}$  at  $y = 50\text{ m}$  and  $5\text{ m} \leq y \leq 50\text{ m}$  at  $x = 100\text{ m}$ , with the analytical solutions calculated using the method described in section 5.1 are shown in Figure 5.5. The agreements between the numerical solutions and the analytical solutions are excellent.

The computation was performed on a personal computer with an Athlon XP 1800+ CPU at 1533 MHz and 512-MB DDR memory at 133 MHz. It took about 15 hrs of CPU time and 10 MB of memory to numerically calculate the total solution and the pure instability solution, and construct the contained instability wave solution to obtain the acoustic wave solution. It is worth mentioning that the computational cost reported above does not necessarily characterize the technique of achieving the acoustic wave

solution. The computational cost greatly depends on the specific numerical scheme and boundary conditions used. With the amplifying nature of instability waves, it takes a longer time for the initial effects to taper off and thus a steady state to establish, because this process involves not only the absorption of the initial waves by the non-reflecting boundary conditions but also the amplification of the instability waves triggered by the numerical reflections due to the imperfectness of these boundary conditions. Therefore, it is expected that a steady state solution can be achieved in less time if a more effective non-reflecting boundary condition is used.

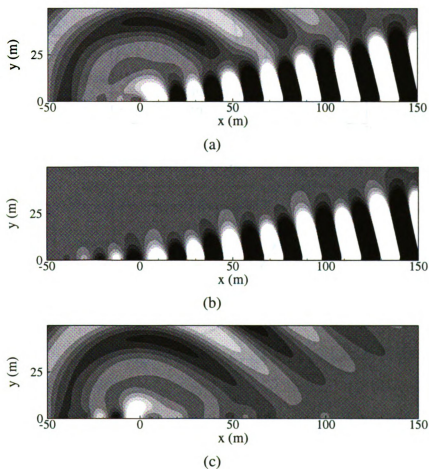
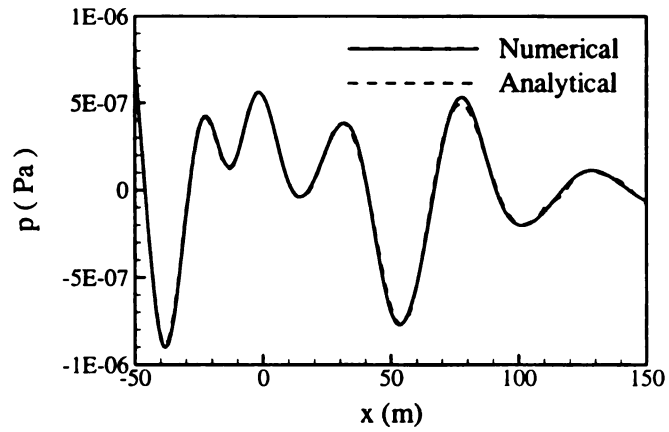
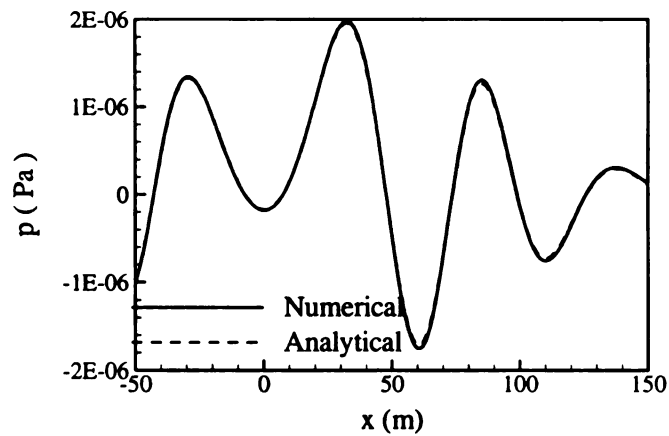


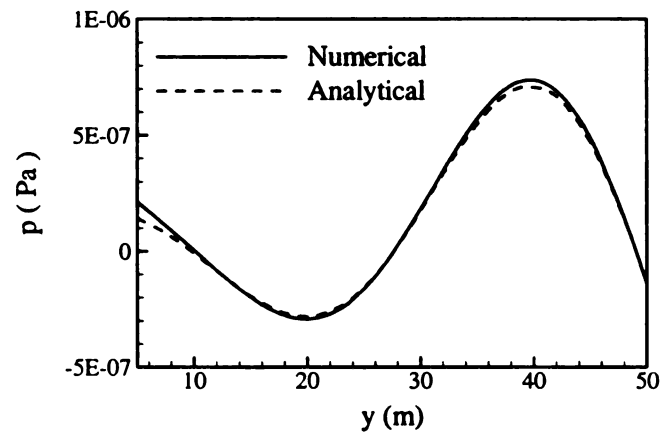
**Figure 5.4** The sound pressure  $t = 224T_1$  in the domain of interest for the three-frequency component sound source. (a) the total solution; (b) the contained instability wave solution; (c) the acoustic wave solution.



(a)



(b)



(c)

**Figure 5.5** The sound pressure for the three-frequency component sound source at  $t = 224T_1$  as compared with the analytical solution along the lines of (a)  $-50 \text{ m} \leq x \leq 150 \text{ m}$  at  $y = 15 \text{ m}$ , (b)  $-50 \text{ m} \leq x \leq 150 \text{ m}$  at  $y = 50 \text{ m}$  and (c)  $5 \text{ m} \leq y \leq 50 \text{ m}$  at  $x = 100 \text{ m}$ .

## 6 COMPUTATIONAL AEROACOUSTICS TIME-DOMAIN METHOD COUPLED WITH ADAPTIVE NOISE CONTROL OPTIMIZER

In this chapter a design of an adaptive noise control system using a computational aeroacoustics (CAA) code combined with an optimizer to adaptively control liner impedance is proposed and tested for multi-dimensional acoustic problems.

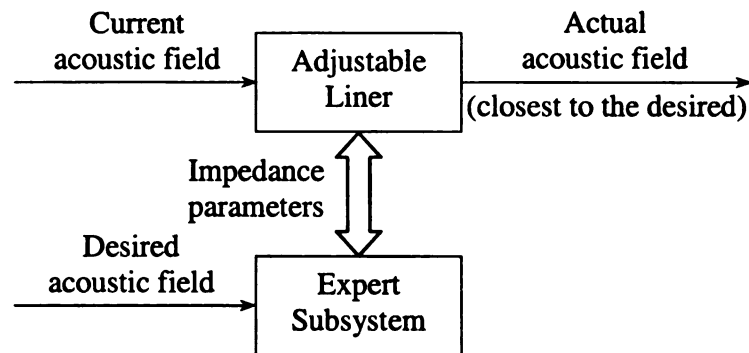


**Figure 6.1** Schematic of the adaptive noise control system

A schematic of this adaptive noise control system is shown in Figure 6.1. The system consists of two primary components, a liner with controllable impedance and an expert subsystem. For a given acoustic noise source and mean flow condition, the current acoustic field refers to the acoustic field resulting from the current values of the liner impedance. The desired acoustic field, which is assumed to be different from the current acoustic field, refers to the acoustic field that we would like to achieve. Considering the desired acoustic field as an input, the expert subsystem calculates new values for the impedance parameters to which the liner is adjusted accordingly to achieve a resultant acoustic field that is the closest to the desired one. This is the basic idea of the adaptive noise control system. In the next section, the expert subsystem and liners with

controllable impedance will be discussed. The implementation of the adaptive noise control system will be demonstrated in section 6.2.

## 6.1 Adaptive Noise Control System

### 6.1.1 The Expert System

Different values of the impedance parameters will have different effects on the acoustic field and thus the resultant acoustic field will be different. In order to achieve an acoustic field that is the closest to the desired one, the expert subsystem is designed to determine the optimum values for those impedance parameters to which the impedance properties are to be adjusted accordingly. For this purpose, the expert subsystem can be treated as an optimization system, whose objective function is one that can indicate the difference between the current and the desired acoustic fields and whose design variables are the impedance parameters. Mathematically, the objective function is formulated as the relative averaged difference in the acoustic pressure of the current and the desired fields over a certain space  $V$  and a certain temporal range  $\Delta t$ , as in Equation (6.1).

$$D = \frac{\int \int |p_{cur} - p_{des}| dV dt}{\int \int |p_{des}| dV dt} \quad (6.1)$$

The acoustic pressure is treated in time domain instead of frequency domain and thus no amplitude, phase and frequency are explicitly associated with it. Therefore the definition in Equation (6.1) indicates a complete comparison between the current and the desired acoustic pressure fields.

A real controllable-impedance substance may only allow its impedance parameters to be varied over specific ranges. This imposes the constraints for the optimization problem.

With the objective function, the design variables and the constraints well defined, the optimization or minimization process is realized with the aid of a MATLAB function 'fmincon', which is provided in the MATLAB optimization toolbox. Details of the algorithms involved in this function can be found in the User's Guide for the optimization toolbox [25] and the references cited in the guide. Only the general ideas are outlined here. The problem under study is formulated as a constrained nonlinear programming problem. Such a problem is solved in MATLAB using the Newton-Lagrange method, with which the problem is first formulated in the form of the Kuhn-Tucker (KT) equations, whose solution forms the basis of the original problem. The KT equations are solved with a Sequential Quadratic Programming (SQP) method, which uses a quasi-Newton method (the Broyden-Fletcher-Goldfarb-Shanno method) to update the Hessian of the Lagrangian function at each major iteration. At each major iteration, a Quadratic Programming (QP) sub-problem for the updated Hessian is first solved to provide a search direction for the current SQP iteration. Then along the search direction, a line search procedure is performed by means of cubic, quadratic or mixed cubic/quadratic polynomial interpolation and extrapolation. The searching result is a new point of design variables that sufficiently decrease the value of a merit function that reflects both the minimization of the objective function and the violation of the constraints.

It is worth mentioning that the optimization process present here is quite similar to the impedance education method of Watson et. al.[55, 56] In their works, the impedance education method is used to find the liner impedance in a duct by minimizing the

difference between the measured acoustic pressure field and the predicted acoustic pressure field, which is numerically calculated by solving the Helmholtz equation (frequency-domain approach) based on the predicted liner impedance. Although their works attack a different practical problem, the idea is essentially the same as that in the expert subsystem of the current chapter. Both deal with an inverse problem, one in time-domain and the other in frequency-domain.

### **6.1.2 Liners with Controllable Impedance**

By now we have established the expert subsystem with which we can approximate a desired acoustic field if we can control the impedance properties. The standard approach of controlling impedance properties is a mechanical approach, which is to control the geometric parameters of the liner (e.g. the diameter and/or depth of the Helmholtz resonators in an array) so that the required impedance properties can be achieved.[2] Since the impedance properties also depend on the liner material properties, a potential approach of controllable impedance might be developed through the control of material properties or micro-structures of the materials. The liners with controllable impedance are critical components in the adaptive noise control system and merit further investigation. However, our main purpose of the current study is to demonstrate the feasibility and potential of the coupling of a CAA time-domain method with an optimizer for the purpose of adaptive noise control, we will not get into any specific approaches for controllable impedance in this chapter. Instead, the three-parameter impedance model of the Helmholtz type [49] given in Equation (6.2) is used for the purpose of the demonstration.

$$Z(\omega) = R_0 - i(X_{-1}/\omega + X_1\omega) \quad (6.2)$$

It is worth mentioning that the general concept of the adaptive noise control system works for all kinds of liners with controllable impedance.

## 6.2 Numerical Implementation and Results

To test the feasibility of the coupling concept above, we implement the concept for a two-dimensional problem as shown in Figure 6.2. All the variables used in this chapter are dimensionless with  $L = 0.012\text{m}$  as the length scale,  $a_0 = 340\text{m/s}$  as the velocity scale,  $\rho_0 = 1.29\text{kg/m}^3$  as the density scale,  $L/a_0$  as the time scale,  $\rho_0 a_0^2$  as the pressure scale and  $\rho_0 a_0$  as the impedance scale.

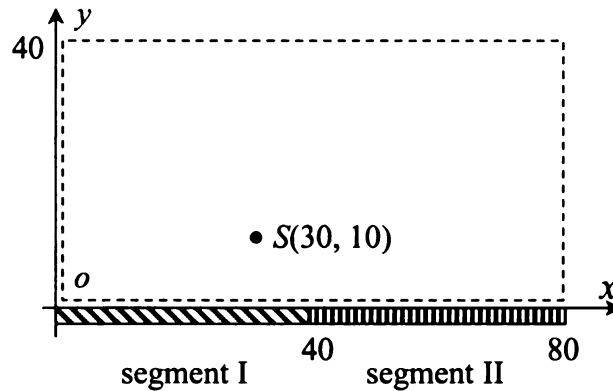


**Figure 6.2** Test problem schematic

The acoustic field of interest lies in the region of  $80 \times 40$  confined in the dashed lines and is bounded by an impedance wall of two segments of equal length, denoted as segments I and II, at  $y = 0$ . The impedance is assumed to be characterized by the three-parameter model as in Equation (6.2) but takes different values for the impedance parameters for the two segments. We add a note that when this model is used for a case with a mean flow, it is assumed that the mean flow effects are included in the three parameters. [49, 61] When the same values are used for the three parameters  $R_0$ ,  $X_{-1}$

and  $X_1$  in the cases of different mean flow conditions, they represent different liners. Initially, the acoustic velocity components are zero everywhere and the broadband acoustic pressure has a cylindrical Gaussian distribution of the form

$$p_0(R) = \exp(-BR^2) \quad (6.3)$$

where  $R$  is the distance to the pulse center  $S$  at  $x = 30$  and  $y = 10$  and  $B = 0.04 \ln 2$ . The above problem is numerically solved by a CAA code in time domain with a seven-point-stencil upwind optimized DRP method. [47, 68] The accuracy is sufficient for both the temporal and spatial scales of the current problem. Nonreflecting radiation boundary condition [48] is applied at the left, right and upper boundaries. It has been substantiated that numerical reflection is virtually zero at these boundaries. At the lower boundary, Tam's broadband time-domain impedance boundary condition [49, 61] is applied. For the three-parameter impedance model in Equation (6.2), the time-domain impedance boundary condition is derived as

$$\frac{\partial p}{\partial t} = R_0 \frac{\partial v_n}{\partial t} - X_{-1} v_n + X_1 \frac{\partial^2 v_n}{\partial t^2} \quad (6.4)$$

where  $p$  and  $v_n$  are the acoustic pressure and the normal acoustic velocity (positive when pointing into the liner) at the impedance wall, both being time-domain variables. The CAA time-domain code will be incorporated in the optimization process to predict the acoustic field given the noise source, the mean flow condition and the values for the impedance parameters.

The optimization process is schematically illustrated in Figure 6.3. As a discretized special case of Equation (6.1), the objective function used in the current optimization process is defined as the sum of the local differences over all the nodes in the computational domain at a certain time, say  $t = 25$ , as in Equation (6.5),

$$D_1 = \frac{\sum_j \sum_i |p_{cur} - p_{des}|_{i,j,t=25}}{\sum_j \sum_i |p_{des}|_{i,j,t=25}} \quad (6.5)$$

where the desired acoustic pressure  $p_{des}$  is assumed to be known and the current acoustic pressure is computed by the CAA time-domain code.

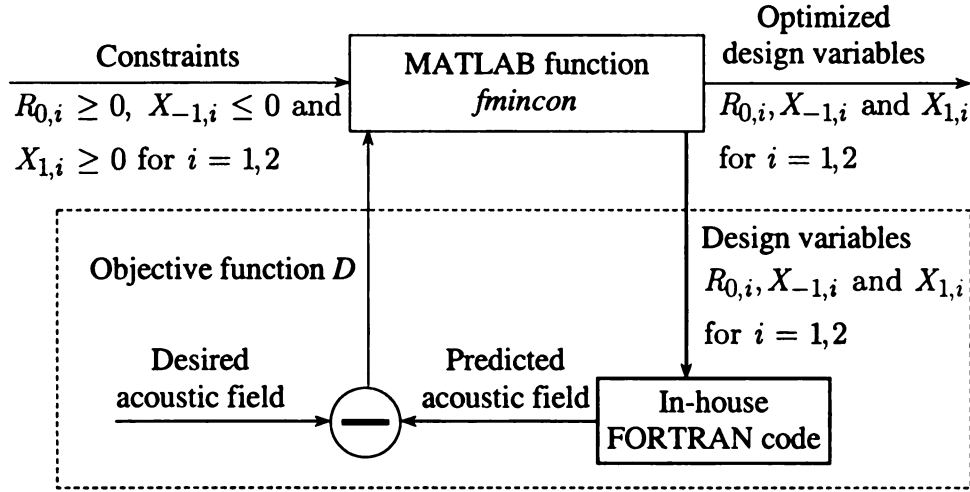


**Figure 6.3** Optimization process

As discussed in section 6.1, constraints may be imposed to the optimization problem from the practical considerations of a real controllable-impedance substance. In the current problem, the three-parameter model in Equation (6.2) is used. Since this model analogously represents a damped mechanical vibration system of resistance  $R_0$ , compliance  $-X_{-1}$  and mass  $X_1$ , all being greater than or equal to zero, we can assume that the physical constraints for the three parameters are  $R_0 \geq 0$ ,  $X_{-1} \leq 0$  and  $X_1 \geq 0$ . Mathematical analysis shows that the constraint  $X_{-1} < 0$  is also required for the stability of the broadband time-domain impedance boundary condition. [49]

The MATLAB function 'fmincon' is used to minimize the objective function that is calculated by an in-house FORTRAN program. Every time upon being called by

'fmincon', the FORTRAN program numerically calculates the acoustic field with the impedance parameters that it receives as inputs using the CAA time-domain code. It then calculates the relative averaged difference between the two fields as defined in Equation (6.5). The difference is returned to 'fmincon' as the value of the objective function. Many calls may be needed before the optimization process is terminated when the magnitude of the directional derivative in the search direction is less than  $2 \times 10^{-9}$  while all the constraints are satisfied. The small magnitude indicates the optimization accuracy.

To test the optimization process, several desired acoustic fields are proposed for three different mean flow conditions: no mean flow, a uniform mean flow ( $M_x = 0.8$ ,  $M_y = 0$ ) and a sheared mean flow ( $M_x(y) = 0.8 \sin[(\pi/2)/(y/40)]$  and  $M_y = 0$ ). For each of the mean flow conditions, the desired acoustic fields for unperturbed and perturbed cases are specified as the following. For the unperturbed cases, the desired acoustic fields are calculated by the CAA code for a given set of impedance parameters shown as 'exact' in Table 6.1. These desired acoustic fields for unperturbed cases are shown in Figure 6.4 (a), Figure 6.5 (a), and Figure 6.6 (a) respectively for the three mean flow conditions. For the perturbed cases, the desired acoustic fields are defined as the addition of the desired acoustic fields of the corresponding unperturbed cases and a uniformly distributed random perturbation within 10% of the local acoustic pressure. These desired acoustic fields for the perturbed cases are shown in Figure 6.4 (b), Figure 6.5 (b), and Figure 6.6 (b). Figure 6.7 (a) shows another desired acoustic pressure field achieved by uniformly decreasing by 10% the local acoustic pressure of the unperturbed desired acoustic field with the sheared mean flow in Figure 6.6 (a). After obtaining the

desired acoustic fields for all the cases, we then reverse the process to find out the required impedance parameters by using the optimization process.

For all the desired acoustic fields, we quite arbitrarily choose  $R_0 = 1$ ,  $X_{-1} = -1$  and  $X_1 = 1$ , only to satisfy the physical constraints, as the initial guess for all the simulated cases. It can be seen from Table 6.1 that the values of the initial guess are enough far away from the optimized impedance parameters. Other initial guesses have also been tried and essentially the same results have been obtained. Therefore, we would like to say that the global optimum is achieved. The optimization was performed on a personal computer with an Athlon XP 1800+ CPU at 1533MHz and 512MB memory. It took about 10 minutes of CPU time for each of all the simulated cases. The optimization results are shown in Table 6.1.

In Table 6.1, “unperturbed optimized” is used for the unperturbed cases and “perturbed optimized” is used for the perturbed cases. For the unperturbed cases, the resultant acoustic pressure fields with these optimized impedance parameters are visually undistinguishable from those shown in Figure 6.4 (a), Figure 6.5 (a), and Figure 6.6 (a), respectively and thus are not presented. The values of the impedance parameters for the unperturbed cases are very accurately reproduced by the optimization procedure. It is shown in Table 6.1 that the objective function, or the relative averaged difference, defined in Equation (6.5) is in the order of  $10^{-7}$  for the three unperturbed cases, as compared to zero, the theoretically obtainable value. The small magnitudes of the relative error substantiate the accuracy of the optimization procedure. For the perturbed cases, the resultant acoustic fields with these optimized impedance parameters are shown in Figure 6.4 (c), Figure 6.5 (c), and Figure 6.6 (c) for the three different mean flow conditions. It

is interesting to note that these acoustic fields (Figure 6.4 (c), Figure 6.5 (c), and Figure 6.6 (c)) still resemble the desired acoustic fields for the unperturbed cases (see Figure 6.4 (a), Figure 6.5 (a), and Figure 6.6 (a)). The resemblances can also be found with a comparison between the corresponding optimized impedance parameters for the perturbed cases (see “perturbed optimized” in Table 6.1) and those impedance parameters (see “exact” in Table 6.1) used to produce the desired acoustic fields for the unperturbed cases. These close resemblances result from the fact that the averaged effects of the random perturbations in the desired acoustic fields for the perturbed cases nearly vanish.

For the desired acoustic pressure field shown in Figure 6.7 (a), however, the averaged effect of the modification will not vanish. As might be expected, the resulting values of the impedance parameters (see “modified optimized” in Table 6.1) are quite different from those (see “exact” in Table 6.1) used to produce the desired acoustic field for the unperturbed case. As a result, the difference is also more obvious between the current acoustic pressure field shown in Figure 6.7 (b) and the unperturbed (unmodified) desired one shown in Figure 6.6 (a).

For the perturbed or modified cases, an acoustic field that is identical to the desired one is even physically impossible and thus it is reasonable that the minimized objective function is not as small as for the unperturbed cases. However it is believed that the accuracy is good due to the small magnitude in the directional derivative and the evidence shown for the unperturbed cases.

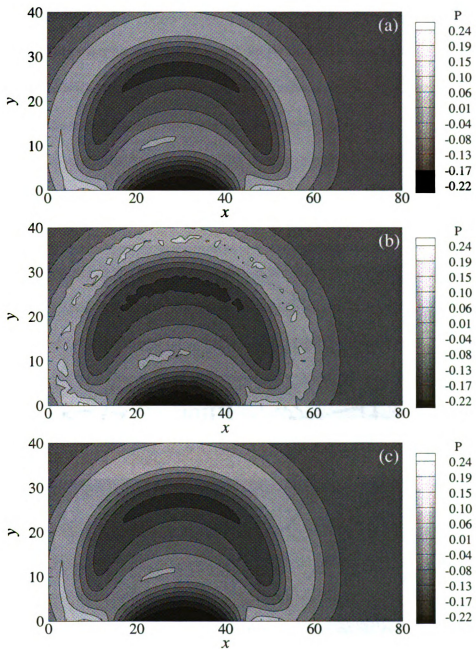


**Figure 6.4** Acoustic pressure fields at  $t = 25$  without mean flow. (a) the unperturbed desired; (b) the perturbed desired; (c) the optimized (resultant) for the perturbed desired.

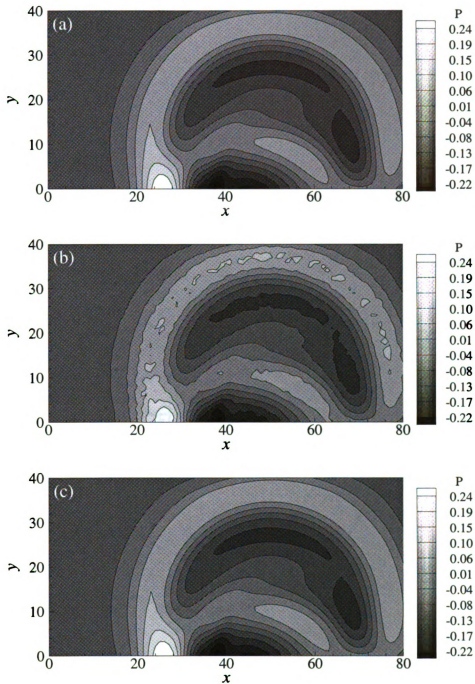


**Figure 6.5** Acoustic pressure fields at  $t = 25$  with a uniform mean flow of  $M_x = 0.8$  and  $M_y = 0$ . (a) the unperturbed desired; (b) the perturbed desired; (c) the optimized (resultant) for the perturbed desired.

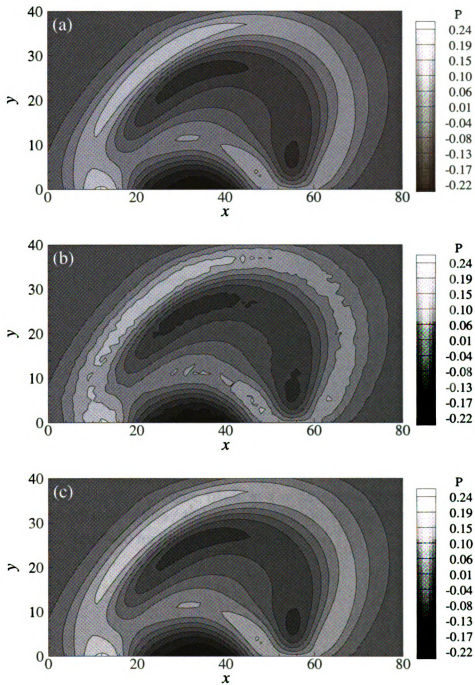


**Figure 6.6** Acoustic pressure fields at  $t = 25$  with a sheared mean flow of  $M_x(y) = 0.8 \sin[(\pi/2)(y/40)]$  and  $M_y = 0$ . (a) the unperturbed desired; (b) the perturbed desired; (c) the optimized (resultant) for the perturbed desired.

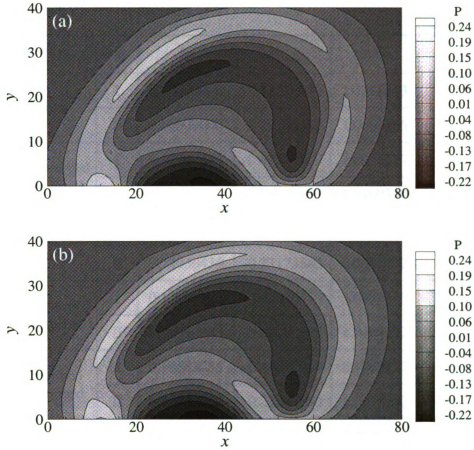


**Figure 6.7** Acoustic pressure fields at  $t = 25$  with a sheared mean flow of  $M_x(y) = 0.8 \sin[(\pi/2)(y/40)]$  and  $M_y = 0$ . (a) the modified desired; (b) the optimized (resultant) for the modified desired.

**Table 6.1** Values for the impedance parameters

		seg.	$R_0$	$X_{-1}$	$X_1$	$D$
all cases	exact	I	0.20000000	-0.47576471	2.09383333	
		II	0.10000000	-0.23788235	1.04691667	
no mean flow	unperturbed optimized	I	0.19999880	-0.47576529	2.09383775	6.01E-07
		II	0.09999081	-0.23788437	1.04693702	
	perturbed optimized	I	0.19766536	-0.47855838	2.11890414	5.00E-02
		II	0.12036436	-0.23173582	0.98874926	
uniform mean flow	unperturbed optimized	I	0.19999997	-0.47576475	2.09383192	5.18E-07
		II	0.09999943	-0.23788338	1.04692421	
	perturbed optimized	I	0.19583255	-0.47632917	2.10251175	5.08E-02
		II	0.10042433	-0.23866052	1.04792525	
sheared mean flow	unperturbed optimized	I	0.19999945	-0.47576487	2.09383427	2.42E-07
		II	0.09999810	-0.23788297	1.04692207	
	perturbed optimized	I	0.20011584	-0.47660989	2.09708747	5.04E-02
		II	0.09269976	-0.24189526	1.07151848	
	modified optimized	I	0.30733303	-0.46104729	2.04534607	8.96E-02
		II	0.16058164	-0.22220306	0.93715973	

## 7 NOISE PREDICTION AND OPTIMIZATION SYSTEM FOR TURBOFAN ENGINE INLET DUCT DESIGN

A noise prediction and optimization system for turbofan inlet duct designs is developed in this chapter. In section 7.1, the numerical noise prediction system including the numerical methods and models are explained in details. Four verification problems are given in section 7.2, each with an emphasis on testing an aspect of the numerical methods. Sections 7.3, 7.4 and 7.5 each present an optimization problem solved with the noise prediction and optimization system.

### 7.1 Noise Prediction System

A schematic of the generic engine inlet duct is shown in Figure 7.1. The duct geometry as well as the mean flow is axisymmetric. The duct wall is partially lined with acoustic liners. With a given sound source at the duct outlet, the sound wave propagates inside the duct and then radiates into the far field. A hybrid method is adopted to solve for the whole computational domain. That is, the governing equations with proper boundary conditions are solved inside the duct and also possibly in its near field and a Kirchhoff method is applied in the far field. These two regions are connected with the Kirchhoff surface as shown in Figure 7.1 . Unless otherwise stated, variables used in this chapter are dimensionless with  $L_0 = 1\text{ m}$  as the length scale,  $c_0 = 340\text{ m/s}$  as the velocity scale,  $\rho_0 = 1.29\text{ kg/m}^3$  as the density scale,  $L_0/c_0$  as the time scale,  $\rho_0 c_0^2$  as the pressure scale and  $\rho_0 c_0$  as the impedance scale. The harmonic time dependence is assumed in the form of  $\exp(i\omega t)$ . Under this convention, the impedance is  $Z = R + iX$ , where  $R$  and  $X$  are the resistance and the reactance.

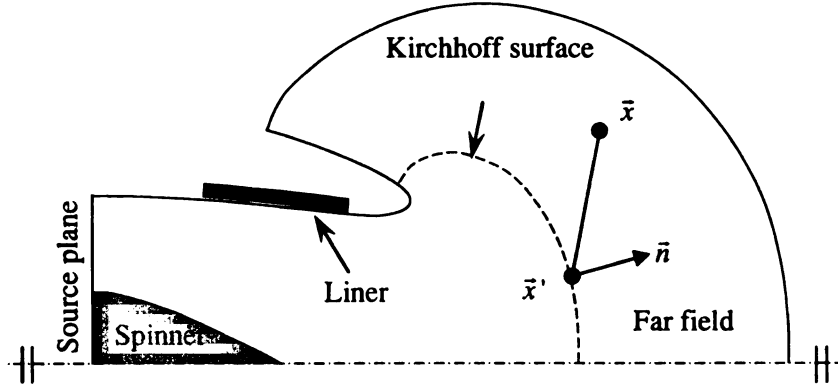


**Figure 7.1** The whole computational domain

### 7.1.1 Governing Equations

Under the assumptions that both the duct geometry and the mean flow are axisymmetric, a spinning mode with azimuthal mode number  $m$  ( $m$  being integers) exists at the angular frequency  $\omega$ . Its perturbation variables in the cylindrical coordinates can thus be assumed of the form,

$$\begin{bmatrix} u(x, r, \theta, t) \\ v(x, r, \theta, t) \\ w(x, r, \theta, t) \\ p(x, r, \theta, t) \end{bmatrix} = \begin{bmatrix} \hat{u}(x, r) \\ \hat{v}(x, r) \\ \hat{w}(x, r) \\ \hat{p}(x, r) \end{bmatrix} \exp(i\omega t + im\theta) \quad (7.1)$$

where  $u$ ,  $v$  and  $w$  are the acoustic velocities in the axial ( $x$ -), radial ( $r$ -) and azimuthal ( $\theta$ -) directions, respectively, and  $p$  is the acoustic pressure. The duct axis is on the  $x$ -axis.

With the form in Equation (7.1), the linearized Euler equations are reduced to

$$\mathbf{A} \frac{\partial \hat{\mathbf{u}}}{\partial x} + \mathbf{B} \frac{\partial \hat{\mathbf{u}}}{\partial r} + \mathbf{C} \hat{\mathbf{u}} + i\omega \hat{\mathbf{u}} = \mathbf{0} \quad (7.2)$$

where

$$\hat{\mathbf{u}} = \begin{bmatrix} \hat{u} \\ \hat{v} \\ \hat{w} \\ \hat{p} \end{bmatrix}, \mathbf{A} = \begin{bmatrix} \bar{u} & 0 & 0 & 1 \\ 0 & \bar{u} & 0 & 0 \\ 0 & 0 & \bar{u} & 0 \\ 1 & 0 & 0 & \bar{u} \end{bmatrix}, \mathbf{B} = \begin{bmatrix} \bar{v} & 0 & 0 & 0 \\ 0 & \bar{v} & 0 & 1 \\ 0 & 0 & \bar{v} & 0 \\ 0 & 1 & 0 & \bar{v} \end{bmatrix}, \text{ and}$$

$$\mathbf{C} = \begin{bmatrix} d\bar{u}/dx & d\bar{u}/dr & 0 & 0 \\ d\bar{v}/dx & d\bar{v}/dr & 0 & 0 \\ 0 & 0 & \bar{v}/r & im/r \\ 0 & 1/r & im/r & d\bar{u}/dx + d\bar{v}/dr + \bar{v}/r \end{bmatrix},$$

and  $\bar{u}$  and  $\bar{v}$  are the mean flow velocities in the axial and radial directions, respectively.

The azimuthal mean flow velocity is zero since the mean flow is axisymmetric.

### 7.1.2 Boundary Conditions

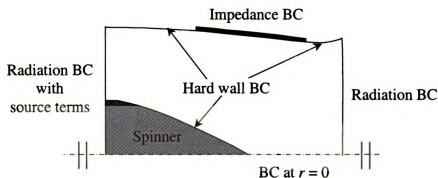


**Figure 7.2** Types of boundary conditions

The computational domain where the governing equations are calculated, i.e., the region inside the duct and the near field, are bounded by boundaries of different characteristics. These boundaries are mathematically modeled by different types of boundary conditions (BC) shown in Figure 7.2, which are explained as follows.

### 7.1.2.1 Boundary Conditions at $r = 0$

Along the axis  $r = 0$ , some terms in the governing equations are singular and thus not numerically solvable. Here we are going to derive the boundary conditions at  $r = 0$  based on the local (analytical) solution at  $r = 0$ . The boundary conditions will then be used to replace the governing equations to avoid the singular terms.

In the infinitesimal region near  $r = 0$ , the mean flow can always be considered as uniform (for an axisymmetric mean flow, this is even more accurate). Therefore, the local solution near  $r = 0$  is, for a given  $x$  and an azimuthal mode number  $m$ ,

$$\hat{u}(x, r) \sim J_m(\beta r)$$

$$\hat{v}(x, r) \sim \frac{dJ_m(\beta r)}{dr}$$

$$\hat{w}(x, r) \sim \frac{J_m(\beta r)}{r}$$

$$\hat{p}(x, r) \sim J_m(\beta r)$$

where  $J_m$  is the  $m$ th order Bessel function of the first kind and  $\beta$  is a parameter determined by the local mean flow conditions. By using the properties of Bessel functions and extending the solutions to the  $x$ - $r$  plane of negative  $r$ , we have

$$\frac{\partial \hat{u}}{\partial r} = \hat{v} = \hat{w} = \frac{\partial \hat{p}}{\partial r} = 0 \quad (7.3)$$

for  $m$  being odd, and

$$\hat{u} = \frac{\partial \hat{v}}{\partial r} = \frac{\partial \hat{w}}{\partial r} = \hat{p} = 0 \quad (7.4)$$

for  $m$  being even but zero. The derivation of the boundary condition for  $m = 0$  involves a little more reasoning than other even modes, because for this mode,  $\frac{J_m(\beta r)}{r}$

is not continuous at  $r = 0$ . In fact,  $\frac{J_m(\beta r)}{r} = \infty$  for  $r = \infty$ . However, there is no rotating mode for  $m = 0$  and this physically means  $\hat{w} = 0$ . In other words, the proportionality constant for  $\hat{w} \sim \frac{J_m(\beta r)}{r}$  is zero. Therefore, the boundary conditions in Equation (7.4) also apply to the case of  $m = 0$ .

Although the local solution is for the uniform or zero mean flow case, the boundary conditions in Equations (7.3) and (7.4) are valid for a non-uniform mean flow case.

#### 7.1.2.2 Non-Reflecting Radiation Boundary Conditions

Non-reflecting radiation boundary conditions are applied at the duct outlet and at the Kirchhoff surface to allow any outgoing wave to exit the computational domain. Inhomogeneous terms are added at the outlet to allow waves entering the computational domain to simulate the fan face condition. The following non-reflecting radiation boundary conditions used in this chapter is a frequency-domain version of the time-domain formulation by Tam, et al., [47, 48, 50]

$$\left(i\omega + \frac{\partial}{\partial R} + \frac{1}{R}\right)\hat{\mathbf{u}} = \left(i\omega + \frac{\partial}{\partial R} + \frac{1}{R}\right)\hat{\mathbf{u}}_{\text{in}} \quad (7.5)$$

where  $\hat{\mathbf{u}}_{\text{in}} = [\hat{u}_{\text{in}}, \hat{v}_{\text{in}}, \hat{w}_{\text{in}}, \hat{p}_{\text{in}}]^T$  is the incoming waves, determined from the fan face condition and  $R$  is the distance from the current boundary point to the location of an imaginary point source inside the computational domain. If the source location is at  $(x_0, r_0)$  on the  $x-r$  plane of the current problem, Equation (7.5) is

$$\left(i\omega + \cos\alpha \frac{\partial}{\partial x} + \sin\alpha \frac{\partial}{\partial y} + \frac{1}{R}\right)\hat{\mathbf{u}} = \left(i\omega + \cos\alpha \frac{\partial}{\partial x} + \sin\alpha \frac{\partial}{\partial y} + \frac{1}{R}\right)\hat{\mathbf{u}}_{\text{in}} \quad (7.6)$$

with  $R = \sqrt{(x - x_0)^2 + (r - r_0)^2}$ ,  $\cos \alpha = \frac{x - x_0}{R}$ , and  $\sin \alpha = \frac{r - r_0}{R}$ .

We are going to study one specific mode of the fan noise with each simulation. Therefore, at the fan face of the inlet duct, the analytical solution [10] of mode  $(m, n)$  ( $m$  and  $n$  are the azimuthal and radial mode numbers, respectively) of a hard-wall cylindrical annular duct with the same inner and outer radii and mean flow is used for the inhomogeneous term  $\hat{u}_{\text{in}}$ . On the Kirchhoff surface  $\hat{u}_{\text{in}}$  is set to zero.

### 7.1.2.3 Impedance and Hard Wall Boundary Conditions

The acoustic liner on the inlet duct wall is modeled by the impedance boundary condition [26], which is, expressed in the current notation,

$$\hat{\mathbf{u}} \cdot \mathbf{n} = (\hat{p}/Z) + (1/i\omega)\bar{\mathbf{u}} \cdot \nabla(\hat{p}/Z) - (\hat{p}/i\omega Z)\mathbf{n} \cdot (\mathbf{n} \cdot \nabla\bar{\mathbf{u}}) \quad (7.7)$$

where  $\mathbf{n}$  is the local unit vector normal to the boundary surface and is positive when pointing from the fluid side to the liner,  $Z$  is the liner impedance and  $\bar{\mathbf{u}}$  is the vector of the mean flow velocity. We assume that the impedance  $Z$  is uniform and thus spatially independent and the acoustic treatment is impermeable, i.e., the normal mean flow velocity  $\bar{u}_{(n)}$  is zero at the boundary (but not its spatial derivatives). Under these two assumptions, Equation (7.7) is simplified to be

$$i\omega Z \hat{u}_{(n)} = i\omega \hat{p} + \bar{\mathbf{u}} \cdot \nabla \hat{p} - \hat{p} \frac{\partial \bar{u}_{(n)}}{\partial n} \quad (7.8)$$

with  $\hat{u}_{(n)}$  being the normal acoustic velocity.

When the governing Equation (7.9) is numerically solved using an iteration method or a pseudo-time marching method, the formulation in Equation (7.8) will cause numerical instability. We use a time-domain formulation of the impedance boundary

condition [49], which has been proved to be stable in the time-domain calculation. For example, such a formulation is, for a zero mean flow case,

$$\frac{\partial \hat{p}}{\partial n} = \frac{1}{R} \left( \frac{\partial \hat{u}}{\partial x} + \frac{\partial \hat{v}}{\partial r} + \frac{v + im\hat{w}}{r} - X\omega\hat{u}_n \right) \quad \text{for } X \leq 0 \quad (7.10)$$

$$\frac{\partial \hat{p}}{\partial n} = \frac{\omega}{X} (R\hat{u}_n - \hat{p}) \quad \text{for } X > 0 \quad (7.11)$$

At a hard wall, the hard wall boundary condition is formulated as

$$\frac{\partial \hat{p}}{\partial n} = 0 \quad (7.12)$$

### 7.1.3 Grid Generation and Transformation of the Governing Equations and Boundary Conditions

The duct geometry is described by the inner radius  $R_{inner}$  and the outer radius  $R_{outer}$ , both as a function of  $x$ ,

$$R_{inner}(x) = \max \left[ 0, 0.64212 - \sqrt{0.04777 + 0.98234(x/L)^2} \right] \quad (7.13)$$

$$R_{outer}(x) = 1 - \frac{0.08295}{a+1} \left[ a(x/L)^2 + \frac{e^{b(1-x/L)} - e^b}{1 - e^b} \right] \quad (7.14)$$

where the duct length  $L = 1.86393$  and  $a$  and  $b$  are parameters that determine the variation of the outer radius over the duct length but with the outer radius fixed at the two ends. ( $R_{outer}(0) = 1$  and  $R_{outer}(L) = 0.91705$ )

The problem is going to be solved in a body-fitted coordinate system. A body-fitted grid is generated using elliptic partial differential equations and a six-order accuracy scheme for discretization. Such accuracy will not compromise the accuracy of the numerical scheme for solving the governing equations and the boundary conditions. Since the geometry of the duct is parameterized, the grid can be automatically generated,

given a set of geometry parameters  $a$  and  $b$ . The grid generation gives the mapping from the physical domain  $(x, r)$  to the computational domain  $(\xi, \eta)$  and is formally expressed as

$$\xi = \xi(x, r)$$

$$\eta = \eta(x, r)$$

The governing equations and the boundary conditions are correspondingly transformed into and solved in the new coordinates  $(\xi, \eta)$ .

#### 7.1.4 Numerical Schemes

The governing equations are reformulated in a pseudo-transient form

$$\frac{\partial \hat{\mathbf{u}}}{\partial \tau} + \mathbf{A} \frac{\partial \hat{\mathbf{u}}}{\partial x} + \mathbf{B} \frac{\partial \hat{\mathbf{u}}}{\partial r} + \mathbf{C} \hat{\mathbf{u}} + i\omega \hat{\mathbf{u}} = \mathbf{0} \quad (7.15)$$

Equation (7.14) along with the same boundary conditions given earlier is solved with a 4th-order seven-point-stencil optimized upwind Dispersion-Relation-Preserving scheme. [68] The spatial coefficients for both the interior and the boundary points are the same as those listed in Reference [68] while the temporal coefficients are from Reference [47].

#### 7.1.5 Kirchhoff Integral

Due to the limitation of computational resources, we adopt a hybrid method to study acoustic radiation to the far field. With this method, the sound field inside of the duct and its near field is calculated using the CAA method discussed earlier while the sound field in the far field is calculated with a Kirchhoff method based on the information calculated by the CAA method on the Kirchhoff surface (see Figure 7.1)

The Kirchhoff's formulation in the frequency domain for a stationary surface [23], assuming the time dependence is  $\exp(i\omega t)$ , is

$$\varphi(\vec{x}, \omega) = \frac{1}{4\pi} \int_{S_0} \frac{1}{r_0} \exp\left\{-i\frac{\omega}{\beta^2}[\tau_0 - M(x - x')]\right\} \left[ \varphi\left(\frac{1}{r_0} + \frac{i\omega}{\beta^2}\right) \frac{\partial \tau_0}{\partial n_0} - \frac{\partial \varphi}{\partial n_0} - \frac{i\omega}{\beta^2} \varphi M \frac{\partial x'}{\partial n_0} \right] dS_0 \quad (7.16)$$

where  $M$  is the Mach number in the  $x$  direction,  $\beta = \sqrt{1 - M^2}$ ,  $\vec{x} = (x, y, z)$  is the observation point,  $\vec{y} = (x', y', z')$  is a point on the Kirchhoff surface, variables with subscript "0" are transformed variables based on the Prandtl-Glauert transformation,  $x_0 = x$ ,  $y_0 = \beta y$ ,  $z_0 = \beta z$  and  $\vec{r}_0 = \vec{x}_0 - \vec{y}_0$ .

## 7.2 Verification of Noise Prediction System

In this section, we verify the noise prediction system with several test problems, each with an emphasis on a different aspect of the noise prediction system.

### 7.2.1 Semi-Infinite Hard-Wall Annular Duct

In this test problem, we consider a semi-infinite hard-wall annular duct with an inner radius  $R_{\text{inner}} = 0.42356$  and an outer radius  $R_{\text{outer}} = 1$ . The duct starts at the left boundary and extends to infinity to the right. At the inner and outer duct walls, the hard wall boundary conditions in Equation (7.12) are applied. At the left boundary, the nonreflecting radiation boundary condition in Equation (7.6) is applied with the incoming waves  $\hat{u}_{\text{in}}$  given as mode (6,1) or mode (6,2) at  $\omega = 16$ . To simulate the infinite extension of the duct, we terminate the computational domain at some finite duct length to the right and apply the nonreflecting radiation boundary conditions with  $\hat{u}_{\text{in}} = 0$ . In

Figure 7.3, the numerical solutions (below the axis) are compared with the exact solution (above the axis) for mode (6,1) and mode (6,2), respectively. We can see that very good agreement is achieved.

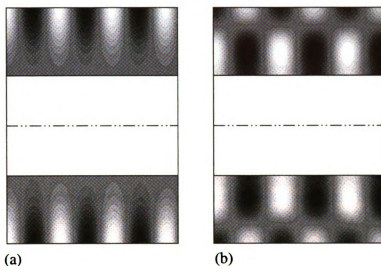


**Figure 7.3** Results of the hard-wall annular duct problem. The exact and the numerical solutions are above and below the axis, respectively. (a) mode (6,1); (b) mode (6,2).

### 7.2.2 Semi-Infinite Hard-Wall Circular Duct

In this problem, we consider a semi-infinite hard-wall circular duct, which is similar to the semi-infinite hard-wall annular duct problem except that the duct axis at  $r = 0$  is part of the computational domain, where the boundary conditions at  $r = 0$  are applied. The angular frequency, the outer radius and all the other boundary conditions are the same as in the annular duct problem above. Again the numerical solutions agree very well with the exact solutions for mode (6,1) and mode (6,2), as seen in Figure 7.4 (a) and Figure 7.4 (b), respectively.

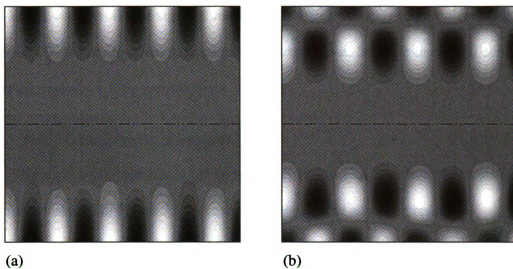


**Figure 7.4** Results of the hard-wall circular duct problem. The exact and the numerical solutions are above and below the axis, respectively. (a) mode (6,1); (b) mode (6,2).

### 7.2.3 Semi-Infinite Lined-Wall Circular Duct

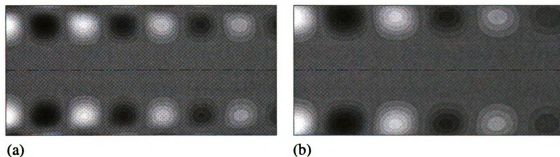


**Figure 7.5** Results of the lined-wall circular duct problem. The exact and the numerical solutions are above and below the axis, respectively. (a)  $\omega = 12$ ,  $Z = 0.2 - i$ , mode (6,1); (b)  $\omega = 10$ ,  $Z = 0.2 + i$ , mode (6,1).

The semi-infinite lined-wall circular duct problem is geometrically the same as the semi-infinite hard-wall circular duct considered problem above. The impedance boundary condition is applied at the lined wall. In Figure 7.5 (a) is a comparison between the exact and the numerical solutions for mode (6,1),  $\omega = 12$ ,  $Z = 0.2 - i$ . In Figure 7.5 (b) is a comparison between the exact and the numerical solutions for mode (6,1),

$\omega = 10$ ,  $Z = 0.2 + i$ . The signs of reactance in these two cases require that Equations (7.10) and (7.11) are applied, respectively. As we can see, both the numerical solutions accurately reproduce the exact solutions.

#### 7.2.4 Test Problem for the Kirchhoff Code

Here we verify our Kirchhoff code, which is based on Equation (7.16), using the test problem shown in Figure 7.6. An exact solution for the acoustic pressure is

$$\hat{p}(r) = \frac{\exp(-i\omega r)}{r}, \text{ for } 0 < r < \infty \quad (7.17)$$

where  $r$  is the radial coordinate in the spherical coordinate system. Because we assume the time dependence is of the form  $\exp(i\omega t)$ , Equation (7.17) is an outgoing wave and thus the source where this wave is originated is at  $r = 0$ , i.e., inside the Kirchhoff surface of radius  $r_0$ . Therefore, the acoustic pressure at any location outside the Kirchhoff surface can be predicted using Equation (7.16). The acoustic pressure obtained with the Kirchhoff code is compared with the exact solution for  $r_0 < r \leq 10r_0$  in Figure 7.7. We can see that the agreement is excellent.

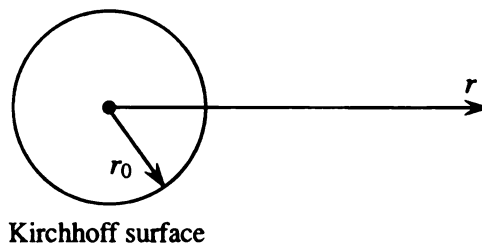


**Figure 7.6** Schematic of the test problem for the Kirchhoff method

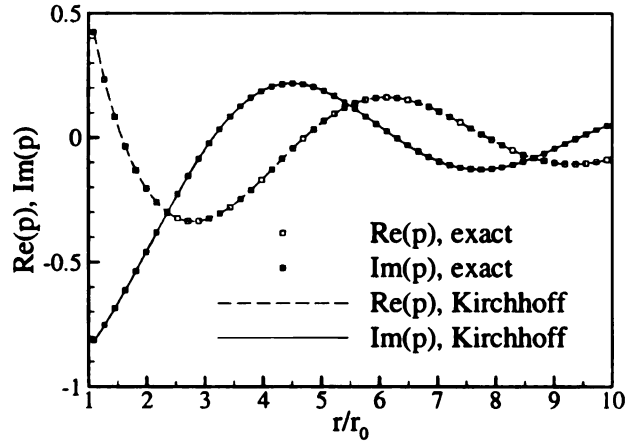


**Figure 7.7** Results of the test problem for the Kirchhoff method

With the noise prediction system verified, we now couple it with the same optimizer that has been discussed in Chapter 6. In the following sections, the noise prediction and optimization system will be applied to attack three optimization problems. For each of them, the objective function, the design variables, the constraints and the result will be defined and then the optimization result will be given.

### 7.3 Liner Impedance Optimization

#### 7.3.1 Problem Definition

For the liner impedance optimization, we use the duct geometry described with Equations (7.13) and (7.14) with  $a = -1.8166$  and  $b = -11$ . The liner is applied on a segment of the outer duct wall with the location unchanged during the optimization. The liner's resistance  $R$  and reactance  $X$  are selected as the design variables and no constraints are applied on them. For the purpose of demonstration, we use the total acoustic energy on the surface of the duct inlet  $S_{inlet}$  as the objective function  $F$ ,

$$F = \int_{S_{inlet}} |p|^2 dS \quad (7.18)$$

### 7.3.2 Optimization Result

The optimization starts with  $Z = 1 + i$  and terminates when a local optimum point is found. Figure 7.8 and Figure 7.9 show the history of the objective function defined in Equation (7.18) and the resistance  $R$  and reactance  $X$  as the optimization proceeds. The optimized design variables are achieved at  $R = 0.3936$  and  $X = -1.337$ , after about 100 iterations, with the objective function  $F$  decreasing from 0.1767 to 0.02469.

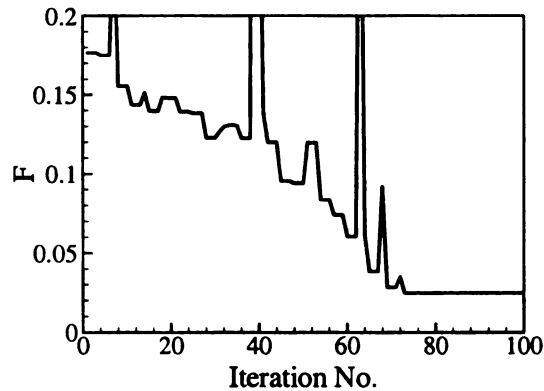


**Figure 7.8** The history of the objective function during the liner impedance optimization

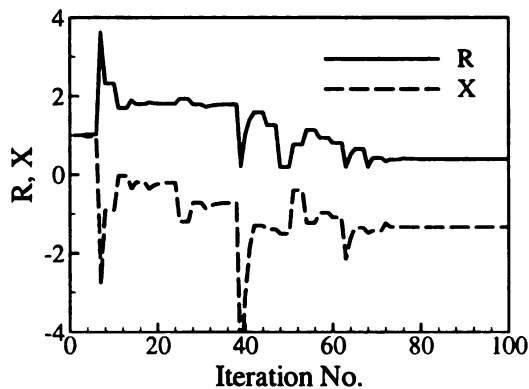


**Figure 7.9** The history of the design variables  $R$  and  $X$  during the liner impedance optimization.

Shown in Figure 7.10 is the sound field calculated with the optimized impedance parameters. The field in the region outside the duct is obtained with the Kirchhoff code. As a comparison, the case without any liner applied is shown in Figure 7.11. We can see a significant reduction in the noise level near the duct inlet and also in the far field as a result of the sound absorbing mechanism of the liner.



**Figure 7.10** The sound field calculated with the optimized liner impedance.

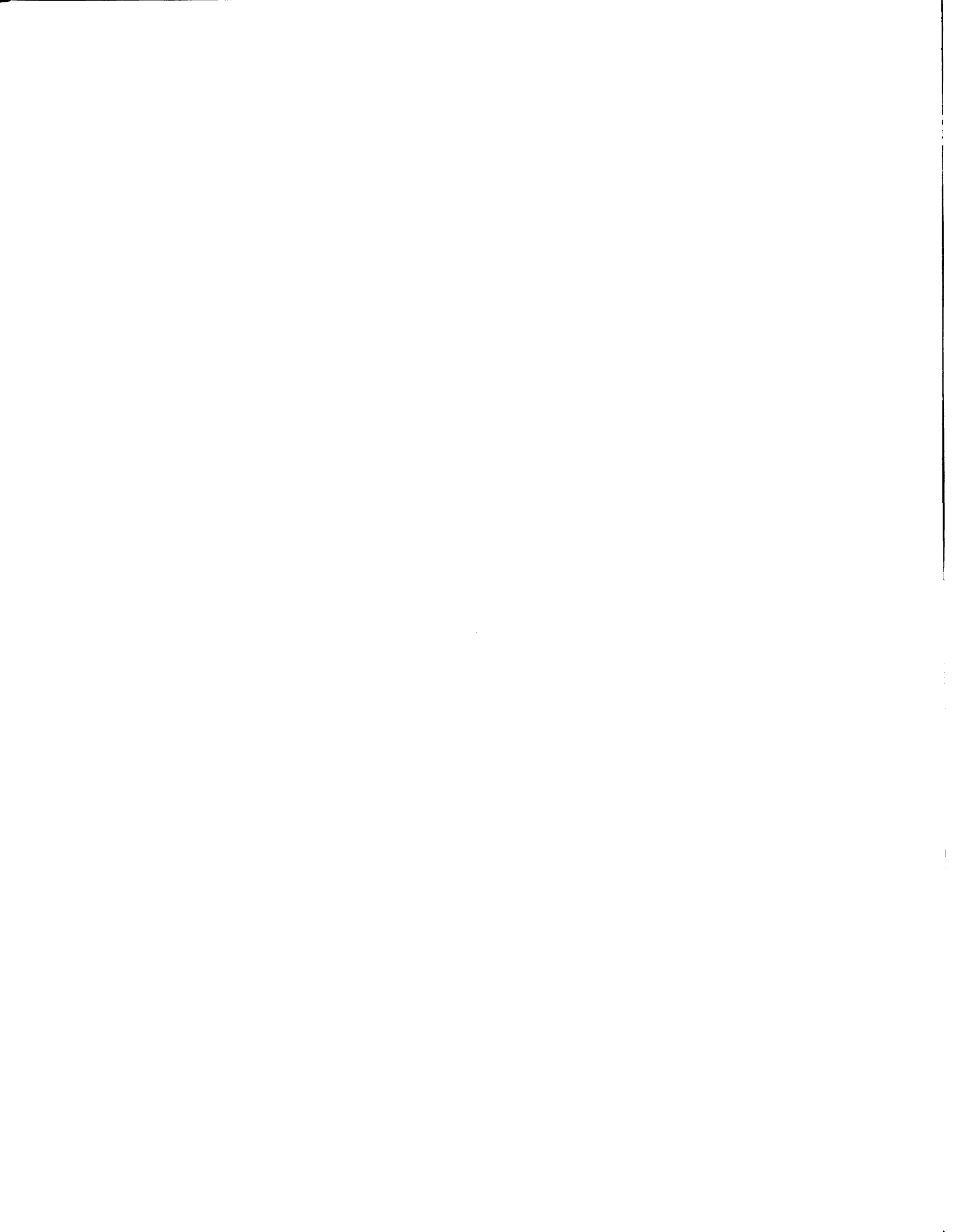


**Figure 7.11** The sound field calculated with the original geometry and without liners applied.

## 7.4 Geometry Optimization

### 7.4.1 Problem Definition

For the geometry optimization, all the walls are considered hard walls. The duct geometry is described with Equations (7.13) and (7.14), with parameters  $a$  and  $b$  as the design variables and no constraints are applied on them. The objective function are the same as defined in Equation (7.18).



### 7.4.2 Optimization Result

The optimization starts with  $a = -1.8166$  and  $b = -11$  and terminates when a local optimum point is found. Figure 7.12 and Figure 7.13 show the history of the objective function defined in Equation (7.18) and the design variables  $a$  and  $b$  as the optimization proceeds. The optimized design variables are achieved at  $a = 0.085284$  and  $b = -16.844$ , after about 30 iterations, with the objective function  $F$  decreasing from 0.81886 to 0.43303.

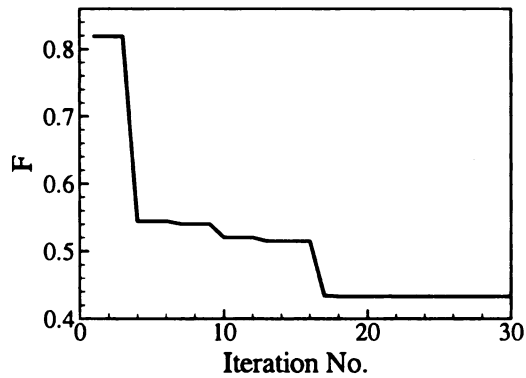


**Figure 7.12** The history of the objective function during the geometry optimization

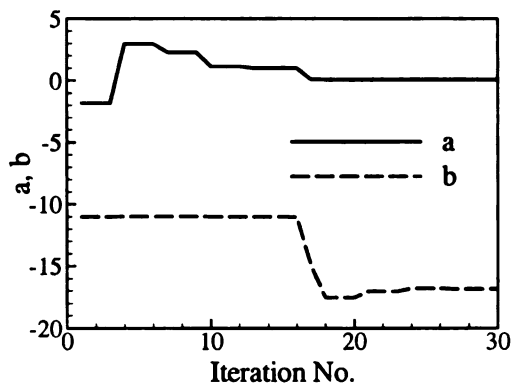


**Figure 7.13** The history of the design variables  $a$  and  $b$  during the geometry optimization.

The sound field calculated with the optimized geometry is shown in Figure 7.14, with the field outside the duct calculated with the Kirchhoff code. The sound field in Figure 7.11 corresponds to the geometry at the start of the optimization. The directivity pattern in the far field is changed but the reduction in the noise level is not obvious. This is because without the sound absorbing mechanism like a liner, the sound power emitted from the duct inlet is approximately equal to the sound power coming into the duct at the duct outlet, if the outgoing wave at the duct outlet due to the wall reflection is very small. The geometry optimization would be more effective when the directivity pattern is considered in the objective function or when the geometry is optimized together with the liner impedance optimization.



**Figure 7.14** The sound field calculated with the optimized geometry.

## 7.5 Liner Layout Optimization

Acoustic treatment of turbofan engine inlet ducts attenuates fan noise with the penalty of added weight. A design with the most weight-effective acoustic treatment is certainly desirable. The effectiveness of the acoustic treatment with given impedance properties depends on the number and sizes of the liner patches, as well as their mounting locations on the inlet duct wall. An example of this is shown in Figure 7.15, where the total area of liner patches (indicated by the bold lines along the duct walls) is the same for

the both cases. In this section the liner layout of a fixed-amount/area of liner patches is optimized to reduce the noise emission from a turbofan engine inlet duct.



**Figure 7.15** The sound fields with different layouts of liner patches. The bold lines indicate the liner patches. Equal amounts of liner are applied for the two cases.

### 7.5.1 Problem Definition

We assume that  $n$  liner patches are mounted on the duct wall, occupying half of the area of the duct wall,  $A$ . Note that this includes the cases of fewer liner patches. To simplify the analysis and also to reduce the calculation cost for the optimization process, we assume that all the patches are circular. With the duct wall radius given as a function of the axial coordinate  $x$ ,  $R(x)$ , the area and location of any patch  $i$  will only depend on the coordinates of its two ends,  $x_{i1}$  and  $x_{i2}$ , for  $i = 1, 2, \dots, n$ . These will be considered as the design variables. A physically correct layout of these patches requires that

$$0 \leq L_1 \leq x_{11} \leq x_{12} \leq \dots \leq x_{i1} \leq x_{i2} \dots \leq x_{n1} \leq x_{n2} \leq L_2 \leq L \quad (7.19)$$

where  $L$  is the length of the duct and  $L_1$  and  $L_2$  reflect design constraints. This is illustrated in Figure 7.16 for the case of  $n = 2$ . To satisfy the requirement on the total area of the liner patches, we need to have

$$\sum_{i=1}^n \int_{x_{i1}}^{x_{i2}} 2\pi R(x) dx = A/2 \quad (7.20)$$

Equations (7.19) and (7.20) are the constraints for the design variables.

As mentioned earlier, the grid generation is parameterized such that  $x_{i1}$  and  $x_{i2}$ , for  $i = 1, 2, \dots, n$  are always on grid points.

The objective function will reflect the noise level in an affected region during a take-off or landing period. The affected region may be an area in the vicinity of an airport, denoted by  $D$ , with any point on it denoted as  $\vec{x} \in D$ . We assume the airplane takes off at time  $t = 0$  and the noise is negligible to the people in the affected region after time  $t = T$ . The airplane travels in a path described by

$$\vec{x}_0 = \vec{x}_0(t) \quad (7.21)$$

This is illustrated in Figure 7.17 (note that Figure 7.17 uses a different coordinate system than Figure 7.16), with the reference frame set on the ground.

In the CAA simulation, the reference frame is established on the aircraft/engine inlet duct and the motion of the aircraft is equivalently treated as the free stream velocity. In such a case, any fixed point in the ground reference frame,  $\vec{x}$ , is now expressed as  $\vec{x}'(t) = \vec{x} - \vec{x}_0(t)$ . Correspondingly, the affected region  $D$  now becomes a function of the time,  $D'(t)$ , defined by

$$D'(t) = \{\vec{x}'(t) \mid \vec{x}'(t) = \vec{x} - \vec{x}_0(t), \vec{x} \in D\} \quad (7.22)$$

Thus, the objective function can be written in a form like

$$f = \int_0^T \iint_{D'(t)} |p_{\text{rms}}^2| dD' dt \quad (7.23)$$

which has the meaning of the overall acoustic power in the affected region during a take-off or landing period.

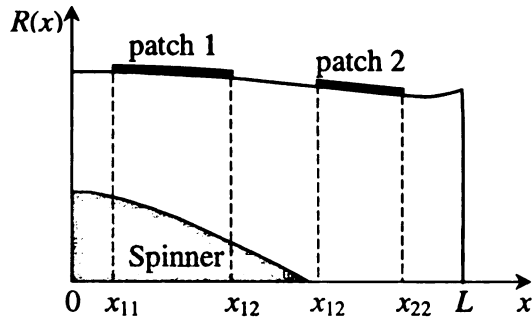


**Figure 7.16** Patches of liner on the duct wall

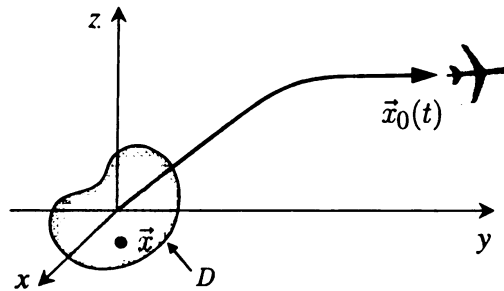


**Figure 7.17** Affected region and airplane path

### 7.5.2 Optimization Result

A simple case with only one liner patch on 40% of the total duct inner wall is considered. The impedance is given as  $Z = 1 + i$ . The design variables are thus the positions of the two ends of the liner patch,  $x_1$  and  $x_2$ .  $L_1$  and  $L_2$  are chosen to be 0.1864 and 1.6755, corresponding to  $0.1L$  and  $0.9L$ , respectively. The affected region  $S$  is given as a square of  $-5 \leq x \leq 5$ ,  $-5 \leq y \leq 5$  and  $z = 0$  during a landing period  $-100 \leq t \leq 0$ , with  $t = 0$  defined when the engine arrives at  $x = 0$ ,  $y = 0$  and  $z = 0$ . During the landing period, the aircraft moves at  $M = 0.1$  with a descending trajectory at angle of  $30^\circ$ .

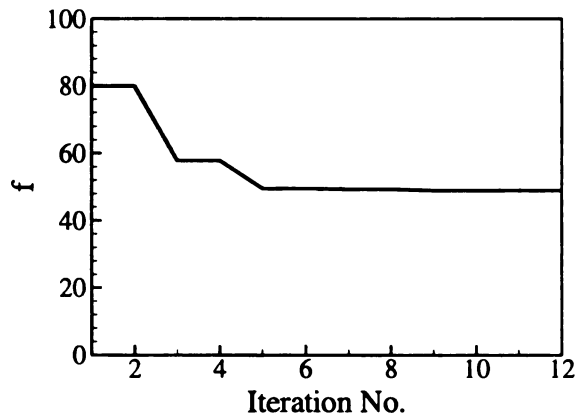


**Figure 7.18** The history of the objective function during the geometry optimization.

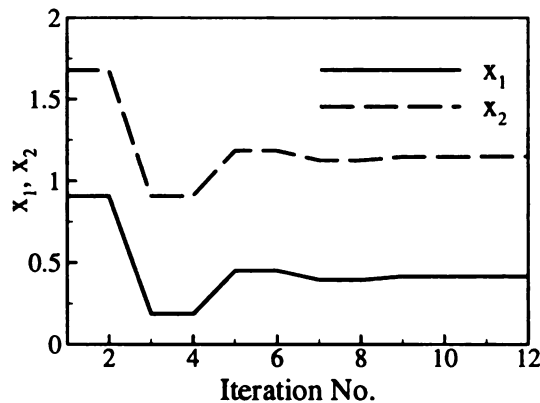
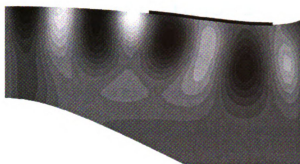
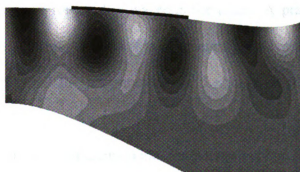


**Figure 7.19** The history of the design variables  $x_1$  and  $x_2$  during the geometry optimization.

The optimization starts with  $x_1 = 0.9062$  and  $x_2 = L_2 = 1.6755$ . Figure 7.18 and Figure 7.19 show the history of the objective function defined in Equation (7.23) and the design variables  $x_1$  and  $x_2$  as the optimization proceeds. The optimized design variables are found at  $x_1 = 0.4165$  and  $x_2 = 1.1483$  with the objective function  $f$  decreasing from 79.9 to 49.0. The sound field with the liner layout at the start of the optimization is shown in Figure 7.20 (a). Figure 7.20 (b) shows the sound field calculated with the optimized layout. The bold lines along the duct walls indicate the liners patches.



(a)



(b)

**Figure 7.20** The sound field before (a) and after (b) optimization.

## 8 CONCLUSIONS

The effects of optimization parameters,  $\beta_0$ ,  $\lambda$  and  $\sigma$  on the characteristics of broadband optimized upwind schemes are systematically studied. It is shown that there are optimum values for the control parameter  $\sigma$  and the weighting parameter  $\lambda$  for a given range of wavenumber, at which the overall accuracy of the schemes improves. A scheme that is accurate everywhere for a wide range is virtually not possible since increasing the accuracy for relatively large wavenumber  $\alpha\Delta x$  is always at the expense of decreasing the accuracy for smaller wavenumber  $\alpha\Delta x$ . A practical approach is to optimize a scheme by adjusting the available parameters in such a way that its dispersion and dissipation errors at all the wavenumbers in the range of interest are reasonably balanced.

The unique feature of optimized multi-component upwind and central schemes is that they are optimized for the selected wavenumbers so that they can accurately and efficiently predict the acoustic waves traveling with these wavenumber components. When calculating a sound field consisting of dominant wavenumbers, the optimized multi-component schemes are superior to the optimized broadband schemes. For broadband waves, the optimized upwind multi-component schemes need to be modified so that they are stable for the range of wavenumbers considered. The optimized central 1-component schemes can give nearly identical dispersion and dissipation characteristics as those of the optimized central broadband schemes. For a given stencil width, the 2-component schemes give better characteristics than the optimized central broadband schemes. Based on the Fourier analysis, it is expected that the optimized central multi-component schemes are at least comparable to if not better than the optimized central

broadband schemes when solving broadband wave problems. The accuracy of the multi-component schemes improves as the number of wavenumbers chosen for optimization increases. However, the number of stencil points has to be increased accordingly.

The time-domain impedance boundary condition is a type of boundary condition that is unique and important to CAA. It imposes more challenges than most of the other types of boundary conditions involve in CAA. A three-dimensional initial and impedance boundary problem is proposed to benchmark broadband time-domain impedance boundary conditions in a three-dimensional context. Its analytical solution is derived and evaluated. A CAA code using Tam and Auriault's formulation of broadband time-domain impedance boundary condition very accurately reproduces the analytical solution. This formulation is also used in some of the other chapters of the thesis.

The above-mentioned CAA code, with slight modification, is also tested in an impedance duct environment. It is tested against the analytical solution of a semi-infinite impedance duct problem and the experimental data from the NASA Langley flow impedance tube facility in the presence of a sheared or zero mean flow. The CAA code accurately predicts the duct acoustics in terms of both amplitude and phase. Both the analytical solution and the experimental data are only available for single-frequency cases. However, since the system of the linearized Euler equations and all the boundary conditions are linear, a series of tests at discrete frequencies representing the spectrum in a certain range should reasonably be equivalent to a broadband test in the same range.

A global time-domain technique is presented to achieve the acoustic wave solution by subtracting the contained instability wave solution from the total solution of the LEE. In particular this study is focused on multi-frequency component sound sources.

The characteristics of the eigen-solution of the homogeneous LEE with the boundary conditions allow us to relate the contained instability wave solution with the pure instability wave solution. As a result, the contained instability wave solution, instead of being suppressed, is obtained from the pure instability wave solution and the total solution with a technique developed in the study. The acoustic wave solution can then be achieved by subtracting the contained instability wave solution from the total solution. The concept of the method presented here is simple and the method is easy to be implemented. The effectiveness of the method is demonstrated by a test problem solved with the previously developed CAA code. The presented method can potentially be applied to problems with more generalized mean flows, practical sound sources, and realistic physical domains.

A conceptual design is developed for adaptive noise control through the coupling of a CAA time-domain code with an optimizer. A three-parameter broadband impedance model is used for the purpose of demonstration of the concept although the concept works for all kinds of liners with controllable impedance. The CAA code with the broadband time-domain impedance boundary condition serves as an accurate and efficient tool for simulating the acoustic field to be controlled. Incorporating the CAA code with the optimizer, it is shown that the optimization procedure is able to find the optimum impedance properties for a desired acoustic field under different mean flow conditions.

As another application of the CAA code that has been developed and tested, a noise prediction and optimization system for turbofan inlet duct designs is developed. Such a system consists of a noise prediction system and an optimizer. A hybrid method is

adopted for the purpose of more efficient noise prediction: the CAA code is used for the duct and its near field and a Kirchhoff method for the far field. The noise prediction system is verified with several test problems, each emphasized on testing a specific aspect of the system. The capabilities of the optimizer coupled with the noise prediction system are demonstrated with three optimization problems: liner impedance optimization; duct geometry optimization and liner layout optimization. The results show that the optimization can effectively change the acoustic field in favor of the design objectives.

Some topics that may deserve further study are briefly discussed as follows.

The current DRP schemes are finite difference schemes that can only be applied on a structured grid. A high-order DRP scheme on unstructured grids is highly desirable since it would be accurate for wave propagation in long distances as well as flexible for complex geometries.

The impedance boundary condition is mathematically unstable with a non-zero tangential flow at the boundary. However such a scenario exists in practice when the local effects are averaged over the surface of a liner, resulting in a uniform impedance boundary condition and at the same time non-zero tangential flow. Therefore, a stable formulation of the impedance boundary condition with non-zero tangential flow would be of great value for modeling lined boundaries.

A more general formulation of the impedance boundary condition with an arbitrary flow would be useful to model any boundary beyond which all the effects are lumped and represented by the boundary condition. It would be a universal formulation for nearly all types of the boundary conditions encountered in CAA. This should be another potential subject for future study.

## **BIBLIOGRAPHY**

## BIBLIOGRAPHY

- 1 Agarwal, A., Morris, P. J., and Mani, R., "Calculation of Sound Propagation in Nonuniform Flows: Suppression of Instability Waves," *AIAA Journal*, Vol. 42, No. 1, 2004, pp. 80-88.
- 2 Ahuja, K. K. and Gaeta, R. J., Jr., "Active Control of Liner Impedance by Varying Orifice Geometry," NASA/CR-2000-210633.
- 3 Ahuja, V., Özyörük, Y., and Long, L. N., "Computational Simulations of Fore and Aft Radiation from Ducted Fans," *AIAA Paper 2000-1943*, June 2000.
- 4 Armstrong, D. L., "Acoustic Grazing Flow Impedance Using Waveguide Principles," NASA CR-120848, 1971.
- 5 Arsac, J., *Fourier Transforms and the Theory of Distributions*, Prentice-Hall, Inc, 1966.
- 6 Dahl, M. D., "Solution to the Category 5 Problem: Generation and Radiation of Acoustic Waves from a 2D Shear Layer," *Proceedings of the Third Computational Aeroacoustics Workshop on Benchmark Problems*, Cleveland, Ohio, November, 1999, NASA/CP-2000-209790, August, 2000, pp. 87-92.
- 7 Dawson, Thomas H., *Theory and Practice of Solid Mechanics*, Plenum Press, 1976.
- 8 Dowling, A. P., Ffowcs Williams, J. E., and Goldstein, M. E., "Sound Production in a Moving Stream," *Phil. Trans. Roy. Soc. Lond., A*, Vol. 288, 1978, pp. 321-349.
- 9 Eversman, W., Parrett, A. V., Preisser, J. S., and Silcox, R. J., "Contributions to the Finite Element Solution of the Fan Noise Radiation Problem," *ASME Journal of Vibration, Acoustics, Stress and Reliability in Design*, Vol. 107, April, 1985, pp.216-223.
- 10 Eversman, W. E., "Theoretical Models for Duct Acoustic Propagation and Radiation," *Aeroacoustics of Flight Vehicles: Theory and Practice*, edited by Hubbard, H. H., NASA RP-1258, Aug. 1991, Chapter 13.
- 11 Eversman, W., and Roy, I. D., "Ducted Fan Acoustic Radiation Including the Effects of Non-Uniform Mean Flow and Acoustic Treatment," *AIAA Paper 1993-4424*, Oct. 1993.
- 12 Ewert, R., and Schröder, W., "Acoustic Perturbation Equations Based on Flow Decomposition via Source Filtering," *Journal of Computational Physics*, Vol. 188, 2003, pp. 365-398.

- 13 Fung, K.-Y., and Ju, H., "Impedance and Its Time-Domain Extensions," *AIAA Journal*, Vol. 38, 2000, pp. 30-38.
- 14 Fung, K.-Y., and Ju, H., "Broadband Time-Domain Impedance Models," *AIAA Journal*, Vol. 39, 2001, pp. 1449-1454.
- 15 Gottlieb, P., "Sound Source Near a Velocity Discontinuity," *The Journal of the Acoustical Society of America*, Vol. 32, 1960, pp. 1117-1122.
- 16 Hu, F. Q., "A Stable, Perfectly Matched Layer for Linearized Euler Equations in Unsplit Physical Variables," *Journal of Computational Physics*, Vol. 173, 2001, pp. 455-480.
- 17 Ju, H., and Fung, K.-Y., "Time-Domain Impedance Boundary Conditions with Mean Flow Effects," *AIAA Journal*, Vol. 39, 2001, pp. 1683-1690.
- 18 Kinsler, L. E., and Frey, A. R., *Fundamentals of Acoustics*, 2nd edition, John Wiley & Sons, Inc, 1962.
- 19 Li, X. D., Schemel, C., Michel, U. and Thiele, F., "Azimuthal Sound Mode Propagation in Axisymmetric Flow Ducts," *AIAA Journal*, Vol. 42, 2004, pp. 2019-2027.
- 20 Li, X. D., Schoenwald, N., Yan, J. and Thiele, F., "A Numerical Study on Acoustic Radiation from a Scarfed Intake," *AIAA Paper 2003-3245*, May 2003.
- 21 Li, Y., "Wavenumber-Extended High-Order Upwind-Biased Finite Difference Schemes for Convective Scalar Transport," *Journal of Computational Physics*, Vol. 13, 1997, pp. 235-255.
- 22 Lockard, D.P., Brentner, K.S., and Atkins, H.L., 1995, "High-Accuracy Algorithms for Computational Aeroacoustics," *AIAA Journal*, Vol. 33, pp. 246-251.
- 23 Lyrantzis, A. S., and Mankbadi, R. R., "Prediction of the Far-Field Jet Noise Using Kirchhoff's Formulation," *AIAA Journal*, Vol. 34, 1996, pp. 413-416.
- 24 Mani, R., "The Influence of Jet Flow on Jet Noise. Part 1. The Noise of Unheated Jets," *Journal of Fluid Mechanics*, Vol. 73, 1976, pp. 753-778.
- 25 "Optimization Toolbox for Use with MATLAB®," MathWorks, Natick, MA, 2002.
- 26 Meyers, M. K., "On the Acoustic Boundary Condition in the Presence of Flow," *Journal of Sound and Vibration*, Vol. 71, 1980, pp. 429-434.
- 27 Mottsinger, R. E. and Kraft, R. E., "Design and Performance of Duct Acoustic Treatment," *Aeroacoustics of Flight Vehicles: Theory and Practice*, NASA RP-1258, Aug. 1991, Chap.14.

- 28 Nallasamy, M., Sutliff, D. L., and Heidelberg, L. J., "Propagation of Spinning Acoustic Modes in Turbofan Exhaust Ducts," *Journal of Propulsion and Power*, Vol. 16, 2000, pp.736-743.
- 29 Nayfeh, A. H., Kaiser, J. E., and Shaker, B. S., "Effect of Mean-Velocity Profile Shapes on Sound Transmission through Two-Dimensional Ducts," *Journal of Sound and Vibration*, Vol. 34, 1974, pp. 413-423.
- 30 Özyörük, Y., and Long, L. N., "Computation of Sound Radiating from an Engine Inlets," *AIAA Journal*, Vol. 34, 1996, pp.894-901.
- 31 Özyörük, Y., and Long, L. N., "A Time-Domain Implementation on Surface Acoustic Impedance Condition with and without Flow," *AIAA Paper 96-1663*, May 1996.
- 32 Özyörük, Y., and Long, L. N., "A Time-Domain Implementation of Surface Acoustic Impedance Condition with and without Flow," *Journal of Computational Acoustics*, Vol. 5, 1997, pp. 277-296.
- 33 Özyörük, Y., Long, L. N. and Jones, M. G., "Time-Domain Numerical Simulation of a Flow-Impedance Tube," *Journal of Computational Physics*, Vol. 146, 1998, pp. 29-57.
- 34 Özyörük, Y., and Long, L. N., "Time-Domain Calculation of Sound Propagation in Lined Ducts with Sheared Flows," *AIAA Paper 99-1817*, May 1999.
- 35 Özyörük, Y., and Long, L. N., "Time-domain calculation of sound propagation in lined ducts with sheared flows," *AIAA Journal*, Vol. 38, 2000, pp. 768-773.
- 36 Özyörük, Y., Alpman, E., Ahuja, V. and Long, L. N., "A Frequency-Domain Numerical Method for Noise Radiation From Ducted Fans," *AIAA Paper 2002-2587*, June 2002.
- 37 Parrott, T. L., Watson, W. R., and Jones, M. G., "Experimental Validation of a Two-Dimensional Shear Flow Model for Determining Acoustic Impedance," *NASA TP-2679*, NASA, Washington, DC, 1987.
- 38 Poritsky, H., "Extension of Weyl's Integral for Harmonic Spherical Waves to Arbitrary Wave shapes," *Communications on Pure and Applied Mathematics*, Vol. IV, 1951, pp. 33-42.
- 39 Rienstra, S. W. and Eversman, W., "A Numerical Comparison Between Multi-Scales and FEM Solution for Sound Propagation in Lined Flow Ducts," *Journal of Fluid Mechanics*, Vol. 437, 2001, pp. 367-384.
- 40 Roseau, M., *Asymptotic Wave Theory*, North-Holland Publishing Company, 1976.

- 41 Rumsey, C. L., Biedron, R. T., Farassat, F., and Spence, P. L., "Duct-Fan Engine Acoustic Predictions Using a Navier-Stokes Code," *Journal of Sound and Vibration*, Vol. 213, No. 4, 1998, pp.643-664.
- 42 Schoenwald, N., Schemel, C., Eschricht, D., Michel, U., and Thiele, F., "Numerical Simulation of Sound Propagation and Radiation from Aero-Engine Intakes," *Proceedings of the 3rd Aeroacoustics Workshop SWING*, October 26-27, 2002, University Stuttgart.
- 43 Shim, I. B., Kim, J. W., and Lee, D. J., "Numerical Study on Radiation of Multiple Pure Tone Noise from an Aircraft Engine Inlet," *AIAA Paper 99-1831*, May 1999.
- 44 Stanescu, D., Ait-Ali-Yahia, D., Habashi, W. G., and Robichaud, M. P., "Multidomain Spectral Computations of Sound Radiation from Ducted Fans," *AIAA Journal*, Vol. 37, 1999, pp.296-302.
- 45 Tam, C. K. W., and Shen, H., "Direct Computation of Nonlinear Acoustic Pulses Using High-Order Finite Difference Schemes," *AIAA Paper 1993-4325*.
- 46 Tam, C.K.W., Webb, J.C., and Dong, Z., "A Study of the Short Wave Components in Computational Aeroacoustics," *Journal of Computational Acoustics*, Vol. 1, 1993, pp. 1-30.
- 47 Tam, C. K. W., and Webb, J. C., "Dispersion-Relation-Preserving Finite Difference Schemes for Computational Acoustics," *Journal of Computational Physics*, Vol. 107, No. 2, 1993, pp. 262-281.
- 48 Tam, C. K. W., and Dong, Z., "Radiation and Outflow Boundary Conditions for Direct Computation of Acoustic and Flow Disturbances in a Nonuniform Mean Flow," *Journal of Computational Acoustics*, Vol. 4, 1996, pp. 175-201.
- 49 Tam, C. K. W., and Auriault, L., "Time-Domain Impedance Boundary Conditions for Computational Aeroacoustics," *AIAA Journal*, Vol. 34, 1996, pp.917-923.
- 50 Tam, C. K. W., Fang, J. and Kurbatskii, K. A., "Non-homogeneous Radiation and Outflow Boundary Conditions Simulating Incoming Acoustic and Vorticity Waves for Exterior Computational Aeroacoustics Problems", *International Journal for Numerical Methods in Fluids*, Vol. 26, 1998, pp. 1107-1123.
- 51 Tester, B. J., "The Propagation and Attenuation of Sound in Lined Ducts Containing Uniform of Plug Flow," *Journal of Sound and Vibration*, Vol. 28, 1973, pp. 151-203.
- 52 Tester, B. J., "Some Aspects of 'Sound' Attenuation in Lined Ducts Containing Inviscid Mean Flows with Boundary Layers," *Journal of Sound and Vibration*, Vol. 28, 1973, pp. 217-245.

- 53 Tester, B. J., and Burrin, R. H., "On Sound Radiation from Sources in Parallel Sheared Jet Flows," AIAA Paper 74-57, Jan. 1974.
- 54 Watson, W. R., Private communication, 2002.
- 55 Watson, W. R., Jones, M. G. and Parrott, T. L., "Validation of an Impedance Eduction Method in Flow," AIAA Journal, Vol. 37, 1999, pp. 818-824.
- 56 Watson, W. R., Tracy, M. B., Jones, M. G. and Parrott, T. L., "Impedance Eduction in the Presence of Shear Flow," AIAA Paper 2001-2263, May 2001.
- 57 Whitham, G. B., Linear and Nonlinear Waves, John Wiley & Sons, Inc, 1974.
- 58 Zhang, X., Chen, X. X., Morfey, C. L., Tester, B. J., "Computation of Fan Noise Radiation through a Realistic Engine Exhaust Geometry with Flow," AIAA Paper 2003-3267, May 2003.
- 59 Zheng, S., Miller, A. E., and Zhuang, M., "Radiation and Refraction of Sound Waves through a Two-dimensional Shear Layer," The Proceedings of the 4th Computational Aeroacoustics Workshop on Benchmark Problems, in press.
- 60 Zheng, S., and Zhuang, M., "A New Conceptual Design for Active Noise Control for Controllable Impedance Liners," AIAA Paper 2002-2518.
- 61 Zheng, S. and Zhuang, M., "Application and Verification of Broadband Time Domain Impedance Boundary Conditions in Multi-Dimensional Acoustic Problems," AIAA Paper 2002-2593, June 2002.
- 62 Zheng, S. and Zhuang, M., "A Computational Aeroacoustics Prediction Tool for Duct Acoustics with Analytical and Experimental Validations," AIAA Paper 2003-3248, May, 2003.
- 63 Zheng, S., and Zhuang, M., "Computational Aeroacoustics Time-Domain Method Coupled with Adaptive Noise Control Optimizer," AIAA Journal, Vol. 41, 2003, pp.1853-1857.
- 64 Zheng, S., and Zhuang, M., "Three-Dimensional Benchmark Problem for Broadband Time-Domain Impedance Boundary Conditions," AIAA Journal, Vol. 42, 2004, pp. 405-407.
- 65 Zheng, S. and Zhuang, M., "Noise Prediction and Optimization System for Turbofan Engine Inlet Duct Design," AIAA Paper 2004-3031, May 2004.
- 66 Zheng, S. and Zhuang, M., "Verification and Validation of Time-Domain Impedance Boundary Condition in Lined Ducts," AIAA Journal, Vol. 43, 2005, pp. 306-313.

- 67 Zhuang, M., and Chen, R.F., "Optimized Upwind Dispersion-Relation-Preserving Finite Difference Schemes for Computational Aeroacoustics," AIAA Journal, Vol. 36, 1998, pp. 2146-2148.
- 68 Zhuang, M., and Chen, R. F., "Applications of High-Order Optimized Upwind Schemes for Computational Aeroacoustics," AIAA Journal, Vol. 40, 2002, pp. 443-449.